

# **Analysis of Poly(L-lactide) Nanocomposites Based on Layered Double Hydroxides : Comparison of NiAl and MgAl LDH**

vorgelegt von

**M. Sc.**

**Jing Leng**

aus Qingdao, VR China

von der Fakultät III – Prozesswissenschaften  
der Technischen Universität Berlin  
zur Erlangung des akademischen Grades

Doktor der Naturwissenschaften

Dr. rer. nat.

genehmigte Dissertation

Promotionsausschuss:

Vorsitzender: Prof. Dr. rer. nat. Walter Reimers

Gutachter: Prof. Dr. –Ing. Manfred H. Wagner

Gutachter: Prof. Dr. rer. nat. Andreas Schönhals

Tag der wissenschaftlichen Aussprache: 09. Dezember 2016

Berlin 2016



## **Acknowledgements**

Firstly, I would like to express my sincere gratitude to my supervisor Prof. Dr. Andreas Schönhals (BAM Bundesanstalt für Materialforschung und -prüfung) for giving me the opportunity to do the research about polymer nanocomposites. During the journey of four years, his expert advice never fails to inspire me and his encouragement always motivates me to overcome one difficulty after another. I also thank my registered supervisor Prof. Dr. Manfred H. Wagner (Technische Universität Berlin) for his help of the enrollment and supervision of my project. I appreciate Prof. Dr. De-Yi Wang (IMDEA Materials Institute) for offering me the research samples and building the collaboration with our group, without his supply I have no possibility to finish my dissertation.

I acknowledge the financial support from the China Scholarship Council (CSC) for the cost of my living in Germany.

For my topic research, the helps from the following people are very important. I thank Dr. Nianjun Kang for preparing the samples for me. The sharing of the device temperature modulated differential scanning calorimetry (TMDSC) and the insightful discussions from Prof. Dr. Christoph Schick (Universität Rostock) and Dr. Andreas Wurm (Universität Rostock) are significantly helpful for the investigation of my topic. The measurements and analysis of small- and wide-angle X-ray scattering (SAXS and WAXS) from Dr. Jana Falkenhagen, Dr. Franziska Emmerling (BAM) and Dr. Andreas F. Thünemann (BAM) are necessary for the completion of my project.

Meanwhile, I thank the helps from the technicians in BAM. Thank Mr. Audi for pumping nitrogen tanks and instructing coating process. Thank Mr. Neubert for measuring conventional DSC data. Also thank Mr. Milczewski for his enthusiastic assistance.

Although it is not very relevant to the topics investigated, I am grateful for the company of my colleagues in our group. They are Huajie, Christina, Marieke, Sherif, Shereen, Nora, Arda, Farooq, Asad, Yi, Paulina and Timur. Thank you for the good times in the four years and wish you have a bright future ahead.

The supports from friends and parents are indispensable for my dissertation. I believe that I will always recall the days in Berlin even if a long time passes, here I just would like to give my most sincere appreciation to you.



## Table of Contents

<b>Acknowledgements</b> .....	3
<b>Abstract</b> .....	7
<b>Zusammenfassung</b> .....	9
<b>1. Introduction</b> .....	11
1.1 Polymer Nanocomposites .....	11
1.2 Motivation of this work.....	12
1.3 Structure of the thesis .....	13
<b>2. Scientific Background</b> .....	15
2.1 Layered Double Hydroxide .....	15
2.2 Polymer nanocomposites based on LDH.....	17
2.3 Relaxation phenomena in polymers.....	19
2.3.1 Four dynamics regions of the polymer system in dependence on temperature .....	19
2.3.2 The glass transition .....	21
2.3.3 The theories describing glassy dynamics of polymers.....	25
2.4 Three phase model of the semicrystalline polymer .....	27
<b>3. Principles of characterization techniques</b> .....	31
3.1 Differential Scanning Calorimetry.....	31
3.1.1 Conventional differential scanning calorimetry.....	31
3.1.2 Temperature modulated differential scanning calorimetry .....	32
3.2 Small- and Wide- angle X-ray Scattering.....	36
3.3 Broadband Dielectric Spectroscopy .....	39
3.3.1 The principle of BDS .....	39
3.3.2 Analysis of dielectric spectra .....	45
<b>4. Experimental section</b> .....	51
4.1 Materials.....	51
4.1.1 Organic modified Layered double hydroxides.....	51
4.1.2 Poly(L-lactide) .....	51
4.2 Preparation of nanocomposites .....	51
4.3 Experimental techniques .....	52
4.3.1 X-ray scattering.....	52
4.3.2 Size Exclusion Chromatography (SEC).....	53

4.3.3 Thermal analysis .....	53
4.3.4 Broadband dielectric spectroscopy (BDS).....	55
<b>5. Investigation of nanocomposites based on polylactide and MgAl/LDH ...</b>	<b>57</b>
5.1 The SAXS analysis for the modified LDH and the dispersion of the nanofiller within the nanocomposites .....	57
5.2 SEC analysis for the degradation stability of the nanocomposites.....	59
5.3 Crystallinity of the nanocomposites investigated by DSC and WAXS.....	61
5.4 The further analysis of the rigid amorphous phase of MgAl/LDH-PLA nanocomposites.....	65
5.5 Dielectric spectroscopy analysis for the MgAl/LDH-PLA nanocomposites .....	74
<b>6. Investigation of PLA nanocomposites based on NiAl-LDH and a comparison with its MgAl-LDH counterpart.....</b>	<b>87</b>
6.1 Characterization of modified LDH and the PLA nanocomposites by SAXS .....	87
6.2 Characterization of Degradation stability of the nanocomposites by SEC.....	90
6.3 Crystallization analysis of the nanocomposites investigated by DSC and WAXS .....	92
6.4 The phase fraction analysis between NiAl/LDH-PLA and MgAl/LDH-PLA nanocomposites.....	96
6.5 Dielectric Spectroscopy analysis for the NiAl/LDH-PLA nanocomposites .....	101
<b>7. Conclusions and outlook .....</b>	<b>111</b>
<b>Reference .....</b>	<b>115</b>
<b>List of Symbols and Abbreviations</b>	
<b>List of Publications</b>	

## Abstract

This work focuses on the analysis of the poly (L-lactide) nanocomposites based on modified MgAl and NiAl layered double hydroxides (LDH) characterized by measurements such as size exclusion chromatography (SEC), differential scanning calorimetry (DSC), small- and wide-angle X-ray scattering (SAXS and WAXS) and broadband dielectric spectroscopy (BDS).

The polymer based nanocomposites were prepared by melt blending. Both nanocomposites were found degradation enhancements for PLA by the SEC measurements. Further, NiAl/LDH-PLA nanocomposites showed a stronger degradation than the MgAl/LDH-PLA system. This distinction could be assigned to the different properties of Mg and Ni ions.

The original and modified structures of MgAl/LDH and NiAl/LDH were characterized by SAXS measurements. The size and dispersion of the modified LDHs were shown to be different for MgAl/LDH-PLA and NiAl/LDH-PLA nanocomposites. These distinctions were considered to be related to the properties of different nanofillers.

The degree of crystallization, in dependence on the LDH concentration, investigated by DSC, agrees with the WAXS results for both nanocomposites.

On the basis of the three-phase model describing semicrystalline polymer, the phase of the PLA was divided into crystalline fraction (CF) and non-crystalline fraction. The non-crystalline fraction was subdivided into the mobile amorphous fraction (MAF) contributing and the rigid amorphous fraction (RAF) not contributing to the relaxation strength at the glass transition. In addition, according to related literatures, in the PLA nanocomposites, the RAF could be composed of the RAF caused by the nanofiller ( $RAF_{\text{filler}}$ ) and the RAF caused by the crystallization ( $RAF_{\text{crystal}}$ ). For separating the different parts of RAF, two steps of experiments were applied. In the first step, the critical cooling rate was determined to suppress the crystallization of PLA during the cooling process, then to eliminate the production of  $RAF_{\text{crystal}}$ . In the second step, with the treated sample, the contribution to the relaxation strength at glass transition was calculated by the measurements from temperature modulated DSC (TMDSC), then the  $RAF_{\text{filler}}$  was obtained. Coupling with the measurements of the  $RAF_{\text{all}}$ , MAF and CF, analysis of both RAFs in dependence on LDH concentrations were made. The most noteworthy result for the differences between MgAl/LDH and NiAl/LDH systems was the LDH concentration

dependence on the ratio of  $RAF_{\text{filler}}$  and filler mass. A larger contacting area with PLA segments for MgAl/LDH nanocomposites could be deduced.

Therefore, a partly-exfoliated structure of MgAl/LDH-PLA and an intercalated structure of NiAl/LDH-PLA were proposed.

The BDS measurements gave the total dielectric relaxation information about the neat PLA and the LDH-PLA nanocomposites. Both nanocomposites displayed three additional relaxation processes in comparison to the neat PLA. Relaxation region 1 was related to the fluctuation of SDBS surfactants in the interfacial region between the LDH layers and the PLA matrix, which behaved differently in MgAl/LDH-PLA and/or NiAl/LDH-PLA system. This anomolus behavior was due to the different presence situations of SDBS. Relaxation region 2 had an saddle-like temperature dependence for both nanocomposites, which was found relevant to the fluctuation of remaining water molecules in nanoporous structure of LDH-PLA nanocomposites. Relaxation region 3 was observed at temperatures higher than the characteristic dynamic glass transition temperature. It was assigned to interfacial polarizations effects due to the blocking of charge carriers at the nanofiller. DC conductivity ( $\sigma_{DC}$ ) of MgAl/LDH-PLA was found three orders of magnitude higher than that of the NiAl/LDH-PLA nanocomposite. Moreover, Maxwell/Wagner/Sillars polarization showed a stronger influence on the real part of complex dielectric function for MgAl/LDH-PLA than NiAl/LDH-PLA system. The two behaviors could be interpreted by the increasing blockage from more charge carriers and the releasing of more conduction ions. Both of them were due to the more exfoliated structure of MgAl/LDH-PLA nanocomposites.

## Zusammenfassung

Diese Arbeit konzentriert sich auf die vergleichende Analyse von Poly (L-lactid) (PLA) Nanokompositen auf Basis von modifizierten MgAl und NiAl geschichteten Doppelhydroxiden (LDH). Die Charakterisierung der Materialien erfolgte durch Gel-Permeations-Chromatographie (GPC), Dynamische Differenzkalorimetrie (DSC), Klein- und Weitwinkel-Röntgenstreuung (SAXS und WAXS) und Dielektrische Relaxations Spektroskopie (BDS).

Die polymerbasierten Nanokomposite wurden durch das Mischen in der Schmelze hergestellt. Die GPC-Messungen zeigten für beide Nanokomposite einen beschleunigten Abbau von PLA. Wobei die NiAl/LDH-PLA-Nanokomposite einen stärkeren Abbau als das MgAl/LDH-PLA-System aufwiesen. Diese Unterschiede konnten den unterschiedlichen Eigenschaften von Mg- und Ni-Ionen zugeordnet werden.

Die unmodifizierten und modifizierten Strukturen von MgAl/LDH und NiAl/LDH wurden durch SAXS-Messungen charakterisiert. Die Größe und die Dispersion der modifizierten LDHs (MgAl/LDH-PLA und NiAl/LDH-PLA Nanokomposite) unterschieden sich, was durch die Eigenschaften der verschiedenen Nanofüllstoffe erklärt wurde.

Der Kristallisationsgrad, wurde in Abhängigkeit von der LDH-Konzentration mit DSC gemessen und stimmt mit den WAXS Ergebnissen für beide Nanokomposite überein.

Auf der Grundlage des Dreiphasen-Modells für semikristalline Polymere, wurde PLA in eine kristalline (CF) und in eine amorphe Phase unterteilt. Die amorphe Phase wurde wiederum in eine mobile amorphe (MAF) und in eine starre amorphe Phase (RAF) geteilt, wobei die MAF am Glasübergang zur Stufe in der Wärmekapazität beiträgt und die RAF nicht. Laut Literatur, setzt sich die RAF in semikristallin PLA Nanokompositen zum einen aus RAF durch Nanofüllstoff ( $RAF_{\text{filler}}$ ) und anderen aus RAF durch Kristallisation ( $RAF_{\text{crystal}}$ ) zusammen. Für die Trennung der verschiedenen Teile der RAF wurden zwei Experimente durchgeführt. Im ersten Schritt wurde die kritische Abkühlungsrate bestimmt, um die Kristallisation von PLA während des Kühlprozesses zu unterdrücken und somit die Formierung von  $RAF_{\text{crystal}}$  zu verhindern. Im zweiten Schritt wurde mit der amorphisierten Probe der Beitrag zur Stufe in der Wärmekapazität am Glasübergang durch die Messung mit Temperatur modulierter DSC (TMDSC) gemessen um so  $RAF_{\text{filler}}$  zu erhalten. Anhand der Messungen von  $RAF_{\text{all}}$ , MAF und CF wird die Analyse der beiden RAFs in Abhängigkeit von LDH-Konzentrationen vorgenommen und ermittelt.

Das bemerkenswerteste Ergebnis waren die Unterschiede zwischen MgAl/LDH und NiAl/LDH-Systemen in der LDH-Konzentrationsabhängigkeit von dem Verhältnis von  $RAF_{\text{filler}}$  und Masse an Nanofüllstoff. Es konnte ein größerer Kontaktbereich des Füllstoffes mit PLA-Segmenten für MgAl/LDH-Nanokomposite abgeleitet werden. Daher wurde eine teilweise exfolierte Struktur für MgAl/LDH-PLA und eine interkalierte Struktur für NiAl/LDH-PLA angenommen.

Die BDS-Messungen lieferten die gesamte dielektrische Relaxationsinformation der PLA- und LDH-PLA-Nanokomposite. Beide Nanokomposite zeigten drei zusätzliche Relaxationsprozesse im Vergleich zu dem reinen PLA. Der Relaxationsbereich 1 wurde Fluktuationen von SDBS-Tensiden im Grenzflächenbereich zwischen den LDH-Schichten und der PLA-Matrix zugeordnet, die sich in MgAl/LDH-PLA und/oder NiAl/LDH-PLA-System unterschiedlich verhielten. Dieses unterschiedliche Verhalten wurde auf die unterschiedlich vorliegende SDBS Struktur zurückgeführt. Der Relaxationsbereich 2 hatte eine sattelartige Temperaturabhängigkeit für beide Nanokomposite, was für die Fluktuationen von verbleibenden Wassermoleküle in der nanoporösen Struktur von LDH-PLA-Nanokompositen sprach. Der Relaxationsbereich 3 wurde bei Temperaturen beobachtet, die höher waren als die charakteristische dynamische Glasübergangstemperatur. Dieses wurde durch Grenzflächenpolarisationseffekte aufgrund der Blockierung von Ladungsträgern am Nanofiller erklärt. Die DC-Leitfähigkeit ( $\sigma_{DC}$ ) von MgAl/LDH-PLA war drei Größenordnungen höher als die des NiAl/LDH-PLA-Nanokomposites. Darüber hinaus zeigte die Maxwell/Wagner/Sillars-Polarisation einen stärkeren Einfluss auf den Realteil der komplexen dielektrischen Funktion von MgAl/LDH-PLA als das NiAl/LDH-PLA-System. Die beiden Verhaltensweisen wurden durch die zunehmende Blockade von mehr Ladungsträgern und der Freisetzung von leitenden Ionen erklärt, beides aufgrund der mehr exfolierten Struktur von MgAl/LDH-PLA-Nanokompositen.

# Chapter 1 Introduction

## 1.1 Polymer Nanocomposites

The advancement of polymer composites as a distinctive class of materials start since the mid-20th century. The main purposes to fabricate polymer composites through incorporation of additives is to obtain modification and enhancement of properties, cost reduction, improvement and control of processing<sup>1</sup>. The additives can be continuous, like long fibers or ribbons, or discontinuous, like short fibers or platelets. The primary parameters affecting the properties of polymer composites include, such as the nature of additives, the interaction between the different components within the system, the distribution of the additives in polymer matrix and also the preparation method. However, with incorporation of conventional fillers such as talc, calcium carbonate, fibers, etc, it often requires to add a large amount of fillers into the polymer matrix to achieve desirable improvements, whereas this ordinarily leads to some other defects such as brittleness and opacity<sup>2</sup>. The emergence of nanoscale polymer composites can overcome the above difficulty. A nanocomposite is defined as a composite material in which at least one dimensions of the matrix or additives is in the nanometer size scale ( $< 100 \text{ nm}$ )<sup>3</sup>. Due to the small size of the additives the surface to volume ratio is high, which results in a high value of an interfacial area between the polymer matrix and the nanoparticle<sup>4</sup>. The interfacial area/volume ratio between the matrix polymer and the nanofiller is crucial for the properties of the entire nanocomposite<sup>5</sup>. Even though the insightful understanding of the correlations between the interfacial area/volume ratio and properties of the polymer nanocomposites is still lacking. The fact that the polymer nanocomposites possess more significant improvement compared to macro- and micro-scale polymer composites is indisputable. Some emerging applications of polymer nanocomposites include enhanced mechanical properties, barrier properties, electrical conductivity and flame retardancy, high-performance materials with improved UV absorption, barrier packaging for reduced oxygen degradation, bioactive components for tissue engineering application. The employed nanofillers include nanoclays, nanosilicates, carbon nanotubes (CNTs), modified graphene, ultrafine  $\text{TiO}_2$ , talc, and hydroxyapatite.

Although the conventional polymers nanocomposites will continue to propel the promising properties of materials<sup>6</sup>, it is more exciting to envision the synthesized polymer nanocomposites materials can be built into a hierarchically ordered nanocomposites, as

found in nature like bone, a composite of collagen and other proteins gluing calcium phosphate crystals, or shells of mollusks, that are made of layers of hard aragonite separated by a protein binder.

## **1.2 Motivation of this work**

This work focuses on the complementary analysis of layered double hydroxide (LDH) based poly (L-lactide) nanocomposites mainly by the combination of small- and wide-angle X-ray scattering (SAXS and WAXS), conventional and temperature modulated differential scanning calorimetry (DSC and TMDSC) and broadband dielectric spectroscopy (BDS). The adopted nanofiller LDH is a synthetic clay with a structure derived from brucite ( $\text{Mg}(\text{OH})_2$ ). One of the features of LDHs material is the ability in a wide range to select different metal hydroxide layer and charge-balancing interlayer anion via simple synthetic strategies. Meanwhile, it has a high chemical purity and a homogenous structure. The disadvantage of LDHs compared to other smectite clay materials is its high anion exchange capacity, the typical value reaches 200 mequiv. per 100g, for montmorillonite (MMT) this value is about 100 mequiv. per 100g.<sup>7</sup> Therefore, LDHs have more obstacles to achieve a fully exfoliated state in the polymer matrix compared to smectite clays. Due to the close-packed  $-\text{OH}$  ions on the lattice plane and resultant bound water molecules, LDHs based polymer nanocomposites normally have enhanced thermal stability and reinforced flammability properties without halogen. For its outstanding dispersion condition<sup>8, 9, 10, 11</sup> and versatile combinations between metal hydroxides and organomodified surfactants, LDHs based polymer nanocomposite is a desirable objective to study the structure-property relationships of polymer nanocomposites.

The BDS has advantages in studying dynamics behavior of polymer materials for its convenience, comprehensiveness and universality. The analysis of nanocomposites is mainly applied by investigating the influence of LDH nanofillers on polymer dynamics in comparison with the neat polymer matrix. In parallel, some minutiae such as the relaxation of organomodified surfactants, the conductivity of the nanocomposites system and morphology phase structure can also be revealed in detail. Coupling with other characterization techniques, an insightful landscape of intrinsic mechanism of polymer nanocomposites can be obtained.

### **1.3 Structure of the thesis**

This thesis is divided into seven chapters. Chapter 1 gives the introduction of polymer nanocomposites and the motivation of the work. The simple concepts of polymer nanocomposites and the significance to investigate this topic are supplied.

Chapter 2 focuses on the fundamental principles of adopted materials in this thesis. Which provide the detailed introduction of the layered double hydroxide (LDH) and the progress of LDH based polymer nanocomposites. For an explicit comprehension of the relationship between the polymer molecular mobility and the nanofiller dispersion, some knowledge about the polymer dynamics is explicated. In addition the relevant three phase model describing polymer morphology of semicrystalline polymers is introduced.

Chapter 3 gives the principles of applied characterization techniques. Three short paragraphs about differential scanning calorimetry (DSC), small- and wide-angle X-ray scattering and broadband dielectric spectroscopy are presented.

Chapter 4 is the experimental section where the source and preparation information of materials are given, in addition the experimental details are described here.

Chapter 5 and Chapter 6 mainly depict the analysis of the polylactide nanocomposites based on MgAl/LDH and NiAl/LDH from various aspects. Specially a comparison between the two polymer nanocomposites is made based on the observed intrinsic structure information.

The final chapter gives the conclusion about the investigation results, in parallel an outlook of this research field is presented.



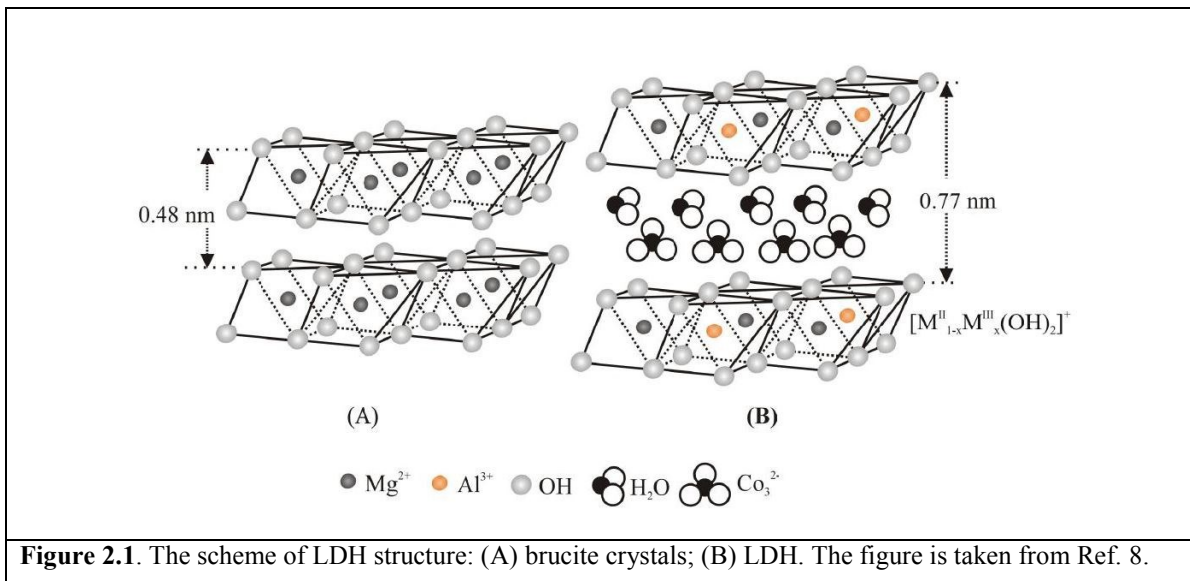
## Chapter 2 Scientific Background

### 2.1 Layered Double Hydroxide

Layered double hydroxides (LDHs) are a class of ionic lamellar compounds consist of positive charged brucite-like layers and an interlayer region containing charge compensating anions molecules<sup>12</sup>. The metal part structure of LDHs is analogous with the mineral brucite<sup>13</sup>. The schematic analogy between the brucite and the LDH structure is shown in Figure 2.1. The brucite is of the  $\text{CdI}_2$  type structure, which consists of magnesium ions compassed octahedrally by hydroxide ions. These octahedral units of hydroxide ions form infinite layers by edge-sharing<sup>14</sup>.

The metal hydroxide sheets in brucite crystal are neutral charged and stacked one another by Van der Waals interaction, the space between the layers is about 0.48 nm. In LDH, some of the divalent cations in brucite sheets are isomorphously substituted by a trivalent cation. The metal hydroxide layer formula transforms from  $\text{Mg}(\text{OH})_2$  into  $[\text{M}^{\text{II}}_{1-x}\text{M}^{\text{III}}_x(\text{OH})_2]^{x+}$ . Instead of the charge neutrality of neat brucite, the metal hydroxide sheet of LDHs is positive charged. The extra charge on the metal hydroxide layers is neutralized by the anions located between the positive charged layers. The interlayer region in LDHs also contains some water molecules for the stabilization of the crystal structure. So the general chemical formula of LDHs is written as  $[\text{M}^{\text{II}}_{1-x}\text{M}^{\text{III}}_x(\text{OH})_2]^{x+}(\text{A}^{n-})_{x/n} \cdot y\text{H}_2\text{O}$ , where  $\text{M}^{\text{II}}$  is a divalent metal ion, such as  $\text{Mg}^{2+}$ ,  $\text{Ca}^{2+}$ ,  $\text{Zn}^{2+}$ , etc.;  $\text{M}^{\text{III}}$  is a trivalent metal ion, such as  $\text{Al}^{3+}$ ,  $\text{Cr}^{3+}$ ,  $\text{Fe}^{3+}$ ,  $\text{Co}^{3+}$ , etc.; the  $x$  is the molar portion of trivalent cations to the total cation content should be between 0.2 and 0.4, and  $\text{A}^{n-}$  is an anion, such as  $\text{Cl}^-$ ,  $\text{CO}_3^{2-}$ ,  $\text{NO}_3^-$ , etc<sup>8</sup>. The presence of anions and water molecules leads to an expansion of interlayer space from 0.48 nm in brucite to about 0.77 nm in MgAl/LDH (see the Figure 2.1).

In contrast to other layered silicate clay materials, which retains negative charged layers and cationic interlayer species (also called cationic clay), the possession of anionic interlayer species in LDHs opens a door for compositional variation with a wide range of organic anionic molecules. On the basis of different application purposes, manifold molecules tailed with anionic group are adopted including organic surfactants (carboxylates and sulfonates<sup>15</sup>), pharmaceuticals (diclofenac, ibuprofen and naproxen) and biomolecules (DNA, nucleotieds and  $\beta$ -cyclodextrins)<sup>16</sup>. The variations of the anion in LDHs can be done by the direct synthesis or by post-synthetic anion exchange<sup>17</sup>.



Due to the anion exchange property, the LDHs layers can be delaminated by modification with various functional anionic molecules. And the delaminated LDHs (LDH nanosheets) can be used for preparations of core-shell multifunctional materials, self-assembling monolayers (SAM) and LDHs polymer nanocomposites<sup>7</sup>.

Besides their compositional flexibility and delamination ability, the distribution of divalent and trivalent cations within the LDH nanosheet is verified to be extremely homogeneous, which can be one of the advantages for applications as catalysts and catalyst precursors<sup>10</sup>. Another advantage is the pillaring property. LDHs can form the pillared-layered structure (PLS)<sup>18</sup> in the course of immobilizing large molecules between the LDH nanosheets. The PLS can introduce micropores into the LDHs, which presents LDHs with specific surface areas up to *ca.* 400 m<sup>2</sup>g<sup>-1</sup>.

Furthermore, through thermal treatment (calcination) at the temperature above about 200 °C, the LDH materials can be converted into an amorphous mixed metal oxides (MMOs). The chemical composition of the MMOs is predetermined by the composition of the cationic layers in the LDH structure. Through multistep thermal treatments the formation of the MMOs is completed at *ca.* 580 °C by decomposing interlayer anions. It is noteworthy that after thermal treatment if heated to a certain temperature (usually from 200 to 500 °C) the LDH structure will re-establish because of exposure to water steams. The LDHs can be transformed into the original structure by the dissolution in a aqueous solution of certain lost interlayer anions also. This feature is called “memory effect” of LDHs. This effect seems to be especially pronounced in Mg/Al LDHs and can facilitate the modification of the morphological and catalytic properties of the LDHs<sup>19</sup>.

## 2.2 Polymer nanocomposites based on LDH

The pretreatment of LDHs can be made through the direct synthesis or anionic exchange<sup>3,20</sup>. The degree of compatibilization of the nanocomposites is dependent on the interaction between the polymer matrix and the layers<sup>21</sup>. Most of the strategies can be classified into *in situ* polymerization, melt-mixing, and solution blending. The *in situ* polymerization provides a solution of the monomer and interlayer gallery is intercalated by these monomer molecules. After that, a catalyst is added to the solution and monomers start to polymerize *in situ*. The polymerization occurs in the interlayer gallery and ruptures the structure of layered crystalline then produces an exfoliated dispersion of the LDHs layers. This method can promote a high exfoliated state of the layered particles.

The melt-mixing method are more environment compatible than other methods due to the avoidance of organic solvents. The melt-mixing method incorporates LDH nanofiller in polymer matrix at rather high temperatures and imposes high local shear stresses in a melt-mixer, such as twin-screw extruders. In this process, the structure of nanocomposites strongly depends on the degree of intercalation of the polymer segments in the interlayer gallery and presents intercalated or exfoliated state. The solution blending method is carried out with polymer and fully dispersed LDHs dissolved in a good solvent. The solvent is evaporated followed by the precipitation of the polymer incorporated between the interlayer galleries. The difficult point of this method is to find a suitable solvent to dissolve both the polymer and the LDH. The use of this method is for facilitating the preparation of thin films with low polar polymers and highly orientated LDHs.

The dispersion and alignment morphology of the LDH based polymer nanocomposites can be determined by X-ray diffraction (XRD) and by transmission electron microscope (TEM). In general, the three typical achieved morphologies are displayed in Figure 2.2<sup>3</sup>. For example, the part (a) of Figure 2.2 represents the dispersion state of nanofillers in the immiscible nanocomposite, actually the XRD pattern of mixed nanofillers is no different with the initial unmixed LDH, in the TEM image an agglomerate morphology is observed due to the tendency for nanoscale particle to coalesce. The part (b) depicts an intercalated structure in the nanocomposite, the peak shifts to the lower angles as a consequence of an enhanced LDH interlayer distance due to the incorporation of the polymer chains into the galleries. The corresponding TEM image gives isotropic dispersion morphology of integral LDH stacks. The exfoliated LDH structure is indicated by part (c), no obvious Bragg peaks can be found, because the periodic ordering of nanofiller is destroyed. The

TEM image shows the exfoliated structure, even single LDH layers dispersed homogeneously in the polymer matrix.

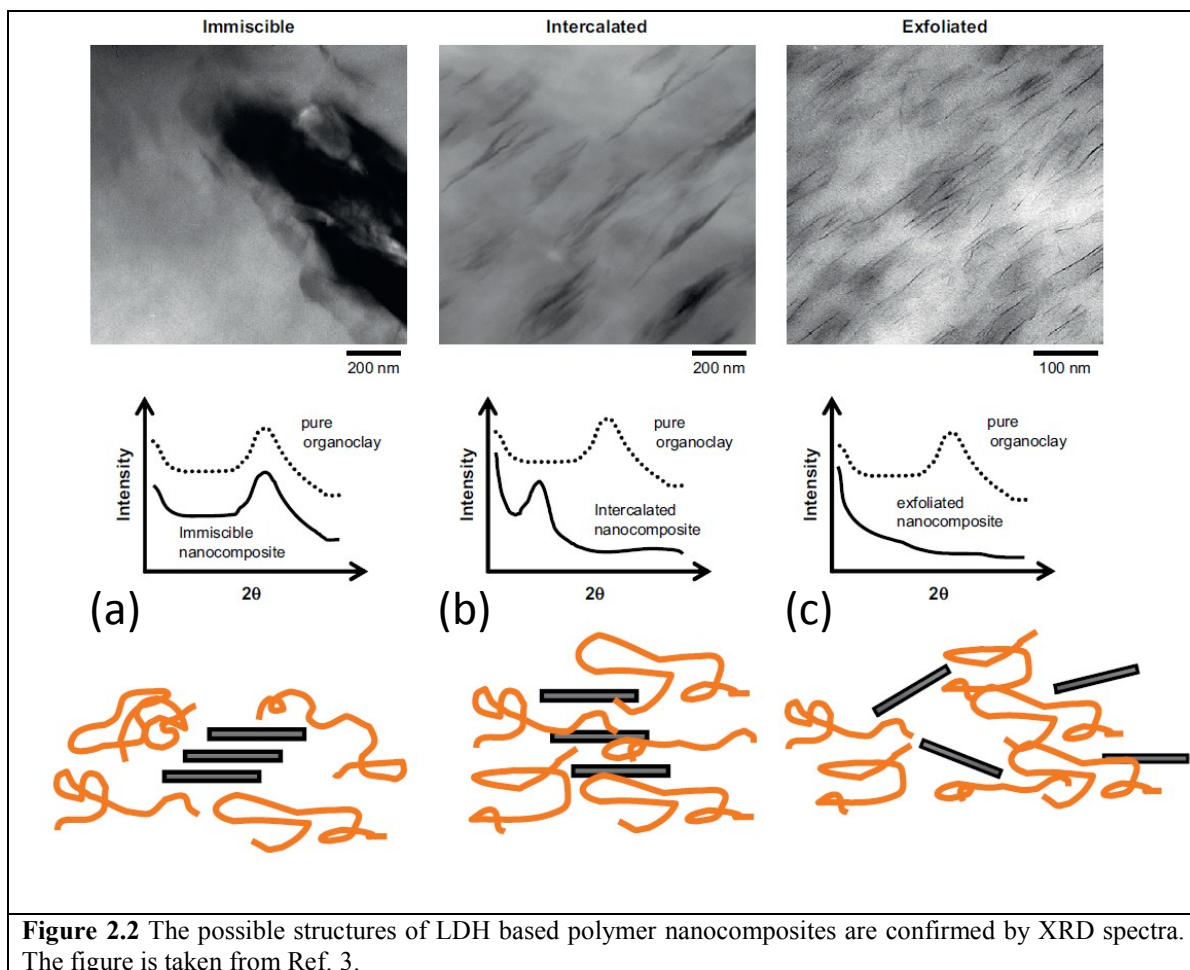


**Figure 2.2** The possible structures of LDH based polymer nanocomposites are confirmed by XRD spectra. The figure is taken from Ref. 3.

Several factors influence the exfoliation extent of LDH fillers, like the nature of interlayer, for example the density charge capacity and the type of cations, the type of the incorporated interlayer anion and size, the nature of polymer matrix and preparation method adopted. Even the concentration of the particles in the polymer matrix play a role.

The incorporation of LDH exerts reinforcement influence on mechanical property of polymer matrix. For the large surface area of LDH, in some case reaches  $800 \text{ m}^2/\text{g}$ , there are large potential interactions with the polymer molecules, the significant improvement of mechanical modulus are expected even for a small amount of nanofillers. Typically, the low amount of LDH incorporation leads to an increase of Young's modulus and the tensile strength. But the higher concentration of LDH induces the regression of the mechanical properties because with increasing concentration the particle aggregation takes place and hinder the better dispersion in polymer matrix as for the low LDH contents. Sorrentino *et al.*<sup>22</sup> reported with 2.8 wt% LDH particle in poly( $\epsilon$ -caprolactone) based nanocomposite

both Young's modulus and yield stress increased about 100%. However, up to 6 wt% the mechanical properties were decreasing. The similar behavior was observed in PU/DS-LDH nanocomposites<sup>23</sup>, the maximum enhancement of tensile strength and elongation at break were found at a concentration of 3 wt% DS-LDH. Except the concentration factor, the nature of the polymer matrix, the modification by the interlayered organic anion and the adoption of compatibilizer also play important roles on mechanical reinforcement.

The thermal stability of the polymer matrix also can be also enhanced by incorporating LDH nanofiller<sup>24</sup>. The enhancement in thermal stability can be attributed to the prevention of LDH layers from diffusion of oxygen and volatile products in the polymer matrix, and to the formation of a char layer after the organic matter decomposition. Moreover, the host metal hydroxide layer gives an additional cooling effect during its endothermic decomposition, which could retard the combustion process. Although there are rare literatures<sup>25,26</sup> claimed a decreasing decomposition temperature compared to pure polymer matrix, the reinforcement effect of LDH on polymer matrix thermal stability is generally accepted.

Recently, with increasing interest in LDH based polymer nanocomposites, several promising applications are reported. Lu *et al.*<sup>27</sup> fabricated a novel thin film nanocomposite membrane for forward osmosis based on LDH nanoparticles and polysulfone. The incorporation of LDH endowed the ultrafiltration substrate with high water permeability as compared to the pristine FO membrane. Kapusetti *et al.*<sup>28</sup> found poly(methyl methacrylate)-based LDH nanocomposites bone cement performed better growth of human osteoblast cells as compared with pure bone cement and could be a potential biomaterial for implants surgery. Mahkam *et al.*<sup>29</sup> introduced a nanocomposite in combination with LDH and a pH-sensitive polymer which is able to act as a drug delivery system controlling the release of insulin effectively.

In conclusion, the great versatility of LDHs and the abundant selectivity of polymer matrix support LDH-polymer nanocomposite to be a promising multifunctional material.

## **2.3 Relaxation phenomena in polymers**

### **2.3.1 Four dynamics regions of the polymer system in dependence on temperature**

A polymer is composed of high weight molecules and the simple phase definition is not suitable to describe it. The basic phase states for low molecular weight compounds are crystalline, liquid and gaseous. But before vaporizing to a gaseous state, the polymer will

start to decompose. Many kinds of polymer do not crystallize at all but form a glassy state at low temperature. At higher temperatures they convert into a viscoelastic melt. The corresponding transition from glassy state to the viscoelastic state is called glass-rubber transition.

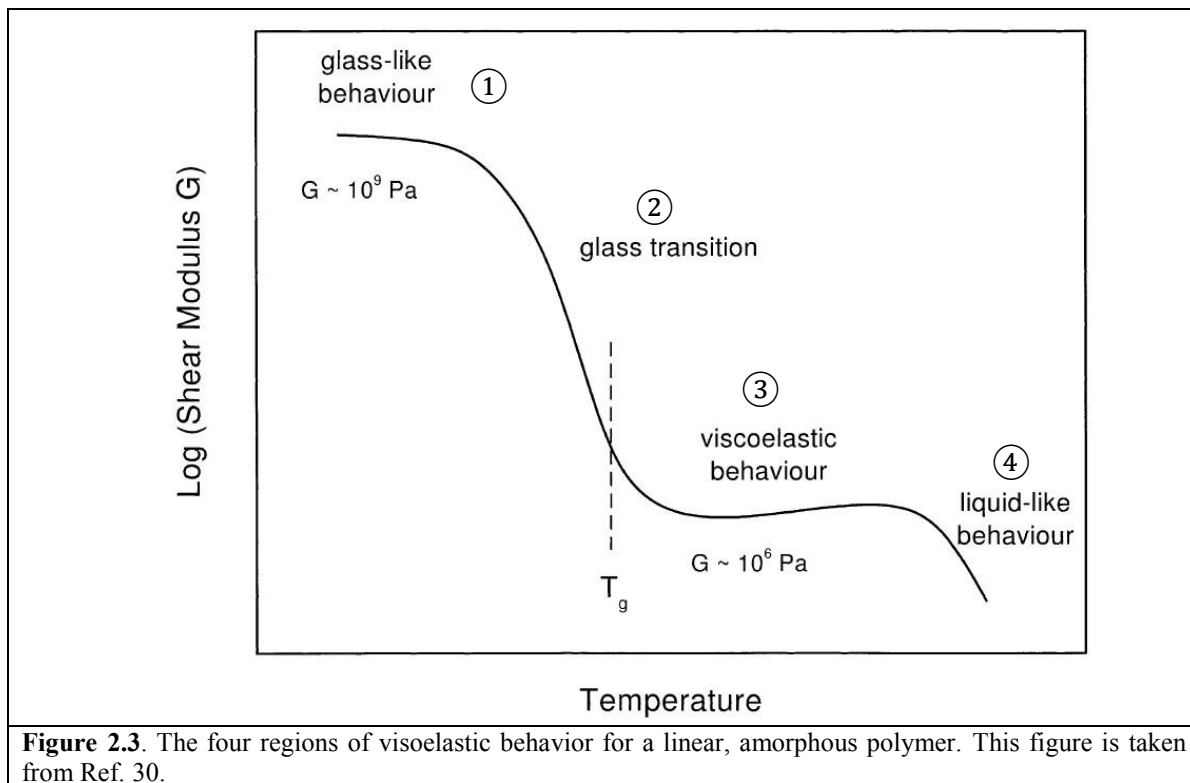


**Figure 2.3.** The four regions of viscoelastic behavior for a linear, amorphous polymer. This figure is taken from Ref. 30.

Depending on the dynamics behavior of the linear amorphous polymer with increasing temperature, there are four different regions (as shown in Figure 2.3) being observed.

Represented by the shear modulus, the curve of polymer in region 1 (below glass transition temperature) displays a plateau and the molecular motions are largely restricted to the vibration and short-range rotational motions. The polymer behaves like a glassy solid and the shear modulus is in the order of magnitude of  $10^9$  Pa. And this regions is indicated as the glassy region. With rising temperature, the polymer comes to the region 2 which depicts the glass transition region, typically the modulus can drop three orders of magnitude within a temperature range of 20 to 30 K. The glass transition is one of the most important feature for polymer based materials, it can be interpreted as the onset of the segmental motion. Below the glass transition temperature  $T_g$  only 1 to 4 atoms in a chain participate in motions, while 10 to 50 segments can move in a coordinated manner in the glass transition region<sup>31, 32, 33, 34</sup>. The glass transition temperature ( $T_g$ ) can be taken for instance at the maximum rate of turndown of the modulus at the elbow. Often the  $T_g$  is

defined as the temperature where the thermal expansion coefficient experiences a change in its temperature dependence. For the crystalline polymer, because of the crystallization restraint the amount of polymer participating in the glass transition is much smaller than the amorphous one. Therefore, the significant reduction of shear modulus will be observed after the melting of crystalline polymers.

For temperatures higher than  $T_g$ , the system becomes viscoelastic and rubberlike, this is region 3 the rubbery plateau region. The value of shear modulus of polymer in this region keep constant again with a typical value around  $2 \times 10^6$  Pa. The plateau is due to entanglements in the flexible polymer whose molecular weight is higher than a critical molecular weight  $M_C$ . For most flexible polymers the value of  $M_C$  is about  $10^4$  g/mol. A higher molecular weight leads to a longer plateau. The special case in region 3 is crosslinked polymers for the creep portion in higher temperature range is suppressed due to the covalent bonding between polymer chains.

Up to the temperature range of regions 4, the polymer behaves like an ordinary fluid. At such high temperature the polymer chains obtain a further more increased mobility and permit them to reptate out through entanglements so that the shear modulus tends to a lower value.

### **2.3.2 The glass transition**

Although the dynamics behaviors of polymer exist in all above four regions. The actual analysis of our as prepared polymer nanocomposites primarily focus on glass transition region. To describe glass transition, some thermodynamic quantities are involved such as volume  $V$  and enthalpy  $H$  (as shown in Figure 2.4(a)). At a definite cooling rate, the glass-forming material presents a well-defined change in the slopes of the temperature dependence of the volume or enthalpy

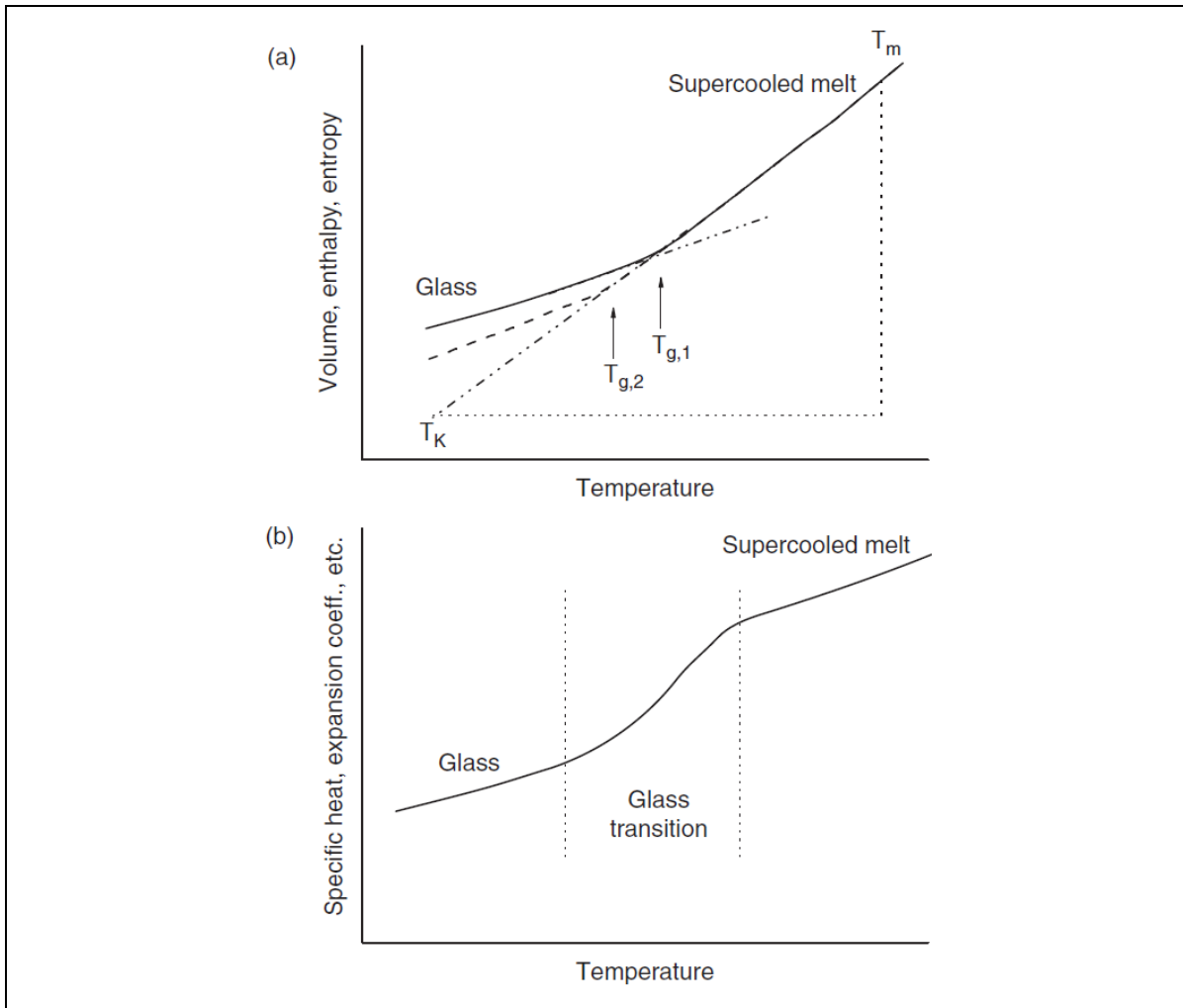


**Figure 2.4.** (a) At two different cooling rates  $R_1 > R_2$ , the glass transition temperature range performs differently  $T_{g,1}$  and  $T_{g,2}$  on thermodynamic quantities like volume, enthalpy, or entropy in dependence on temperature.  $T_m$  indicates hypothetical melting temperature for semicrystalline polymers,  $T_K$  denotes Kauzmann temperature. (b) The steplike changes of temperature dependences during the glass transition process. The figures are taken from Ref.35.

occurs. And the temperature dependence of the corresponding first derivatives such as the specific heat capacity  $c_p = (\partial H / \partial T)_p$  and the thermal expansion coefficient  $\alpha = (1/V)(\partial V / \partial T)_p$  are observed (see Figure 2.4(b)). This phenomenon is called thermal glass transition. For the state of the polymer above  $T_g$  it can be considered as “supercooled” whereas below  $T_g$  the state of polymer is the glassy state. Due to the steplike changes in the polymer properties ( $c_p$  and  $\alpha$ ), the glass transition is analogous to second-order thermodynamic phase transitions. However, the formal classification cannot be made because: (1) the Keesom-Ehrenfest relationships<sup>36,37</sup> which is fulfilled for a second-order phase transitions but is not valid for the glass transition<sup>38,39,40</sup>, and (2) the value of  $T_g$  is a convention and depends on both the timescale of the experiment and the applied method, moreover the supercooled state is a thermodynamically metastable equilibrium state while

the glass is a nonequilibrium state. The latter means below  $T_g$  the properties of glass depend on time. This phenomenon is called physical aging.<sup>41</sup>

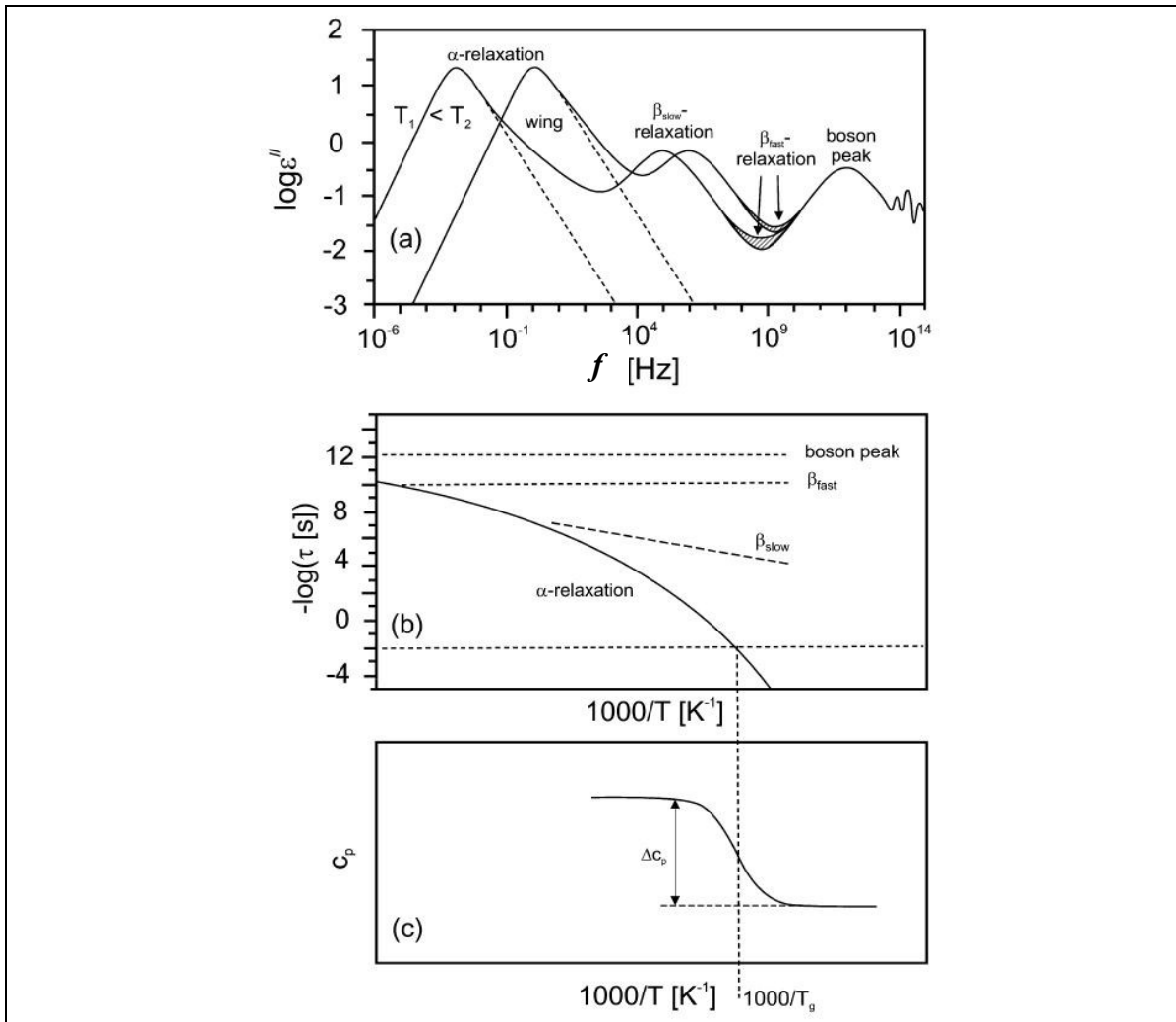


**Figure 2.5.** Scheme of the dynamics taking place in amorphous polymer systems. (a) Imaginary part  $\epsilon''$  of the complex dielectric function vs. frequency for two temperatures  $T_1$  and  $T_2$ . (b) Relaxation map (relaxation rate vs. inverse temperature) for different processes. (c) Thermal glass transition where the specific heat capacity vs. inverse temperature is plotted. The picture is taken from Ref. 36.

It is worth noting if the curve of temperature dependence of entropy below  $T_g$  is extrapolated to zero value, at a certain temperature  $T_K$ , the extrapolated entropy will be lower than the corresponding (hypothetic) crystal (see Figure 2.4(a)). This is the well-known Kauzmann paradox<sup>42</sup>. To resolve the Kauzmann paradox, several theories are proposed such as Adam-Gibbs theory<sup>43</sup> and random first order transition theory<sup>44</sup> (RFOT) through different aspects.

The changes in the thermodynamic quantities or their first derivatives are only one landscape concerning the complex process of glass formation. A second important point focuses on the molecular dynamics in glass-forming systems such as amorphous polymers. This behavior can be observed by a variety of methods like mechanical-dynamical

spectroscopy<sup>26</sup>, ultrasonic spectroscopy<sup>45, 46</sup>, light spectroscopy<sup>47, 48</sup> and neutron scattering<sup>49</sup>, nuclear magnetic resonance spectroscopy (NMR)<sup>50, 51</sup>, specific heat spectroscopy (SHS)<sup>52, 53, 54</sup> and broadband dielectric spectroscopy (BDS)<sup>55</sup>. (Note there is a huge body of literatures in this field. The given references are only examples.) Figure 2.5(a) gives a schematic overview about the dynamical processes at different time scales, the corresponding relaxation map of above dynamical processes is shown in Figure 2.5(b), where relaxation rate  $f$  characterizes dynamical processes and equals  $1/\tau$ . The onset part of  $\alpha$ -relaxation are in agreement with the data characterizing thermal glass transition with specific heat capacity in Figure 2.5(c). The  $\alpha$ -relaxation is also called dynamic glass transition which is due to segmental fluctuations related to conformational changes in polymer systems. With decreasing temperature, the relaxation time increases substantially the temperature dependence of relaxation rate can be approximated by the empirical Vogel-Fulcher-Tammann (VFT) equation<sup>56, 57, 58</sup>

$f_p(T) = f_\infty \exp\left(-\frac{DT_0}{T - T_0}\right)$	(2.1)
--	-------

where  $T_0$  is called Vogel or ideal glass transition temperature which is found 30-70 K below  $T_g$ . It is worth noting the values of  $T_0$  is found to be close to that of the Kauzmann temperature  $T_K$ . The prefactor  $f_\infty$  ( $f_\infty \approx 10^{10}$ - $10^{12}$  Hz) and  $D$  are constants.  $D$  is so-called fragility parameter and can be used to classify glass-forming systems<sup>59, 60</sup>.

Another analogous representation of the VFT equation to describe the  $\alpha$ -relaxation of amorphous polymers is the Williams-Landel-Ferry (WLF) relation.<sup>61</sup>

$\alpha_T = \log \frac{f(T)}{f(T_{Ref})} = -\frac{C_1(T - T_{Ref})}{C_2 + T - T_{Ref}}$	(2.2)
---	-------

Equation 2.1 and 2.2 are mathematically equivalent.  $T_{Ref}$  is a reference temperature and  $f(T_{Ref})$  is the value of the relaxation rate at this temperature.  $C_1$  and  $C_2 = T_{Ref} - T_0$  are so-called WLF parameters.  $\alpha_T$  is the shift factor which is obtained by the ratio of viscosity  $\eta_T/\eta_{Ref}$ . It was argued that these parameters should have universal values which are independent of materials if  $T_g = T_{Ref}$  is chosen. However, these estimates are found to be only rough approximations. Nevertheless, the WLF equation is quite often used in

mechanical spectroscopy to analyze relaxation data in the frame of a master curve construction.

Most amorphous polymers show, in addition to the dynamic glass transition, a slow  $\beta$ -relaxation. The temperature dependence of its relaxation rate follows an Arrhenius-type equation

$f_p(T) = f_\infty \exp\left(-\frac{E_A}{k_B T}\right)$	(2.3)
---	-------

where  $E_A$  is the activation energy,  $k_B$  the Boltzmann constant, and  $f_\infty$  the relaxation rate in the high temperature limit. In history, the  $\beta$ -relaxation of amorphous polymers was considered as the relaxation behaviors from rotational fluctuations of side groups or other localized parts of the main chain. However, in some special cases such as main chain polymers 1,4-polybutadiene<sup>62</sup>, poly(ethylene terephthalate)<sup>63</sup>, or poly(propylene glycol)<sup>64</sup> this explanation is unconvincing apparently. Another approach is proposed by Johari and Goldstein<sup>65, 66</sup>, it argued that the  $\beta$ -relaxation is a generic feature of glass transition and amorphous state, and can be regarded as a precursor of the glass transition. The  $\beta$ -relaxation process can be observed also for various low molecular mass glass-forming liquids.

A further molecular process takes place in the THz region. It means an excess contribution to Debye vibrational density of states (VDOS) and is called Boson peak<sup>67</sup>. Even the relationship between the Boson peak and fluctuations of elastic constants was discussed, its molecular interpretation is still controversial.

### 2.3.3 The theories describing glassy dynamics of polymers

To describe the glass transition problem, several theories are proposed through different aspects. Too elaborate elucidations of those difficult approaches are beyond the scope of this chapter, here only two classical theories will be introduced ---the free volume theory and the cooperativity approach.

The postulation of free volume related to glass transition was first developed by Fox and Flory<sup>68</sup>. And the theoretical improvement was actualized by Doolittle<sup>69</sup> and Cohen<sup>70, 71</sup>. The fundamental assumptions of the free volume theory are: (i) For each molecule there is a molecular scale volume  $V$ ; (ii) when  $V$  exceeds the critical value  $V_c$ , the excess part can be considered as free volume  $V_f$ ; (iii) the molecular mobility occurs only the  $V_f$  is larger

than a critical value  $V^*$  which approximate the molecular volume  $V_m$ , and (iv) there is no expense of free energy is required for the redistribution of  $V_f$ .

In the statistics of free volume, the jump rate  $1/\tau$  is expressed by

$\frac{1}{\tau} \sim \int_{V^*}^{\infty} \exp\left[-\frac{V_f}{\bar{V}_f}\right] dV_f \sim \exp\left[-\frac{V^*}{\bar{V}_f}\right]$	(2.4)
---	-------

where  $\bar{V}_f$  is the averaged free volume. Assuming that the relative averaged free volume  $\bar{f} = \bar{V}_f/V$  ( $V$ : total volume) has a linear dependence on temperature.

$\bar{f} = f_g + \alpha_f(T - T_g)$	(2.5)
-------------------------------------	-------

while  $f^* = V^*/V$  is temperature independent results in a VFT-equation.  $\alpha_f$  is the thermal expansion coefficient of the free volume and  $f_g$  the relative free volume at  $T_g$ . Compared to Equation 2.1,

$DT_0 = \frac{f^*}{\alpha_f} \qquad T_0 = T_g - \frac{f_g}{\alpha_f}$	(2.6)
---	-------

where  $T_0$  is the temperature at which  $\bar{V}_f$  vanishes in the framework of the free volume concept.

There are several techniques to measure the free volume of polymers experimentally, such as positron annihilation lifetime spectroscopy (PALS)<sup>72, 73, 74</sup>, inverse gas chromatography (IGC)<sup>75, 76</sup> and Xe NMR spectroscopy<sup>77</sup>. However, the data provided by different methods do not agree with each other if their absolute values are compared. The free volume theory remains qualitative. Also no characteristic length is involved, the jump between holes is the only transport mechanism, therefore it is hard to understand complex phenomena for example the decoupling of segmental and chain dynamics by this model.

The cooperatively rearranging regions (CRRs) were introduced by Adam and Gibbs<sup>78</sup> as an essential concept in cooperativity approach. A CRR can be considered as the smallest volume which can vary its configuration unrelatedly to the neighboring regions. If per CRR has an average number of segments  $z(T)$ , then the relaxation rate is expressed as

$\frac{1}{\tau} \sim f_p = \exp\left(-\frac{z(T)\Delta E}{k_B T}\right)$	(2.7)
--	-------

where  $\Delta E$  is a free energy barrier for a conformational change of a segment.  $z(T)$  is given by  $z(T) = S_C(T)/(Nk_B \ln 2)$  where  $S_C(T)$  is the total configurational entropy,  $N$  is the total number of segments and  $k_B \ln 2$  is the minimum of entropy of CCR assuming a two-state model.

Donth<sup>76</sup> extended the CRR theory with the use of fluctuation approach of glass transition. If consider  $\xi$  as the radius of a CRR sphere, this leads to the correlation length at  $T_g$  is given directly with experimental thermal parameters:

$\xi^3 = \frac{3}{4\pi} \frac{k_B T_g^2 (\Delta c_p^{-1})}{\rho \delta T^2}$	(2.8)
--	-------

where  $\rho$  is the density of bulk material and  $\Delta c_p^{-1}$  is the step height of reciprocal specific heat capacity at the glass transition where  $c_v = c_p$  was assumed,  $\delta T$  can be extracted from the width of the glass transition<sup>57, 79</sup>,  $k_B$  is the Boltzmann constant. Recently, the correlation length of CRR was measured by DSC<sup>80</sup> and SHS<sup>81, 82</sup>, it was estimated in the range of 1-3 nm and corresponds to 10-200 segments based on several polymers.

## 2.4 Three phase model of the semicrystalline polymer

Due to the influence from the long chain molecule, the maximal degree of polymer crystallization ranges between 10 and 80%, therefore the crystallized polymers are often called “semicrystalline polymer”. The basic building unit in polymer crystals is lamellar crystals, which are in a length scale above the crystal unit cell. It is surprising to find that, a broad range of crystalline polymers form lamellar crystals through chain folding.<sup>83</sup> The lamellar crystals aggregates to form a larger length scale of morphology, after crystallization from melt, a common observation of this morphology is spherulites<sup>84, 85, 86</sup> (see Figure 2.6). The degree of polymer crystallization can be measured by wide angle X-ray diffraction, density, and DSC experiments. Among these methods, thermal analysis techniques are the most essential for equilibrium melting data determination.

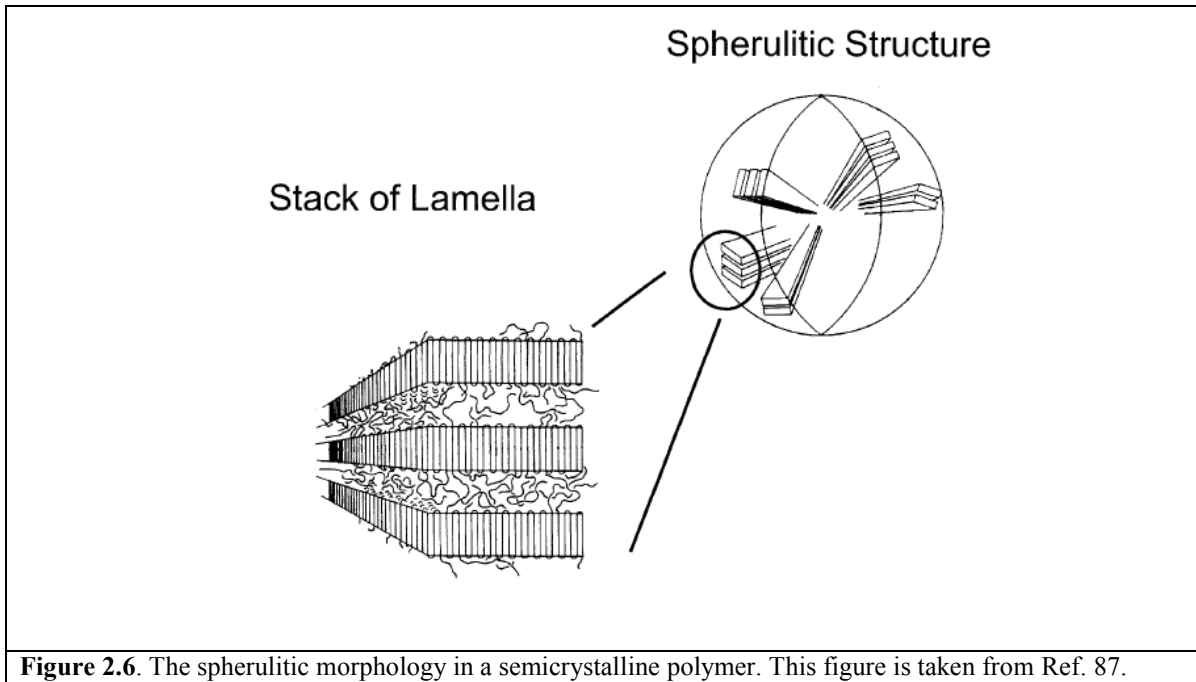


**Figure 2.6.** The spherulitic morphology in a semicrystalline polymer. This figure is taken from Ref. 87.

Resembling amorphous polymers, the non-crystalline part of semicrystalline polymers contributes to the glass transition relaxation strength. In history, the entire morphology of semicrystalline polymers is described by the so-called “two-phase model”<sup>88</sup> which consists of the crystalline and the non-crystalline fraction. Nevertheless, the observed experimental evidences by DSC technique<sup>69</sup>, dielectric spectroscopy<sup>89, 90, 91</sup>, shear spectroscopy<sup>92</sup> and NMR<sup>93</sup> indicate the non-crystalline fraction obtained from the relaxation strength at glass transition is smaller than the one calculated by eliminating the crystallinity. Thus, the amorphous fraction is considered to be composed of two components. The one causing the glass transition is called the mobile amorphous fraction (MAF). The additional fraction no contribution to the glass transition is called rigid amorphous fraction (RAF). For the reason of the production of RAF, the scale of polymer chains must be taken into account. The thickness of the lamella is in the order of several decade nanometers, folded by the polymer chains possessing a typical length of 1-100  $\mu\text{m}$ <sup>94</sup>, the frequent crossing on the interfaces of crystallite and amorphous phases is inevitable. These crossings produce a strong coupling between both interfaces, and results in a broadening of the glass transition to higher temperature. The first recognition of the existence of RAF was made by Wunderlich, et al.<sup>95</sup>, which was considered as a deficiency in  $\Delta c_p$  at  $T_g$  and then confirmed quantitatively as an RAF for polyoxymethylene<sup>96</sup>.

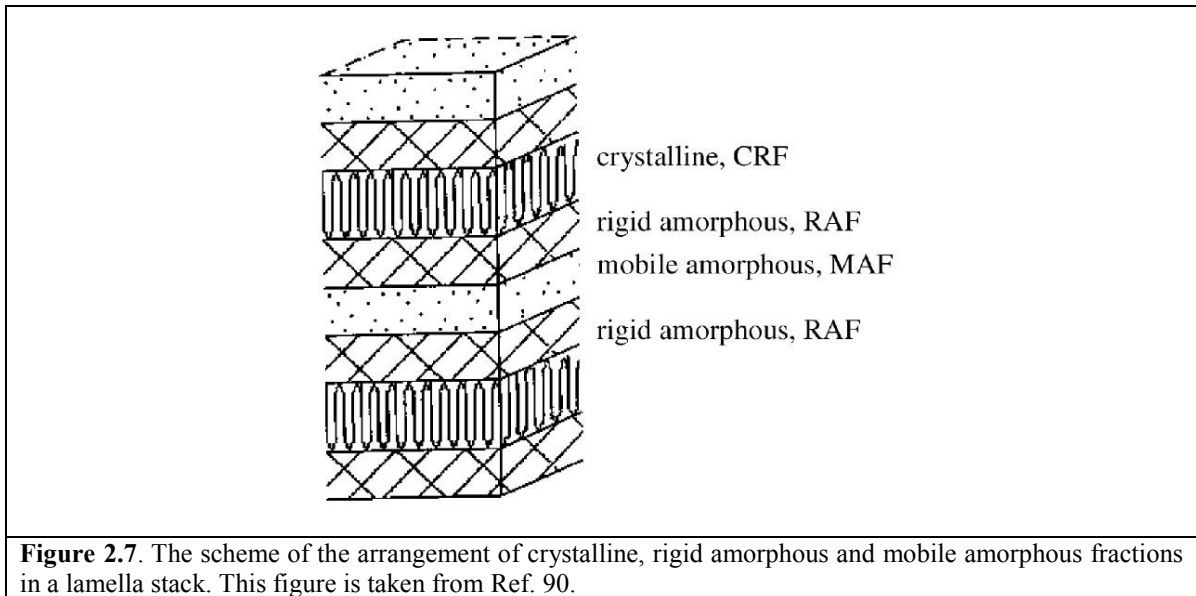


**Figure 2.7.** The scheme of the arrangement of crystalline, rigid amorphous and mobile amorphous fractions in a lamella stack. This figure is taken from Ref. 90.

The new “three-phase model” including RAF was built by Schick, et al.<sup>97</sup> However, for the determination of RAF, which still needs to get the value of crystalline fraction (CF) and MAF firstly and subtract the two known values from the unity.<sup>98,99</sup>

The RAF is not only found in pure semicrystalline polymer systems, Sargsyan<sup>100</sup> et al. discovered in a amorphous polymer nanocomposites system of poly(methyl methacrylate) (PMMA)/SiO<sub>2</sub> there were the RAF caused by the SiO<sub>2</sub> nanofillers. The RAF is demonstrated as a 2 nm thick immobilized layer on the surface of nanofillers. Compared to the concomitant disappearance of the RAF in semicrystalline polymers as the crystallization fuses, the nanofiller seems to be a stable carrier for the RAF. There is no signal for the RAF to devitrificate before degradation of the PMMA. Depending on such character, the RAF due to nanofiller can be regarded as a constant value in polymer nanocomposites systems.

For a more complex system like semicrystalline polymer nanocomposites, on the basis of reported literatures, the RAF can be separated into the RAF caused by the crystallization and the RAF resulted from the nanofiller. To give a complete description of the morphology of polymer nanocomposites, the determinations of different RAFs is necessary. An attempt to calculate the value of different RAFs in PLA based nanocomposites system was made in our recent work<sup>101</sup>.



## Chapter 3 Principles of characterization techniques

### 3.1 Differential Scanning Calorimetry

#### 3.1.1 Conventional differential scanning calorimetry

Differential scanning calorimetry (DSC)<sup>102, 103, 104, 105</sup> is an effective analytical tool to investigate the physical properties of materials via measuring the corresponding thermal responses. Commonly, the DSC locates two sample positions, one for the sample under investigation and the other for a reference sample. The original measurement signal is a temperature difference  $\Delta T$  between the sample and the reference which is given as a voltage<sup>103</sup>. On the basis of the analysis of the heat flow rate  $\Phi$  assigned to  $\Delta T$ , DSC enables determination of melting, crystallization, and glass transition temperature, and the corresponding enthalpy and entropy changes. The relationships of the measured  $\Phi$  and derived values such as heat capacity  $C$ , enthalpy  $H$  and entropy  $S$  are given in what follows:

$\Phi = \frac{dQ}{dt} = C_p \cdot \frac{dT}{dt} = c_p \cdot m \cdot \beta$	(3.1)
$H = \int_0^T C_p dT$	(3.2)
$S = \int_0^T \frac{C_p}{T} dT$	(3.3)

where  $dQ$  is the heat exchanged,  $C_p$  is the heat capacity at constant pressure,  $c_p = C_p/m$  is the corresponding specific heat capacity,  $m$  is the sample mass, and  $\beta$  is the scan rate (heating or cooling).

There are at least two types of DSC: the heat flux DSC and the power compensation DSC for the conventional DSC measurement<sup>106</sup>. For the power compensation DSC, the temperature difference between the sample and reference is maintained constant as the sample is scanned, the heat flow is determined by the compensating power. Whereas in a heat flux DSC, the temperature difference is allowed to vary, with the equation  $\Phi = dT/R$  the signal is converted to heat flow, where  $R$  is the thermal resistance of thermoelectric disk. Regarding precision, the two-dimensional and the three-dimensional measurement systems are involved<sup>107</sup>.(as shown in Figure 3.1) In a two-dimensional measurement

system, the sample may exchange heat directly with the surrounding oven which is not measured by the heat flow sensor, this leads to a loss of 50% of the total heat flow rate exchanged<sup>108</sup>. The three-dimensional measurement systems avoids this problem through the sensing element. To a very good approximation, 94% of the exchanged heat is measured which is realized by the Tian-Calvet type heat flux DSC. Another quasi three-dimensional measurement system with very short response time was introduced by Watson and O'Neill<sup>109, 110</sup>, the accuracy of heat capacity of such power compensating DSC may reach 0.5% under perfect experimental conditions.

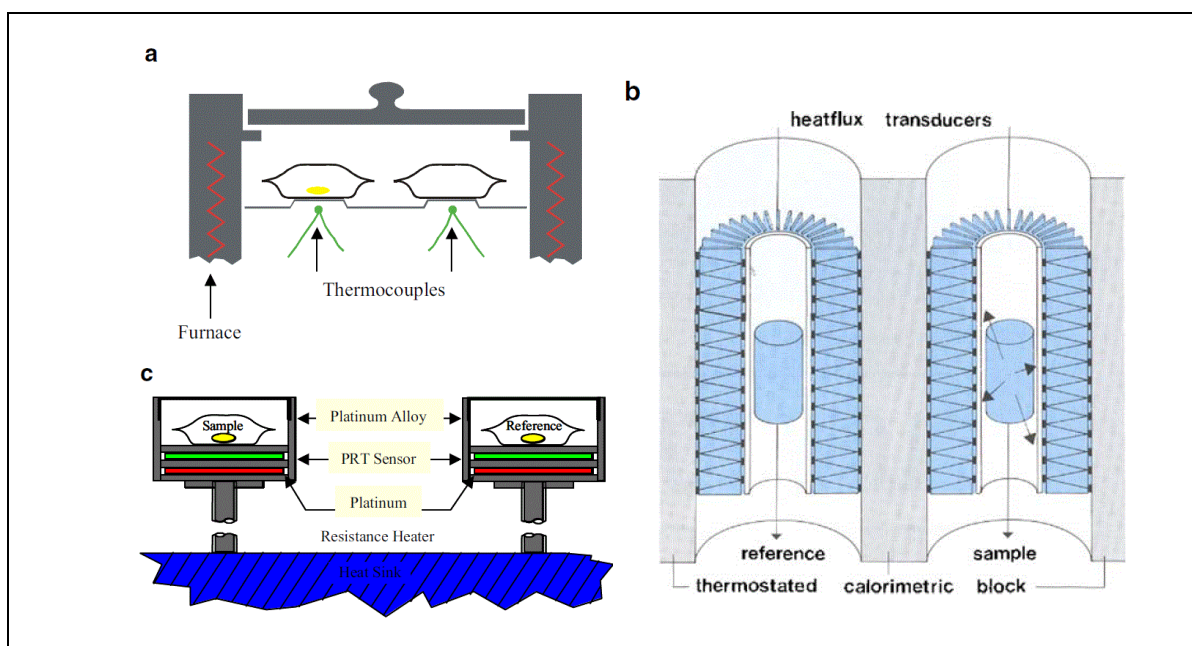
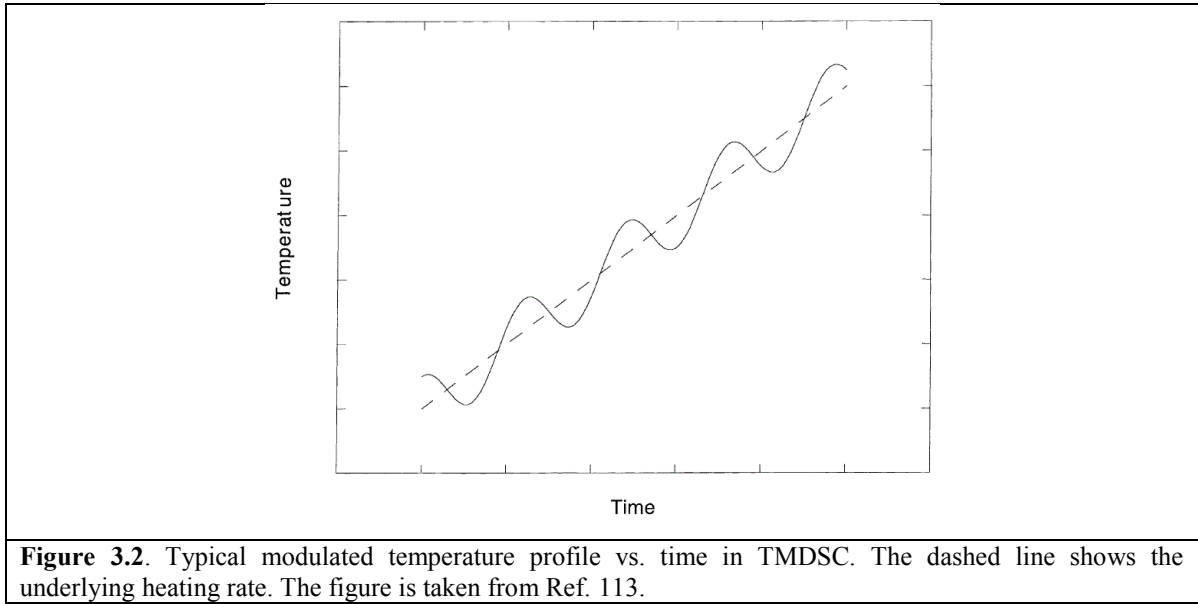


**Figure 3.1.** The schemes of different types of differential scanning calorimeters (DSC). (a) two-dimensional plate like; (b) three-dimensional cylindrical (Tian-Calvet); (c) three-dimensional with power compensation. The figure is taken from Ref. 107.

### 3.1.2 Temperature modulated differential scanning calorimetry

The technique of temperature modulated differential scanning calorimetry (TMDSC) was first proposed by Reading<sup>111, 112</sup> and co-workers. The TMDSC applies a low-frequency sinusoidal or nonsinusoidal (e.g. sawtooth) perturbation ranging from approximately 0.001 to 0.1 Hz on the baseline temperature profile (as shown in Figure 3.2).



For the mathematical analysis a Fourier-transform analysis measuring the amplitude of the response to the temperature modulation is needed. As a typical modulated temperature profile,

the  $T(t)$  can be described as<sup>114</sup>

$T(t) = T_0 + \beta t + A_T \sin(\omega t)$	(3.4)
---	-------

where  $T_0$  is the initial temperature,  $\beta$  is underlying heating or cooling rate,  $A_T$  is amplitude of temperature perturbation and  $\omega$  is angular frequency with  $\omega = 2\pi/t_p$ ,  $t_p$  is the modulation period. If give the first order derivative of Equation 3.4 with respect to  $t$  into Equation 3.1

$\frac{dQ}{dt} = C_p(\beta + \omega A_T \cos \omega t)$	(3.5)
---	-------

For the special case where  $\beta$  is zero, then  $dQ/dt = C_p \omega A_T \cos \omega t$ . Also the resultant heat flow rate can be indicated as  $dQ/dt = A_{HF} \cos \omega t$ , where  $A_{HF}$  is the amplitude of the heat flow modulation. So the reversing heat capacity is

$C_{p \text{ reversing}} = \frac{A_{HF}}{\omega A_T}$	(3.6)
---	-------

where  $\omega A_T$  can be regarded as the amplitude of the modulation in the heating rate oscillation. The total heat capacity equals the average total heat flow is divided by the underlying heat rate  $\beta$ . Thus,

$C_{p\ total} = \frac{\langle dQ/dt \rangle}{\beta}$	(3.7)
--	-------

Then the non-reversing heat capacity is calculated by

$C_{p\ non-reversing} = C_{p\ total} - C_{p\ reversing}$	(3.8)
--	-------

This analysis procedure can be regarded as the simple deconvolution (see Figure 3.3), because it doesn't take the phase lag  $\varphi$  between the modulation in the heat flow and the heating rate into account. In a more complex deconvolution,<sup>115, 116, 117</sup> the phase lag is used to calculate the in- and out-of-phase components of the reversing heat capacity

$C_{p\ reversing} \cos\varphi = C'_p = \textit{phase corrected reversing heat capacity}$	(3.9)
$C_{p\ reversing} \sin\varphi = C''_p = \textit{kinetic heat capacity}$	(3.10)
$C_{p\ reversing} = \frac{A_{HF} e^{-i\varphi}}{\omega A_T} = C'_p - iC''_p$	(3.11)

Which processes contributing to the reversing heat capacity depends strongly on the measuring conditions.<sup>118</sup> For example, the non-reversing latent heats on melting contribute to the reversing heat capacity depending on the ratio of heating rate amplitude and underlying heating rate.

However, the use of sinusoidal wave in TMDSC imposes a short time cooling of each period on the sample during the measurement, which complicates the analysis. Additionally, the input of time-temperature sinusoidal wave cannot ensure a steady sinusoidal heat flow response from the sample. The resultant sinusoidal heat flow wave can be distorted and this

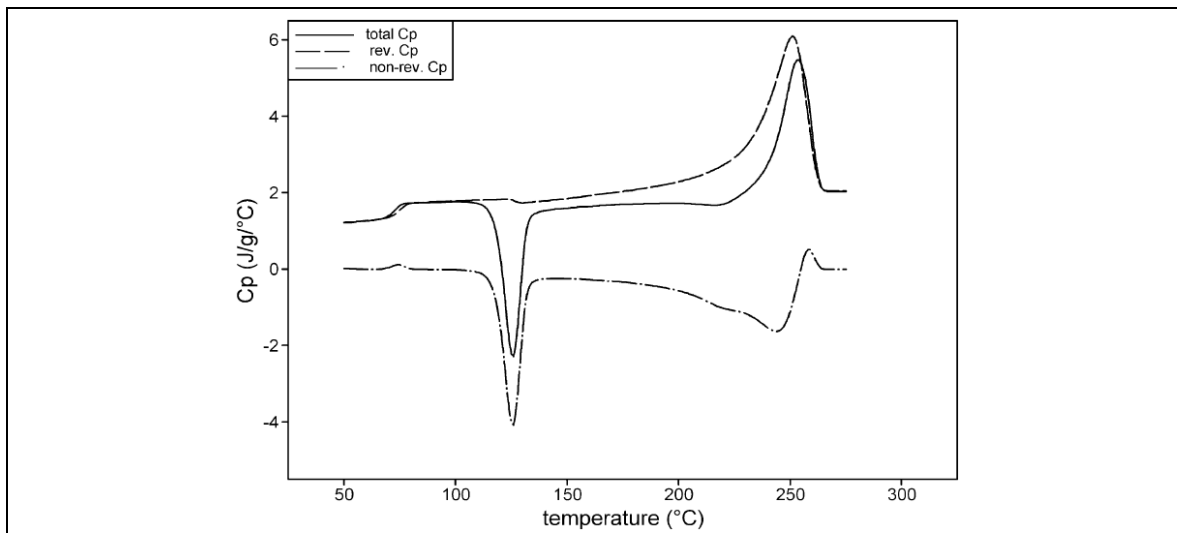


**Figure 3.3.** The total, reversing and nonreversing signals of simulated TMDSC for deconvolution procedure. The figure is taken from Ref. 114.

cannot handled by the TMDSC analysis software<sup>119</sup>. The above problems would not appear in the stepscan mode, which was introduced by Perkin-Elmer Instruments for power-compensated DSCs. It can be regarded as a variant of TMDSC, after raising the sample temperature, for example, by 0.5 K at a high heating rate (step-like, as shown in Figure 3.4) the temperature will be held again. Due to the very short duration for each step, the measurement of the thermodynamic heat capacity with stepscan DSC is not sensitive to baseline drifts, even at the highest accessible temperatures. Also the data treatment is straightforward, no Fourier transformation is needed<sup>120, 121</sup>.

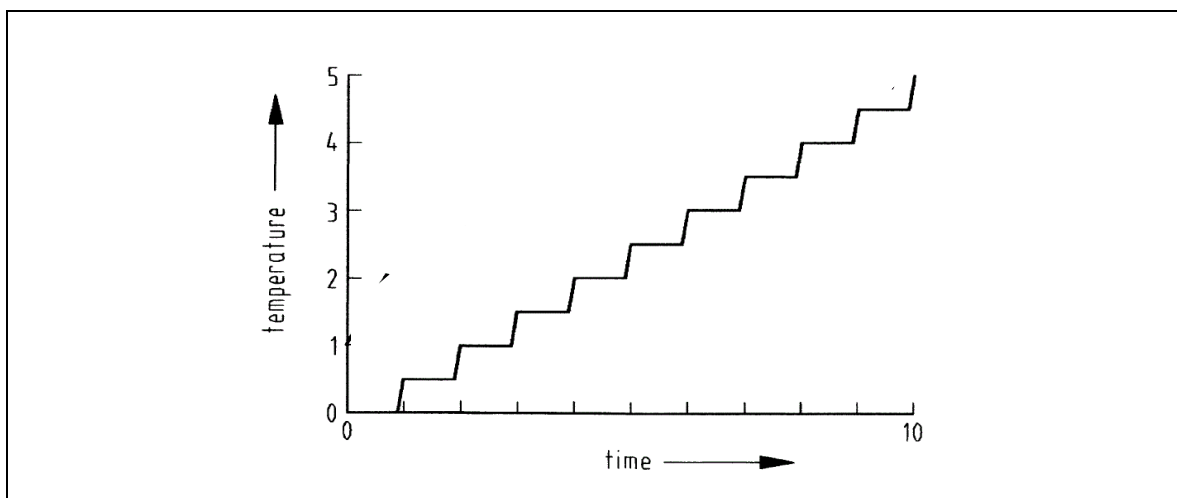


**Figure 3.4.** A stepscan temperature-modulated modes. The figure is taken from Ref. 122.

### 3.2 Small- and Wide- angle X-ray Scattering

The fundamental principle of X-ray scattering follows Bragg's law (as shown in Equation 3.12),

$n\lambda = 2d\sin\theta$	(3.12)
---------------------------	--------

where  $\lambda$  is the wavelength of the radiation used,  $d$  is the inter-planar spacing involved and  $\theta$  is the angle between the incident ray and the scattering crystal planes;  $n$  is a positive integer. The  $2d\sin\theta$  is the path difference of the X-ray scattering, the path difference is the light scattering from one plane of atom lattice subtracts that scatters from the last upper plane of atom lattice inside a sample. If the path difference equals an integer number of wavelengths,

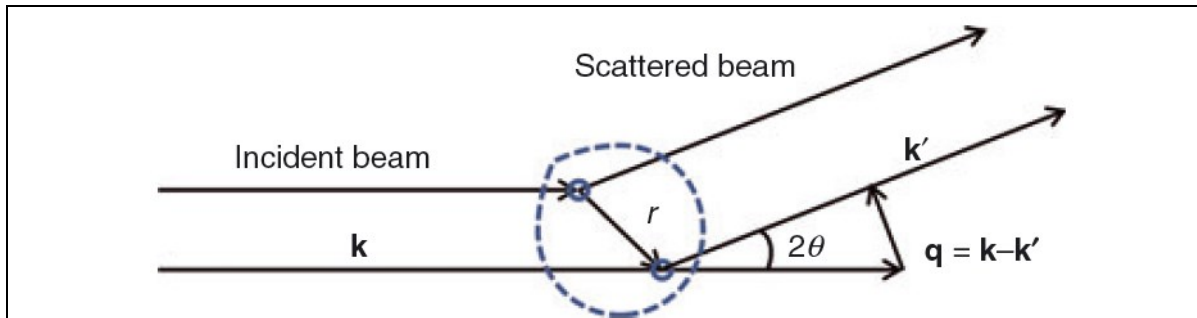


**Figure 3.5.** The scheme of X-ray scattering. The incident beam with wavevector  $\mathbf{k}$  is scattered at the angle  $2\theta$  by two scattering centers with distance of  $r$  and the resultant beam has a wavevector  $\mathbf{k}'$  with the same modulus but different direction. The figure is taken from Ref.123.

the intensity of X-ray will be reinforced, this is the basic idea of Bragg's law. Figure 3.5 gives the geometry of X-ray scattering experiment, when a sample is illuminated by a plane wave of wavevector  $\mathbf{k}$  with a modulus  $2\pi/\lambda$ , in an elastic scattering phenomena the modulus of the scattering wavevector  $\mathbf{k}'$  is unchanged with respect to the incident one and the scattering vector  $\mathbf{q} = \mathbf{k} - \mathbf{k}'$ , its modulus can be indicated by

$q = 4\pi\sin\theta/\lambda$	(3.13)
------------------------------	--------

The scattering techniques using X-rays are extremely useful to study the structure, size and shape of large molecules such as polymers in solids, liquids and solutions with dimensions from micrometers to angstroms<sup>124</sup>. The wide-angle X-ray scattering (WAXS) is particularly used to identify the nature of crystalline phases on an atomic scale. Small-angle X-ray scattering (SAXS) is normally used to analyze the structure of materials on a

scale of about 1-200 nm.<sup>125</sup> For both types of measurement, the sample is illuminated by a narrow beam of well-collimated monochromatic X-rays as a radiation source. The main difference between SAXS and WAXS on the instrument is the distance of detector to the sample. The scattering angle  $2\theta > 1^\circ$  refers to as WAXS, those with  $1^\circ > 2\theta > 0.3^\circ$  are medium-angle X-ray scattering (MAXS), and those with  $2\theta < 0.3^\circ$  can be called SAXS. The crystallinity of polymers can be easily determined by calculating the area under crystalline peaks to the total scattered intensity in a WAXS scan<sup>126</sup>. The degree of crystallinity  $x_c$  is given:

$x_c = \frac{\text{Crystalline scattering area}}{\text{Total scattering area}} = \frac{A_c}{A_c + A_a}$	(3.14)
---	--------

where  $A_a$  is the area of the amorphous halo,  $A_c$  is the total area under Bragg peaks in a WAXS profile, after appropriate background corrections, this equation can be applied.

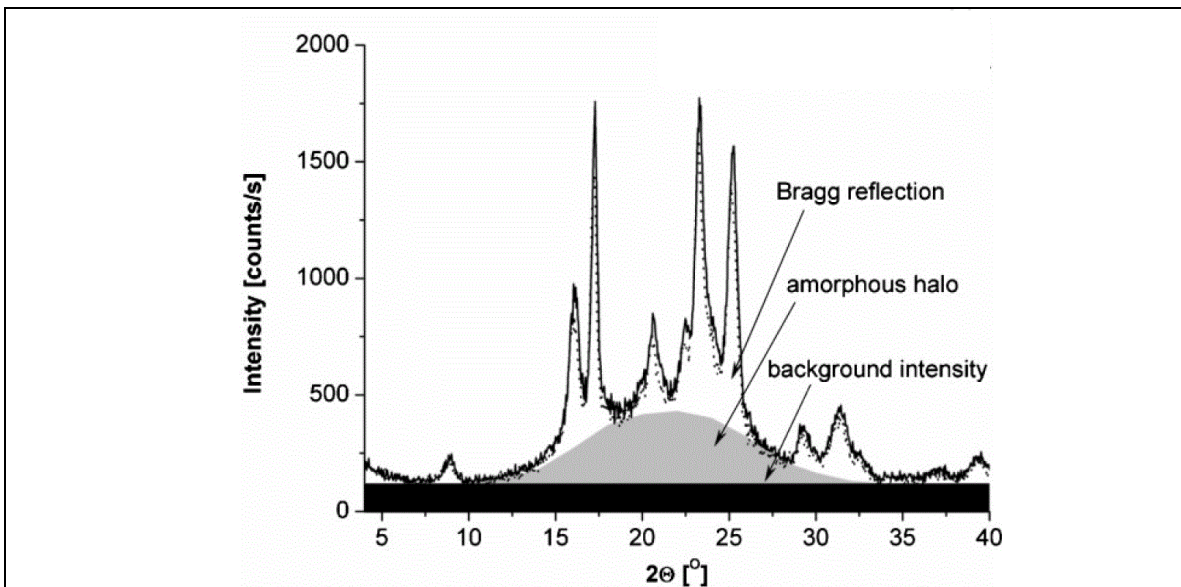


**Figure 3.6.** An example for the splitting of WAXS pattern to determine the crystallinity of polymer nano-composites. The figure is taken from Ref. 127.

The estimation of the size (at submicron level) of crystallite is related to the broadening of scattering peaks and described by Scherrer equation as

$\tau = \frac{K\lambda}{\beta_{1/2} \cos\theta}$	(3.15)
--	--------

where  $\tau$  is the mean size of the crystallite,  $\beta_{1/2}$  is the full-width at half-maximum (FWHM) of the scattering peak,  $K$  is the Scherrer constant (the value of which depends on the shape of the crystallite), and  $\theta$  is the angular position of the scattering plane.

According to Bragg's law, a scattering peak locating at  $q$  values of x-axis can be interpreted by the equation  $d = 2\pi/q_{peak}$ , where  $d$  indicates the distance of separation between scattering planes. Important morphological parameters such as long period ( $L$ ), crystal thickness ( $l_c$ ), and amorphous layer thickness ( $l_a$ ) of semicrystalline polymer can be calculated with the finite lamellar stacks model. For semicrystalline polymers these SAXS profiles can be analyzed via a combination of the correlation function  $\gamma(r)$  and the interface distribution function  $g(r)$ <sup>128, 129, 130</sup>. For the LDH based polymer nanocomposites, the dispersion state of LDH nanofillers is mainly determined by SAXS. The repeat distance between interlayers of LDH can be interpreted by  $q$  values of the primary scattering peak due to the LDH nanofiller platelet. Assuming the lattice distortions can be neglected<sup>131</sup>, the Bragg's law is applied directly to derive the LDH platelet's repeat distance  $d_{LDH} = 2\pi/q_{peak}$ . The Scherrer equation for quantifying finite size effects<sup>132</sup> in X-ray scattering is employed in assessing the thickness of LDH platelet stacks by its simplified mode  $l_c = 2\pi/w$ , where  $w$  is the full-width at half-maximum,  $l_c$  is the mean size of the platelet's thickness, this equation is actually the transformation of Eqn. 3.15 without Scherrer constant  $K$ .

### 3.3 Broadband Dielectric Spectroscopy

Broadband dielectric spectroscopy (BDS) is deals with the interaction of electromagnetic radiation with molecular systems. Normally, BDS describes two main phenomena occur under the applied electromagnetic radiation in the frequency range from  $10^{-6}$  to  $10^{12}$  Hz: (i) dipole relaxation resulting from the reorientational motions of molecular dipoles, (ii) electrical conduction resulting from the translational motions of electric charges (ions, electrons)<sup>47</sup>. For its extraordinary extended frequency range, the BDS technique provides us a wealth of information on the dynamics of dipoles and mobile charge carriers based on the details of molecular system. The objectives can be analyzed by BDS cover polymers, glass-forming liquids, liquid crystals, electrolytes, organic and inorganic semi-conductors.

#### 3.3.1 The principle of BDS

Here, basic principle of the dielectric spectroscopy will be provided. Firstly, for a small electric field  $E$ , the interaction between the electric field and the matter can be described by the displacement  $D$ :

$D = \varepsilon^* \varepsilon_0 E$	(3.16)
-------------------------------------	--------

where  $\varepsilon_0$  is the dielectric permittivity of vacuum ( $\varepsilon_0 = 8.854 * 10^{-12} \text{AsV}^{-1}\text{m}^{-1}$ ),  $\varepsilon^*$  is the complex dielectric function or dielectric permittivity.  $\varepsilon^*$  is time or frequency dependent and can be used to describe time dependent processes in the sample. In the dielectric scope, these time dependent processes mean relaxation phenomena from molecular fluctuations of dipoles and drift motion of mobile charge carriers. In general, these time dependent processes cause a phase shift of the time dependence between the outer electrical field  $E(t)$  and the resulting dielectric displacement  $D(t)$ . For a periodic electrical field  $E(t) = E_0 \exp(-i\omega t)$ , the corresponding  $\varepsilon^*$  can be defined by

$\varepsilon^*(\omega) = \varepsilon'(\omega) - i\varepsilon''(\omega)$	(3.17)
---	--------

where  $\varepsilon'(\omega)$  is the real part,  $\varepsilon''(\omega)$  is the imaginary part of the complex dielectric function and  $i$  is the imaginary unit.

### Electrostatic state

The macroscopic polarization  $\mathbf{P}$  can be related to microscopic dipole moments  $\mathbf{p}_i$  of the molecule or other units in a definite volume  $V$ .

$$\mathbf{P} = \frac{1}{V} \sum \mathbf{p}_i \quad (3.18)$$

where  $i$  counts all dipole moments in the system. For the dipole moment that can be defined as the electric centers of gravity of positive and negative charges do not match. For example a positive charge  $+q$  and a negative charge  $-q$  are separated by a distance  $d$  will cause the dipole moment  $\mathbf{p} = q\mathbf{d}$ . The microscopic dipole moments can be separated into permanent and induced dipoles. Electronic polarization is the typical induced polarization form where negative electron cloud is shifted with regard to the nucleus. The electronic polarization occurs within  $10^{-12}$  s, and similar atomic polarization takes place on a slightly longer time scale. For the sake of simplicity the above induced polarizations denote as  $\mathbf{P}_\infty$ . For permanent dipoles if only one kind of dipole moment  $\boldsymbol{\mu}$  of molecules is considered in a system, then Equation 3.18 becomes

$$\mathbf{P} = \frac{1}{V} \sum \boldsymbol{\mu}_i + \mathbf{P}_\infty = \frac{N}{V} \langle \boldsymbol{\mu} \rangle + \mathbf{P}_\infty \quad (3.19)$$

where  $N$  denotes the whole number of dipoles in the system and  $\langle \boldsymbol{\mu} \rangle$  is the mean dipole moment. The molecular permanent dipole moment  $\boldsymbol{\mu}$  can be oriented by an outer electrical field. Assuming the main factors are the interaction between permanent dipoles and the electric field strength. For the sake of simplicity two assumptions are made first that dipoles do not interact with each other and second that the local electrical field  $\mathbf{E}_{Loc}$  of dipoles is equal to the outer electrical field. If  $\langle \boldsymbol{\mu} \rangle$  is calculated by considering the counterbalance of thermal energy and the interaction energy  $W$  between a dipole and the electric field is given as  $W = -\boldsymbol{\mu} \cdot \mathbf{E}$ . So according to Boltzmann statistics<sup>133, 134</sup>,

$$\langle \boldsymbol{\mu} \rangle = \frac{\int_{4\pi} \boldsymbol{\mu} \exp\left(\frac{\boldsymbol{\mu} \cdot \mathbf{E}}{k_B T}\right) d\Omega}{\int_{4\pi} \exp\left(\frac{\boldsymbol{\mu} \cdot \mathbf{E}}{k_B T}\right) d\Omega} \quad (3.20)$$

where  $T$  is temperature,  $k_B$  is Boltzmann constant and  $d\Omega$  the differential space angle. The factor  $\exp(\frac{\mu \cdot E}{k_B T})d\Omega$  gives the probability that the dipole moment vector has an orientation from  $\Omega$  to  $\Omega + d\Omega$ . Only the dipole moment component parallel to the direction of outer electric field is taken into account for the polarization. So the interaction energy transforms into  $W = -\mu E \cos\theta$  where  $\theta$  is the angle of orientation between the dipole moment and the electrical field (see inset of Figure 3.7). Then the Equation 3.20 becomes

$$\langle \mu \rangle = \frac{\int_0^\pi \mu \cos\theta \exp(\frac{\mu E \cos\theta}{k_B T}) \frac{1}{2} \sin\theta d\theta}{\int_0^\pi \exp(\frac{\mu E \cos\theta}{k_B T}) \frac{1}{2} \sin\theta d\theta} \quad (3.21)$$

The part  $\frac{1}{2} \sin\theta$  indicate the component of space angle with  $\theta$  direction. Substituting  $x = (\mu E \cos\theta)/(k_B T)$  and  $a = (\mu E)/(k_B T)$ . One obtains

$$\langle \cos\theta \rangle = \frac{1}{a} \frac{\int_{-a}^a x \exp(x) dx}{\int_{-a}^a \exp(x) dx} = \frac{\exp(a) - \exp(-a)}{\exp(a) + \exp(-a)} - \frac{1}{a} = \Lambda(a) \quad (3.22)$$

where  $\Lambda(a)$  is the Langevin function. Because of the small value of the interaction energy of a dipole compared to the thermal energy  $\Lambda(a) \approx a/3$  holds. Then Equation 3.20 simplifies to

$$\langle \mu \rangle = \frac{\mu^2}{3k_B T} E \quad (3.23)$$

Substituting to Equation 3.19 yields

$$P = \frac{\mu^2}{3k_B T} \frac{N}{V} E \quad (3.24)$$

So in the form of dielectric function, the orientational polarization component is given as

$$\epsilon_s - \epsilon_\infty = \frac{\mu^2}{3\epsilon_0 k_B T} \frac{N}{V} \quad (3.25)$$

where  $\varepsilon_s = \lim_{\omega \rightarrow 0} \varepsilon'(\omega)$ .  $\varepsilon_\infty = \lim_{\omega \rightarrow \infty} \varepsilon'(\omega)$  covers all contributions from electronic and atomic polarization  $\mathbf{P}_\infty$  to the dielectric function. Keeping in mind that the two assumptions have been made one is the local electrical field is equal to outer electrical field, and the other is no interaction between permanent dipoles with each other. From the actual point of view both effects should be considered. The local electrical field  $\mathbf{E}_{Loc}$  can be described by Lorentz sphere model  $\mathbf{E}_{Loc} = \mathbf{E} + a_{Lor}(\mathbf{P}/\varepsilon_0)$  and for the Lorentz sphere the coefficient  $a_{Lor}$  is 1/3. The enhancement of the dipole moment by the polarization of the environment is given by Onsager by the reaction field theory. The resulting molecular dipole moment can be  $\mathbf{m} = \boldsymbol{\mu} + \alpha \mathbf{E}_{Loc}$  where  $\alpha$  is the polarizability. An Onsager factor is added to Equation 3.17:

$\varepsilon_s - \varepsilon_\infty = \frac{1}{3\varepsilon_0} F \frac{\mu^2 N}{k_B T V}$	(3.26)
---	--------

with  $F = \frac{\varepsilon_s(\varepsilon_\infty + 2)^2}{3(2\varepsilon_s + \varepsilon_\infty)}$ .

The interaction between permanent dipoles is considered with correlation factor  $g$  which is introduced by Kirkwood and Fröhlich<sup>135, 136, 137, 138</sup>. The Kirkwood/ Fröhlich correlation factor is defined by

$g = \frac{\langle \sum_i \boldsymbol{\mu}_i \sum_j \boldsymbol{\mu}_j \rangle}{N\mu^2} = 1 + \frac{\langle \sum_i \sum_{i < j} \boldsymbol{\mu}_i \boldsymbol{\mu}_j \rangle}{N\mu^2} = \frac{\mu_{interact}^2}{\mu^2}$	(3.27)
--	--------

where  $\mu^2$  is the mean square dipole moment for non-interacting isolated dipoles. Equation 3.18 modifies to

$\varepsilon_s - \varepsilon_\infty = \frac{1}{3\varepsilon_0} F g \frac{\mu^2 N}{k_B T V}$	(3.28)
---	--------

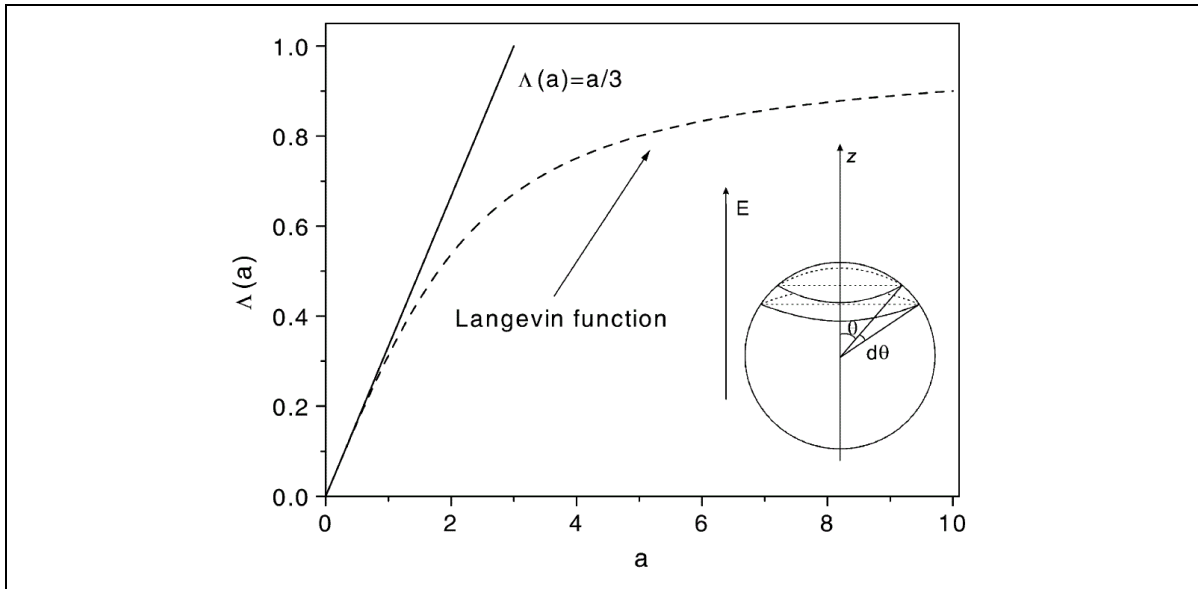


**Figure 3.7.** Dependence of the Langevin function  $L(a)$  on  $a$ . The scheme of the time dependence of electric field  $\Delta E$  and corresponding time dependent relaxation function  $\varepsilon(t)$ . The figure is taken from Ref. 55.

### Dielectric relaxation

The process of dipole reorientation due to time dependent external electrical field can be regarded as a special case of linear response theory. In dielectrics the disturbance is the time dependent external electrical field  $x(t) = E(t)$ , the response is the polarization  $y(t) = P(t)$ . With linear response theory the following can be obtained

$$P(t) = P_{\infty} + \varepsilon_0 \int_{-\infty}^t \varepsilon(t-t') \frac{dE(t')}{dt'} dt' \quad (3.29)$$

where  $\varepsilon(t)$  is the time dependent dielectric function and  $P_{\infty}$  covers all contributions from induced polarization. The corresponding relationship between  $E(t)$  and  $\varepsilon(t)$  is depicted in Figure 3.8.

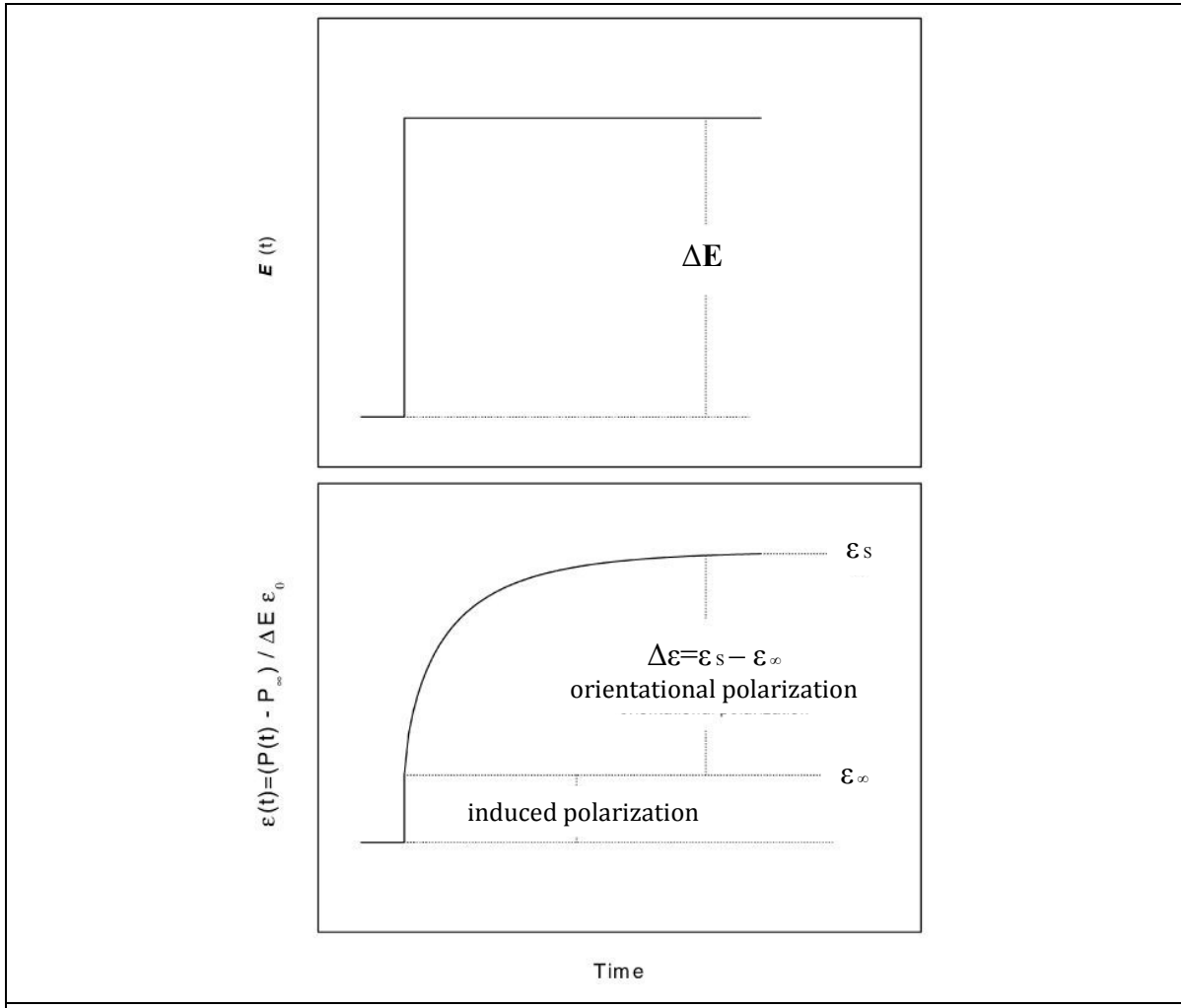


**Figure 3.8.** The scheme of the time dependence of electric field  $\Delta E$  and corresponding time dependent relaxation function  $\varepsilon(t)$ . The figure is taken from Ref. 55.

If a stationary periodic disturbance  $\mathbf{E}(t) = \mathbf{E}_0 \exp(-i\omega t)$  is applied to the system and  $\omega$  is the angular frequency. So Equation 3.29 is transformed to

$\mathbf{P}(t) = \varepsilon_0(\varepsilon^*(\omega) - 1)\mathbf{E}(t)$	(3.30)
---	--------

where  $\varepsilon^*(\omega)$  is the complex dielectric function. Thus the real part  $\varepsilon'(\omega)$  is proportional to the energy stored reversibly in the system per period and the imaginary part  $\varepsilon''(\omega)$  is proportional to the energy which is dissipated per period. The relationship between frequency domain form and time domain form of the dielectric function is given by

$\varepsilon^*(\omega) = \varepsilon'(\omega) - i\varepsilon''(\omega) = \varepsilon_\infty - \int_0^\infty \frac{d\varepsilon(t)}{dt} \exp(-i\omega t) dt$	(3.31)
---	--------

Equation 3.31 is a one-sided Fourier or full imaginary Laplace transformation<sup>139</sup>. And the real part  $\varepsilon'(\omega)$  are related to the imaginary part  $\varepsilon''(\omega)$  by Kramers/Kronig relations<sup>69, 140</sup>.

$$\varepsilon'(\omega) - \varepsilon_\infty = H[\varepsilon''(\omega)] = \frac{1}{\pi} \oint \frac{\varepsilon''(\xi)}{\xi - \omega} d\xi \quad (3.32)$$

The function  $H[ ]$  denotes the Hilbert transformation. This means from experimental point of view  $\varepsilon'(\omega)$  and  $\varepsilon''(\omega)$  carry the same information. Furthermore the dielectric strength  $\Delta\varepsilon$  can be derived by intergrating the imaginary part

$$\varepsilon_s - \varepsilon_\infty = \Delta\varepsilon = \frac{2}{\pi} \int_0^\infty \varepsilon''(\omega) d \ln \omega \quad (3.33)$$

For  $\varepsilon(t)$  and  $\varepsilon^*(\omega)$  are generalized compliances, there is a corresponding modulus called electric modulus  $M(t)$  in the time domain and  $M^*(\omega)$  in the frequency domain. The relationship between the compliance and the modulus is

$$\int_{-\infty}^\infty M(t - \tau) \varepsilon(\tau) d\tau = -\delta(t) \text{ and} \\ M^*(\omega) \varepsilon^*(\omega) = 1 \quad (3.34)$$

where  $\delta(t)$  is the Dirac function.

### 3.3.2 Analysis of dielectric spectra

In the simplest case, the change of orientational polarization can be calculated by its actual value:

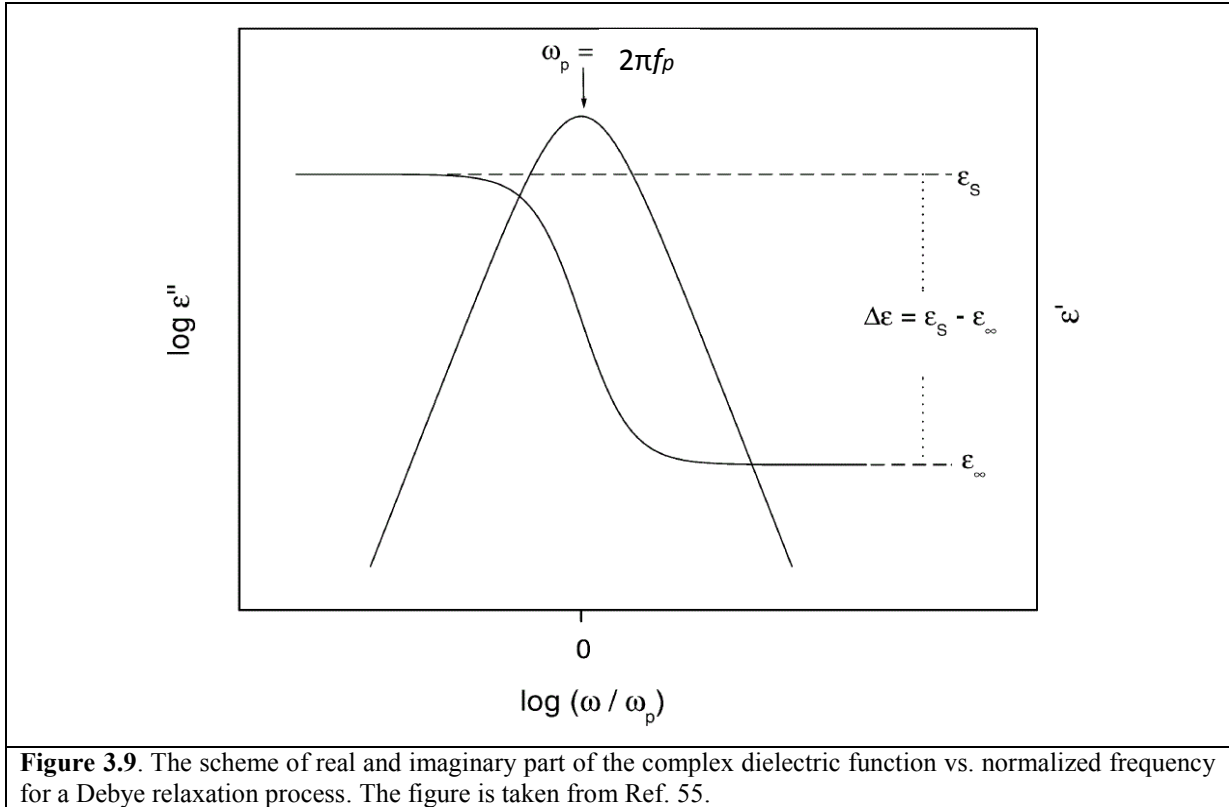
$$\frac{P(t)}{dt} = -\frac{1}{\tau_D} P(t) \quad (3.35)$$

where  $\tau_D$  is a characteristic relaxation time. This function leads to an exponential decay for the correlation function  $\Phi(\tau) = \exp\left[-\frac{t}{\tau_D}\right]$ . These relations can be used to derive the Debye relaxation function

$$\varepsilon^*(\omega) = \varepsilon_\infty + \frac{\Delta\varepsilon}{1 + i\omega\tau_D} \quad (3.36)$$

With Debye relaxation function the relaxation processes due to rotational fluctuations of molecular dipoles can be described. Normally they are related to the characteristic molecular structure (functional groups etc.) or to the whole molecules. If the frequency  $f = \omega/2\pi$  of the applied outer electrical field is in agreement with the reorientation time  $\tau$

of molecular dipoles the value of imaginary part  $\varepsilon''(\omega)$  will be the maximal point. The Figure 3.9 gives the typical dielectric pattern with increasing  $\omega$  the real part  $\varepsilon'(\omega)$  decreases like a step whereas the imaginary part  $\varepsilon''(\omega)$  displays a extrema. The frequency of the maximal loss  $f_p$  is related



to the mean relaxation time  $\tau_p = 1/2\pi f_p$  of the fluctuation dipoles.

From the shape of the loss peak the distribution of relaxation times can be deduced. From either the step in  $\varepsilon'(\omega)$  or the area under the loss peak of  $\varepsilon''(\omega)$  the dielectric strength  $\Delta\varepsilon$  can be determined. Because the fact mentioned they are interrelated with each other by the Kramers/Kronig relations.

In many real cases the half width of measured loss peaks is broader than predicted by Debye model and the pattern shape is asymmetric with a high frequency tail. This is called non-Debye relaxation behavior. There are several empirical model functions modified based on the Debye function which have been developed to describe the broadened and asymmetric loss peaks. The Cole/Cole-function<sup>141</sup> describes a broadening case

$\varepsilon_{CC}^*(\omega) = \varepsilon_{\infty} + \frac{\Delta\varepsilon}{1 + (i\omega\tau_{CC})^{\beta}}$	(3.37)
--	--------

where  $0 < \beta \leq 1$  which gives a symmetrical broadening for the relaxation function. When  $\beta = 1$  the Debye-function is obtained. The Cole/Cole-relaxation time  $\tau_{CC}$  can be derived by  $\omega_{CC} = 1/\tau_{CC}$ .

The relaxation behaviors in liquids or low molecular glass-forming materials show a more complex asymmetric broadening dielectric function which can be described by the Cole/Davidson-function<sup>142, 143</sup>

$\varepsilon_{CD}^*(\omega) = \varepsilon_{\infty} + \frac{\Delta\varepsilon}{(1 + i\omega\tau_{CD})^{\gamma}}$	(3.38)
---	--------

where  $0 < \gamma \leq 1$  describes an asymmetric broadening of the relaxation function for frequencies  $\omega > 1/\tau_{CD}$  where  $\tau_{CD}$  is the Cole/Davidson relaxation time. For  $\gamma = 1$  the Debye-function is obtained again.

Havriliak and Negami introduce a more general model function<sup>144, 145</sup> (HN-function) which is a combination of the Cole/Cole and Cole/Davidson-function:

$\varepsilon_{HN}^*(\omega) = \varepsilon_{\infty} + \frac{\Delta\varepsilon}{(1 + (i\omega\tau_{HN})^{\beta})^{\gamma}}$	(3.39)
---	--------

The shape parameters  $\beta$  and  $\gamma$  describe the symmetric and asymmetric broadening of the complex dielectric function with  $0 < \beta, \beta\gamma \leq 1$ . Figure 3.10 gives the examples of the HN-function with selected shape parameters.

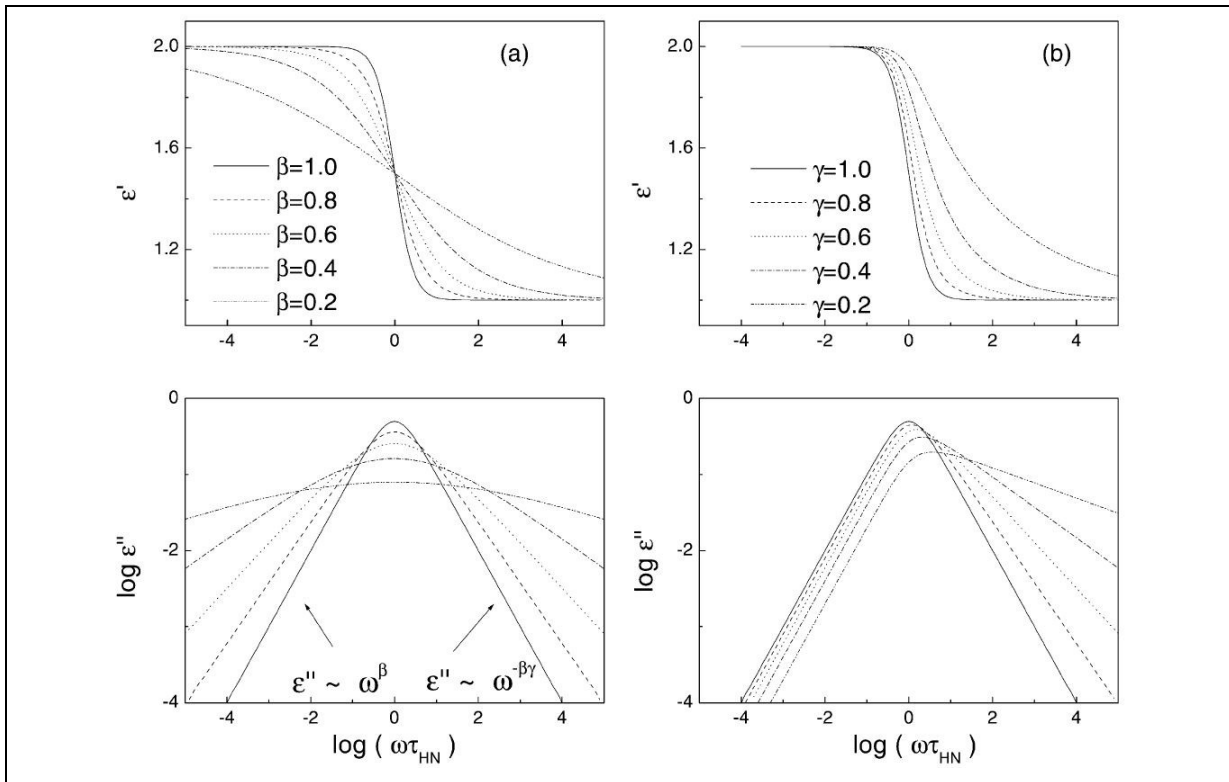


**Figure 3.10.** The scheme of variations of real and imaginary part of complex dielectric permittivity for the Havriliak/Negami-function with fixed (a)  $\gamma=1$ ; (b)  $\beta=1$  ( $\tau_{HN}=1$  s,  $\Delta\epsilon=1$ ,  $\epsilon_\infty=1$ ). The figure is taken from Ref. 55.

Figure 3.11 gives the dielectric loss of poly(chloro styrene) for the  $\alpha$ -relaxation at 428.6 K. The different models Cole/Davidson-, Cole/Cole- and HN-function are fitted to the data. Only

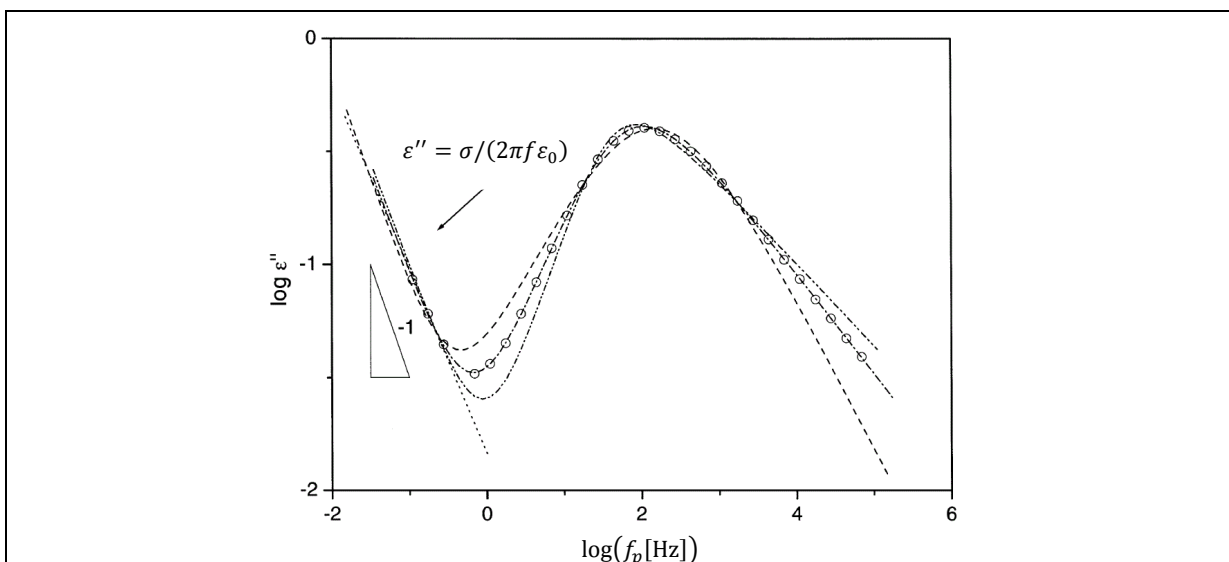


**Figure 3.11.** Dielectric loss versus frequency for poly(chloro styrene) at  $T=428.6$  K. The slope at lower frequency is the conductivity contribution. The relaxation part is described by three different models: *dashed* Cole/Cole-function, *dotted-dotted-dashed* Cole/Davidson-function, *dotted-dashed* HN-function. The figure is taken from Ref. 55.

the fit of HN-function covers all range of frequency. From this aspect for an isolated relaxaton process a set of four parameters is necessary to describe completely.

According to linear response theory the dielectric function has a corresponding complex electric modulus  $M^*(\omega)$

$M^*(\omega) = M'(\omega) + iM''(\omega)$	(3.40)
---	--------

The corresponding modulus is given below if  $\varepsilon^*(\omega)$  is described by the Debye-function.

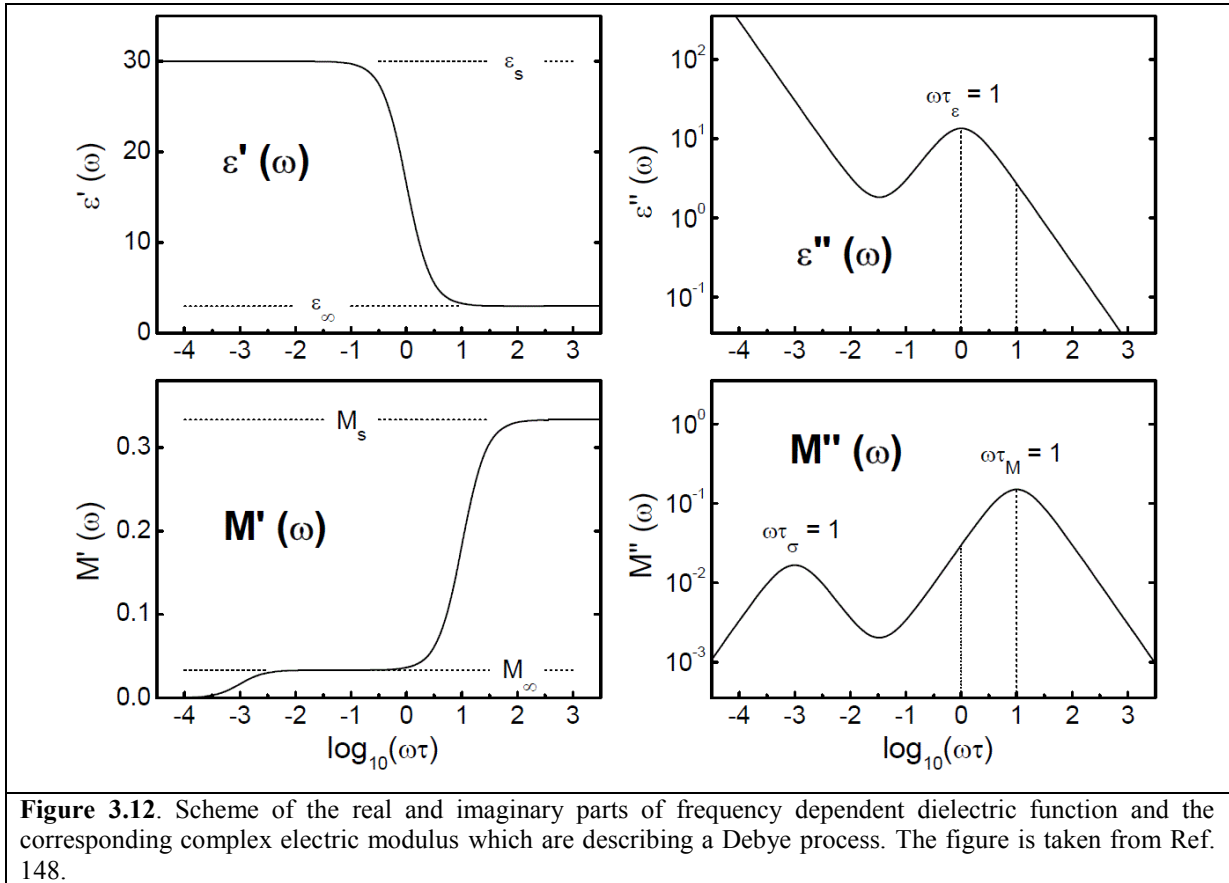
$M^*(\omega) = M_\infty + \frac{\Delta M}{1 + i\omega\tau_{D-M}}$	(3.41)
---	--------

where  $\Delta M = M_S - M_\infty$ ,  $M_S = 1/\varepsilon_S$  and  $M_\infty = 1/\varepsilon_\infty$ . This means the corresponding modulus is Debye-like as well. The electric relaxation time  $\tau_{D-M} = (\varepsilon_\infty/\varepsilon_S)\tau_D$  is given, apparently  $\varepsilon_\infty < \varepsilon_S$  so  $\tau_{D-M} < \tau_D$  holds. For the same relaxation process the representation in the modulus pattern has a higher relaxation rate than the one in the dielectric function pattern. Figure 3.12 depicts a Debye relaxation process represented by both the dielectric function and the electric modulus. It is worth noting that the dielectric properties for a electronic conduction can also be expressed in the modulus representation. Like in the imaginary part

$M''(\omega) = M_\infty \frac{\omega\tau_{\text{Cond}}}{1 + (\omega\tau_{\text{Cond}})^2}$	(3.42)
--	--------

is obtained. For the peak of maximal loss gives  $\omega_M\tau_{\text{Cond}} = 1$  with  $\tau_{\text{Cond}} = \varepsilon_0\varepsilon_\infty/\sigma_0$ . And in the corresponding real part  $M'(\omega)$  increases from zero to  $M_\infty = 1/\varepsilon_\infty$ .

In some cases, the charge carriers are blocked at inner dielectric boundary layers (Maxwell/Wagner/Sillars polarization<sup>146, 147</sup>) on the mesoscopic scale or at the external electrodes contacting the sample (electrode polarization) on the macroscopic scale. Both of



them give rise to a separation of charges which will contribute to the polarization, and the resulting dielectric loss can be by orders of magnitude larger than the dielectric responses from molecular fluctuation. The Maxwell/Wagner/Sillars polarization is observed in inhomogeneous systems such as suspensions or colloids<sup>149</sup>, biological materials<sup>150</sup>, phase separated polymers, blends, crystalline or liquid crystalline polymers. The mesoscopic origin of the effect can be due to a nanophase separated structure, at the internal phase boundaries charges are blocked and causes a strong increase in  $\epsilon'(\omega)$  with decreasing frequency. The electrode polarization can mask the dielectric response of the sample. Recently, Samet *et al.*<sup>151</sup> give an approach to discriminate the difference between Maxwell/Wagner/Sillars and electrode polarizations by analyzing the inter-relation governing their characteristic frequencies. However, validity of the approach has to be checked in different systems furtherly.

## Chapter 4 Experimental section

### 4.1 Materials

#### 4.1.1 Organic modified Layered double hydroxides

The organomodified MgAl/LDH (O-MgAl/LDH; O-LDH) was synthesized by a one-step procedure<sup>152</sup>. Firstly, magnesium and aluminum metal salt solution ( $\text{Mg}^{2+}:\text{Al}^{3+}$  ratio equal to 2:1; the whole metal ion concentration was kept at 0.3 M) was dropped in a SDBS solution under continuous stirring at 50 °C. The pH value of the solution is stabilized at  $10 \pm 0.2$  by dropping the needed amount of 1 M NaOH in. The slurry solution was continuously stirred for 0.5 h, heated up to 75 °C and kept at this temperature for 18 h. The final product was filtered and washed with distilled water several times until the pH of the obtained liquid was about 7. Then the organomodified MgAl/LDH was dried in an oven at 80 °C until the weight was constant. The unmodified MgAl/LDH (U-MgAl/LDH; U-LDH) was also synthesized for comparison by a similar procedure. Although the LDH materials were dried in vacuum before mixing with the polymer matrix, some bound water might be still present in the interlayers of the LDH.

For the O-NiAl-LDH the same procedure is applied, except substituting magnesium component by nickel. Also the unmodified NiAl-LDH (U-NiAl-LDH) was synthesized for comparison.

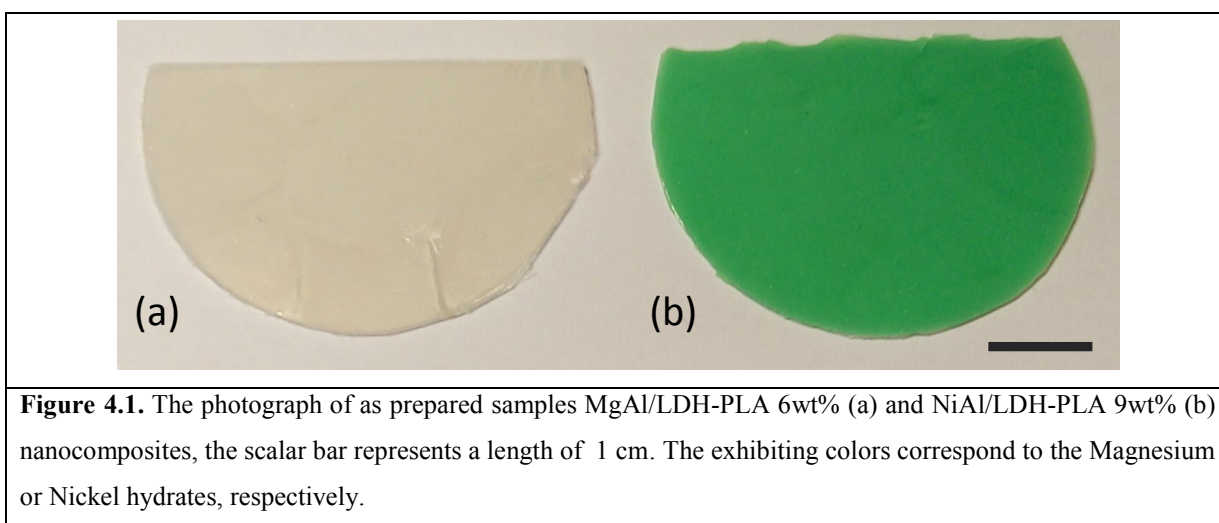
#### 4.1.2 Poly(L-lactide)

Poly(lactide) was purchased as Biomer<sup>®</sup> L9000 from Biomer (Krailling, Germany). It is a predominantly L-type poly(lactide) and was used without further purification. The melt flow index was 3.0-6.0 g/10min. In a differential scanning calorimetry (DSC) measurement at 10 K/min scan rate, the observed glass transition temperature  $T_g$  is 57.5 °C, cold crystallization temperature  $T_c$  is 131.0 °C, melting temperature  $T_m$  is 167.2 °C, cold crystallization enthalpy is 6.76 J/g and melting enthalpy is 8.18 J/g.

### 4.2 Preparation of nanocomposites

The nanocomposites were prepared by melt mixing in a one step process. Before compounding, all the materials (polymer, LDH) were dried under vacuum at 323 K for 24 h. PLA contains a polar group in the main chain which can interact with the LDH for intercalation. Therefore no compatibilizer is needed like for corresponding polyolefin

based nanocomposites<sup>153, 154</sup>. The LDH was mixed in different concentrations with pure PLA to obtain the various nanocomposites. Melt mixing was carried out in a co-rotating twin-screw microextruder (15-mL microcompounder, DSM Xplore, Geleen, The Netherlands) at 463 K with 200 rpm screw speed for 10 min. The concentrations of O-LDH in the nanocomposites were determined based on an approximate metal hydroxide content of the filler. The extruded samples were melt pressed (above the melting temperature) to platelets (40 mm \*40 mm) and thickness of ca. 0.4 mm for several minutes. After that the samples were slowly cooled down in the press (as prepared samples).



## 4.3 Experimental techniques

### 4.3.1 X-ray scattering

The X-ray scattering investigations were carried out in two places because of the long waiting time for the experiments. The characterization of MgAl/LDH-PLA nanocomposites was made at the synchrotron micro focus beamline  $\mu$ Spot (BESSY II of the Helmholtz Centre Berlin for Materials and Energy). A more detailed description of the beamline can be found elsewhere<sup>155</sup>. The beamline provides a beam with a diameter of 100  $\mu$ m at a photon flux of  $1 \times 10^9 \text{ s}^{-1}$  at a ring current of 100 mA. The divergence is less than 1 mrad (horizontally and vertically). The experiments were carried out employing a wavelength of 1.03358  $\text{\AA}$  using a double crystal monochromator (Si 111). The data were collected by a two-dimensional X-ray detector (MarMosaic, CCD  $3072 \times 3072$  pixel with a point spread function width of about 100  $\mu$ m) 820 mm behind the sample position. The obtained scattering images were converted into diagrams of scattered intensities versus scattering vector  $q$  ( $q$  is defined in terms of the scattering angle  $\theta$  and the wavelength  $\lambda$  of

the radiation, thus  $q = 4\pi/(\lambda \sin\theta)$  employing an algorithm of the computer program FIT2D<sup>156</sup>.

X-ray measurements of NiAl/LDH-PLA nanocomposites were performed in a sample holder for solid-state samples with a SAXSpace instrument (Anton Paar, Austria) in line geometry at a temperature of  $298 \pm 1$  K. Each sample was measured for 360 s (60 measurements of 6 s each). The measured intensity was corrected by subtracting the intensity of the empty sample holder. The wavelength  $\lambda$  of the radiation is 0.154 nm. Deconvolution (slit length desmearing) of the SAXS curves was performed with the SAXS-Quant software (Anton Paar, Austria).

#### 4.3.2 Size Exclusion Chromatography (SEC)

SEC was carried out using a refractive index detector ERC 7510 and the following columns: “1 x PL gel mixed C, 10  $\mu\text{m}$ , 300 x 8 mm” and “1 x PSS gel 1000 Å, 3 $\mu\text{m}$ , 300 x 8 mm”. As eluent Chloroform was used at a flow rate of 1.0 mL/min and a temperature of 25°C. The samples were prepared by dissolving 9 to 16 mg of the sample in 1 mL Chloroform. 100  $\mu\text{L}$  of the filtered solution (0.2  $\mu\text{m}$  millipore filter) was injected. Calibration was performed by polystyrene standards (PSS Mainz).

#### 4.3.3 Thermal analysis

The thermal experiments have to be separated into two parts. One is the normal measurements for glass transition temperature and melting enthalpy which was carried out by differential scanning calorimeter (DSC, Seiko instruments, DSC 220C). The samples (ca. 10 mg) were characterized from 248 K to 523 K with a heating and cooling rate of 10 K/min using nitrogen as protection gas. For the pure polylactide, the cold crystallization and melting temperatures are 403 K and 440 K, whereas the corresponding enthalpies are 6 J/g and 8 J/g respectively. A glass transition temperature of 333 K and  $\Delta c_p$  of 0.51 J/g\*K was also estimated from the thermogram.

For the further analysis of phase fractions of the polymer nanocomposites, the thermal data were measured by a PerkinElmer PYRIS Diamond DSC. The sample mass was about 10 mg. The instrument was calibrated as recommended by GEFTA<sup>157</sup> by indium and zinc at zero heating rate for temperature and by sapphire for heat capacity.

For determining the different phase fractions a special temperature program is designed. Two different sets of experiments were carried out. In the first set of experiments, the

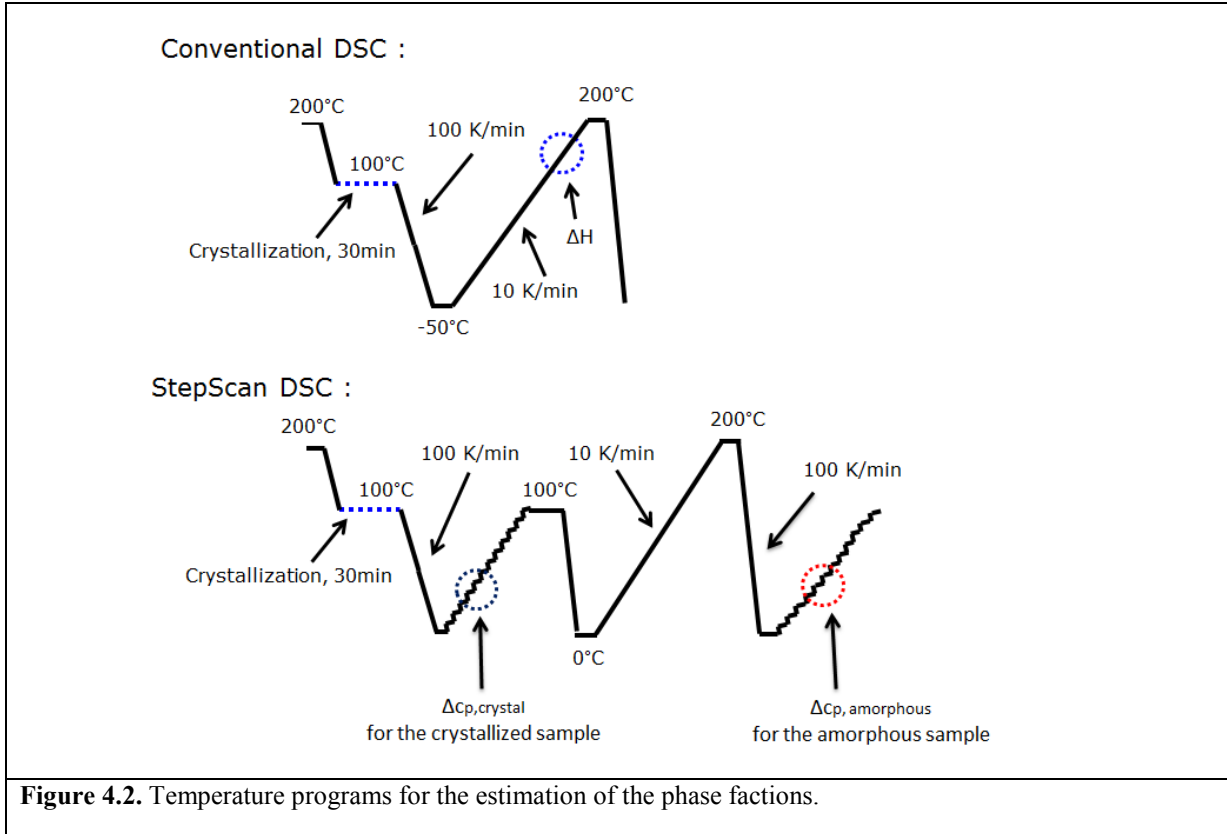
samples were heated to 200 °C to erase the thermal history. After this treatment the sample was cooled down with a rate which varied in the range from 2 K/min to 300 K/min. In contrast to the most semicrystalline polymers, polylactide has a relative long crystallization half time<sup>158, 159, 160</sup>. Therefore, it is possible to estimate a critical cooling rate at which the crystallization and the RAF caused by crystallization can be suppressed for the LDH-PLA nanocomposites with different concentrations of the nanofillers. After the cooling process, the enthalpies for cold crystallization and melting were measured during a subsequent heating run from 0 °C to 200 °C at a rate of 10 K/min. These experiments result in a critical cooling rate  $\beta_{crys}$  of 25 K/min (see below) for the crystallization of PLA.

In the second set of experiments both the melting enthalpy  $\Delta H$  and the increment of the specific heat capacity at the glass transition  $\Delta c_p$  was determined precisely for all samples which were crystallized under well-defined conditions by conventional and StepScan calorimetry (SSDSC), respectively for each concentration of the nanofiller.

**Conventional calorimetry:** In the first part of the experiment the sample was heated to 200 °C and kept there for 2 min to melt it completely and to erase the thermal history. Then the sample was cooled to  $T_{crys}=100$  °C with a rate of 100 K/min to avoid any crystallization. At this temperature the sample was isothermally crystallized for 30 min under defined conditions from the melt. Afterwards, the sample was cooled to -50 °C with a programmed rate of 100 K/min. This procedure leads to a sample with a well-defined crystallinity. Then the sample was heated with a rate of 10 K/min. No cold crystallization was detected during this heating run yielding to the conclusion that the isothermal crystallization at 100 °C for 30 min leads to a fully crystallized samples. The melting enthalpy  $\Delta H$  was estimated for the given concentration of the nanofiller.

**StepScan calorimetry:** SSDSC a special variant of temperature modulated DSC and was carried out by employing 1 K steps at heating rate 12 K/min and isotherms of about 1.5 min. For these measurements the samples were again crystallized under defined conditions as described above (see also Figure 4.2) and cooled down to 0 °C with 100 K/min and kept there for 7 min for equilibration. Then the StepScan experiment was carried out from 0 °C to 100 °C under the conditions given above. These measurements allow a precise estimation of the increment of the specific heat capacity at the glass transition for the crystallized sample  $\Delta c_p$  for a given concentration of the nanofiller. After this step of the experiment, the sample was again cooled down to 0 °C for experimental

reasons and heated up with 10 K/min to 200 °C and kept there for 2 min to melt it completely and erase the thermal history again. After this procedure the sample was cooled down with programmed cooling rate of 100 K/min to 0 °C to avoid any crystallization. After a waiting time of 7 min SSDSC measurement was carried out from 0 °C to 100 °C to estimate the increment of the specific



heat capacity at the glass transition for the amorphous sample  $\Delta C_{p,amorphous}$  for the same concentration of the nanofiller.

#### 4.3.4 Broadband dielectric spectroscopy (BDS)

A high-resolution ALPHA analyzer together with an active sample holder head (Novocontrol, Montabaur, Germany) is used, to measure the complex dielectric function  $\epsilon^*(f) = \epsilon'(f) - i\epsilon''(f)$  ( $\epsilon'$ -real part,  $\epsilon''$ -loss part and  $i = \sqrt{-1}$ ) as function of frequency  $f$  ( $10^{-1}$  Hz to  $10^6$  Hz) and temperature  $T$  (160 K to 400 K). Samples were prepared in parallel plate geometry. Therefore, gold electrodes with a diameter of 20 mm were evaporated on both sides of the samples. The samples were mounted between two gold-plated electrodes (20 mm) of the sample holder. Isothermal frequency scans were carried out where the temperature is controlled by a Quatro Novocontrol cryo-system with a temperature stability of 0.1 K. Details can be found elsewhere<sup>161</sup>.



## Chapter 5 Investigation of nanocomposites based on polylactide and MgAl/LDH

### 5.1 The SAXS analysis for the modified LDH and the dispersion of the nanofiller within the nanocomposites

In the first step the successful modification of LDH by SDBS was proven by SAXS measurements. Figure 5.1 compares the SAXS pattern for O-MgAl/LDH and U-MgAl/LDH. The SAXS data for unmodified LDH shows two equidistant reflections at  $7.1 \text{ nm}^{-1}$  and  $14.11 \text{ nm}^{-1}$ . This is characteristic for a layered compound corresponding to a lamellar repeat distance ( $d = 2\pi/q_{peak}$ ) of  $d = 0.88 \text{ nm}$ . Subtracting the thickness of the hydroxide brucite-like LDH of  $0.49 \text{ nm}$ <sup>162</sup> this results in an effective interlayer distance to be  $0.39 \text{ nm}$ . By fitting two Gaussians to the data, the peak widths were determined to  $w = 0.69 \text{ nm}^{-1}$ . From the width a mean correlation length perpendicular to the lamella normal can be calculated to  $l_c = 2\pi/w = 9.23 \text{ nm}$ . Assuming that lattice distortions can be neglected in a first approximation the crystallite thickness in the direction normal to the (001) plane can be estimated. This calculation results that the average number of layers in a stack of the unmodified LDH is approximately 10.

As expected, the lamellar reflections for modified LDH shift to lower  $q$ -values. Four equidistant reflections are visible. The lack of reflections in the diagram of O-LDH at a  $q$  value of  $7.1 \text{ nm}^{-1}$  proves the absence of significant amounts of U-MgAl/LDH. A similar analysis as discussed above can be also carried for O-MgAl/LDH. After the subtraction of the thickness of the brucite sheet the effective layer distance is  $2.54 \text{ nm}$ . As expected the introduction of the SDBS provokes an essential widening of the distance between the layers. The width of the peak for the O-MgAl/LDH is estimated to  $0.36 \text{ nm}^{-1}$ . This is essentially smaller than for U-MgAl/LDH. Therefore the number of layers in a stack of the modified LDH is lower than for U-MgAl/LDH and is calculated to ca. 6. On the one side, likely the SDBS hinders the formation of large stacks and reduces the number of layers in O-MgAl/LDH. On the other side, the existence of small stacks with only few layers will lead to nanocomposites.

---

\*Similar content was presented in: J. Leng; P. J. Purohit; N.-J. Kang; D.-Y. Wang\*; J. Falkenhagen; F. Emmerling; A. F. Thünemann; A. Schönhals\*, *Eur. Polym. J.* **2015**, *68*, 338-354.

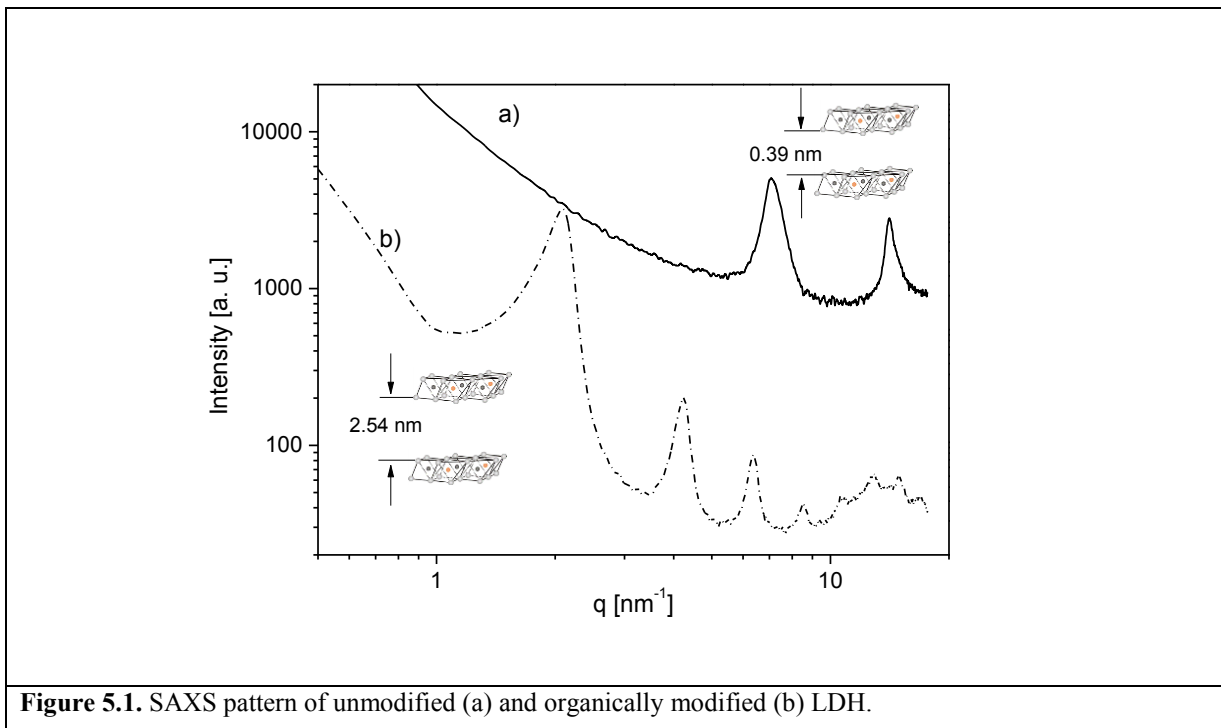
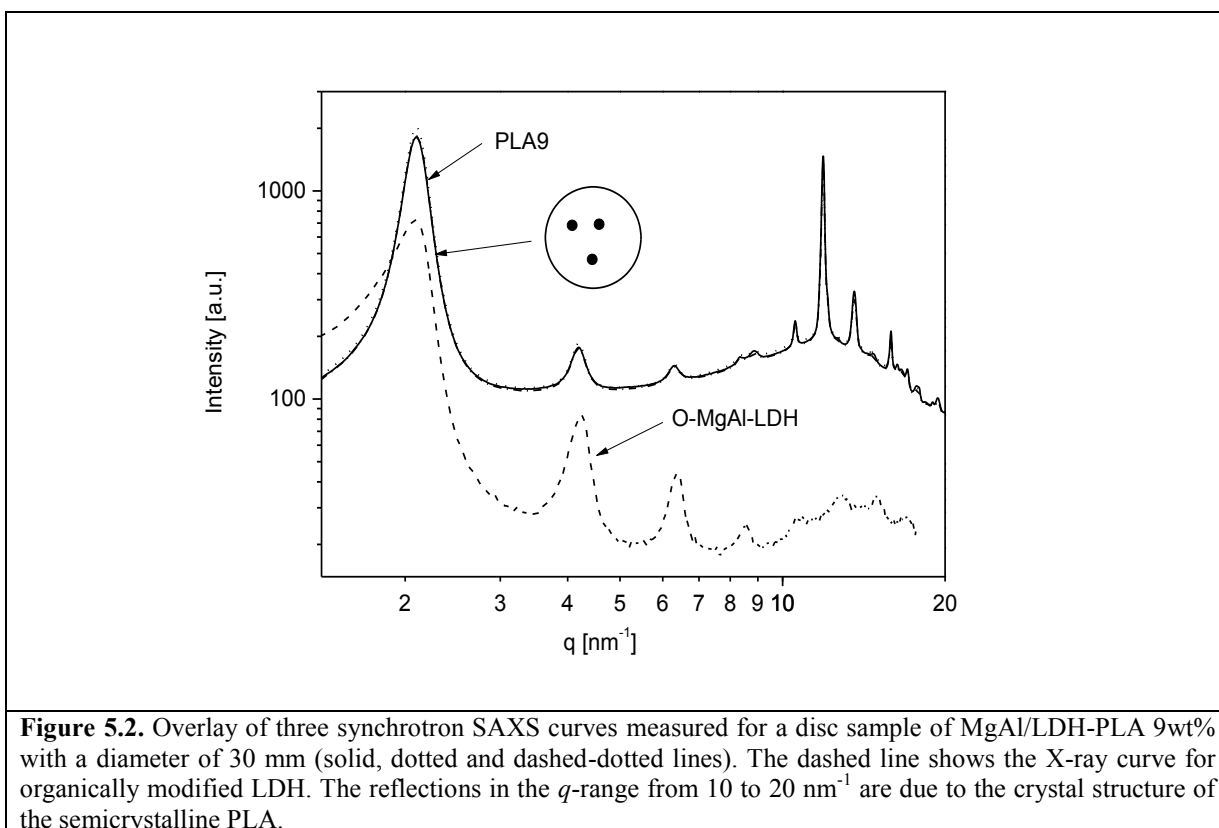


**Figure 5.1.** SAXS pattern of unmodified (a) and organically modified (b) LDH.

The homogenous, spatial distribution of the nanofiller across the sample on a macroscopic scale is one of the key parameters which determine the structure property relationships of nanocomposites. To study this in more detail space resolved X-ray experiments were employed with a microfocus using synchrotron radiation at the  $\mu$ SpotBeamline of BESSY<sup>153</sup>. The measurements were carried out at three different positions of the as prepared samples having a diameter of more than 30 mm where the spot diameter of the X-ray beam was 0.1 mm. The result is depicted in Figure 5.2 for MgAl/LDH-PLA 9 wt% as one example. All the individual SAXS pattern nearly collapse into one chart (solid, dotted and dashed-dotted curves, positions of measurements at the sample are shown in the inset). This proves a homogeneous dispersion of O-LDH in the polymer matrix on macroscopic length scales (> 1 mm).

Figure 5.1 gives further that in the SAXS region reflections at quite similar positions are observed for O-MgAl/LDH and for the nanocomposite. The reflections are a bit weaker and also broader this evidences that stack-like structure similar to that O-MgAl/LDH are also present in the nanocomposites. This result points to a partly exfoliated morphology with mixed nanostacks. After fitting Gaussians, the lamellar repeat unit  $d$  was found out no much difference with O-LDH. This result is similar to results obtained for previously studied nanocomposites based on polyolefines. The stack size was determined from the widths of the peaks and the  $l_c$  was calculated to be 25.6 nm which is equivalent to around

6 layers like for O-MgAl/LDH. Because of the fact that the stacks are so small even a homogenous mixing of these nanostacks in the polymer matrix will lead to nanocomposites.



## 5.2 SEC analysis for the degradation stability of the nanocomposites

The LDH materials contain Al and Mg ions which may cause a catalytic degradation of the PLA matrix. For a similar system an enhanced thermal degradation behavior is reported<sup>163</sup>. Therefore, here Size Exclusion Chromatography was employed to study the quasi isothermal degradation. The investigations were carried out for samples which were stored for more than 3 years at room temperature. Figure 5.3 gives the elugram for neat PLA. Two elution regions having different intensities can be identified. The first one at shorter elution times corresponds to high molecular weights where the second one is due to lower molecular weights. The inset of Figure 5.3 gives the molecular weight distribution for the high molecular weight elution peak for the different LDH concentrations. With increasing concentration of LDH the peak maximum shifts slightly to lower molecular weight. This means with increasing concentration of LDH the molecular weight of the matrix decreases slightly due to catalytic degradation.

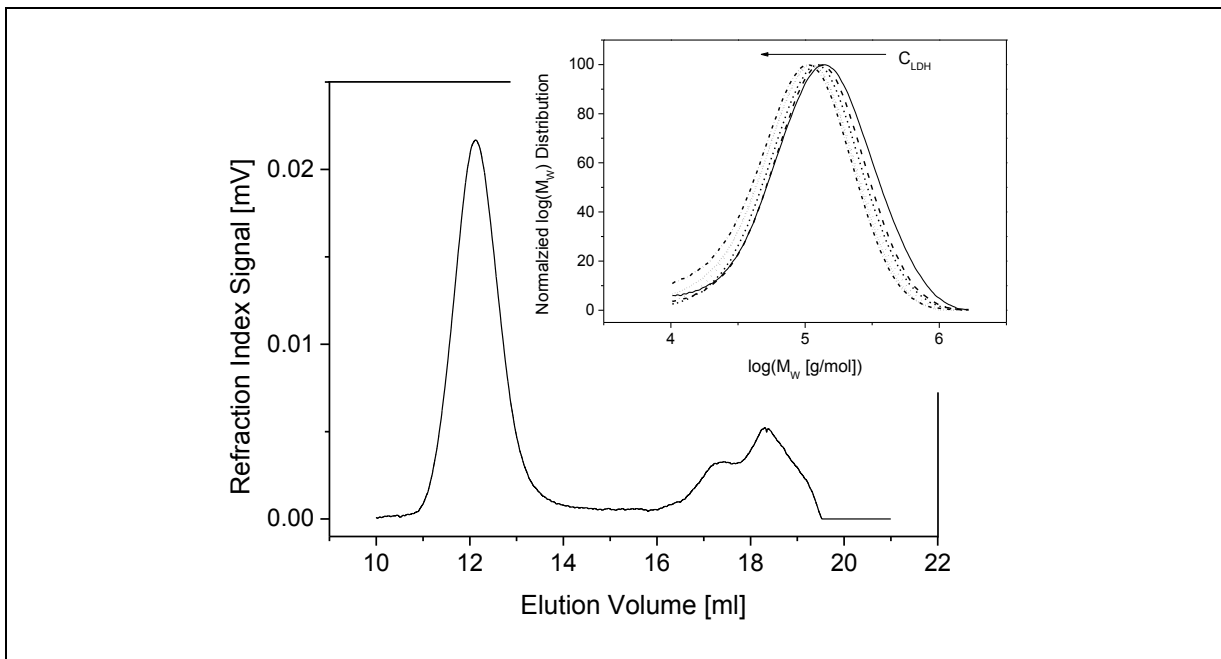


**Figure 5.3.** Signal of the refractive index detector versus the elution volume for pure PLA. The inset shows the normalized molecular weight distribution versus the molecular weight: solid line – pure PLA, dashed line – MgAl-1 wt%, dotted line – MgAl-3 wt%, short dash line – MgAl-6 wt%, short dotted line – MgAl-9 wt%, short dashed dotted line – MgAl-12 wt%.

This becomes clearer in Figure 5.4 where weight averaged molecular weight  $M_W$  is plotted versus  $C_{LDH}$ . With increasing concentration of LDH  $M_W$  decreases from about 190 kg/mol to about 130 kg/mol. This evidences that the nanoparticles influences slightly the degradation of the polymeric matrix likely by catalytic processes. Besides the catalytic activity also the remaining water in the intergalleries might contribute to the degradation process. The change of the molecular weight is small. This slightly decreased molecular weight will not have a significant effect on the properties studied during the course of this paper.

The inset of Figure 5.4 gives the molecular weight distribution of the molecular weight for the release at longer elution times. Obviously, the distribution is bimodal indicating two different molecular species. To compare the different samples, the distribution was normalized by the maximum value of the peak at lower molecular weights. Probably, this low molecular weight compounds are degradations products. These degradation products are also found for neat PLA. But nevertheless the relative amount of both degradation species changes with increasing concentration of LDH. It was tried to identify the both degradation products on a molecular level by mass spectrometry. But up to now only a limited success was made. Therefore, further experimental work is necessary to investigate this problem in more detail.

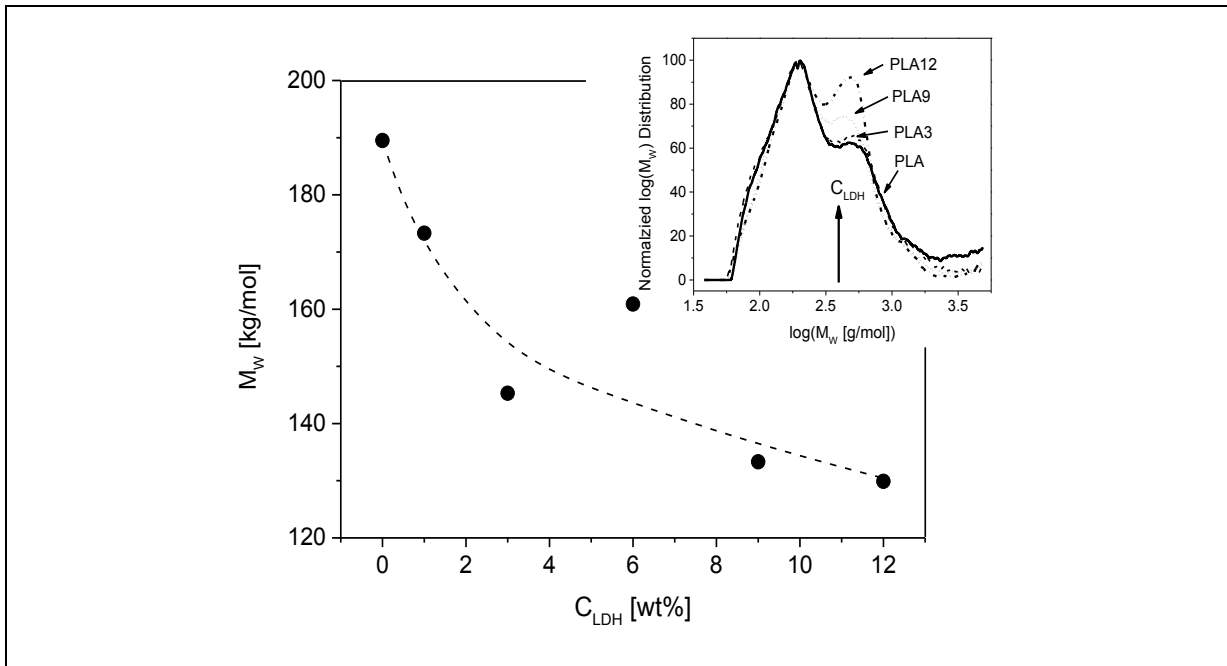


**Figure 5.4.** Change of the weight averaged molecular weight  $M_w$  with the concentration of LDH. The inset shows the normalized molecular weight distribution versus the molecular weight for the low molecular weight degradation products: solid line – pure PLA, dotted line – MgAl-3 wt%, short dotted line – MgAl-9 wt%, short dashed dotted line – MgAl-12 wt%. In the inset the other concentrations are omitted for sake of clearness.

### 5.3 Crystallinity of the nanocomposites investigated by DSC and WAXS

Figure 5.5 compares the DSC curves of the as prepared samples (first heating) run for pure PLA, MgAl-1 wt% and MgAl-12 wt%. All measurements discussed here were carried at heating rate of 10 K/min. A glass transition region as well as crystallization and melting is observed for each concentration of the nanofiller. The glass transition temperature does not change significantly with the concentration of the nanofiller. This concerns also the width of the glass transition.

Interestingly, compared to the pure PLA the melting enthalpy of MgAl-1 wt% is much larger. Moreover, a pronounced cold crystallization peak is observed for MgAl-1 wt%. This suggests that the LDH acts as a nucleation agent. A similar effect was also discussed in the literature. For instance Pilla et al. showed that the addition of recycled wood fibers leads to an increase of the crystallinity of PLA<sup>164</sup>. This will be discussed in more detail below.

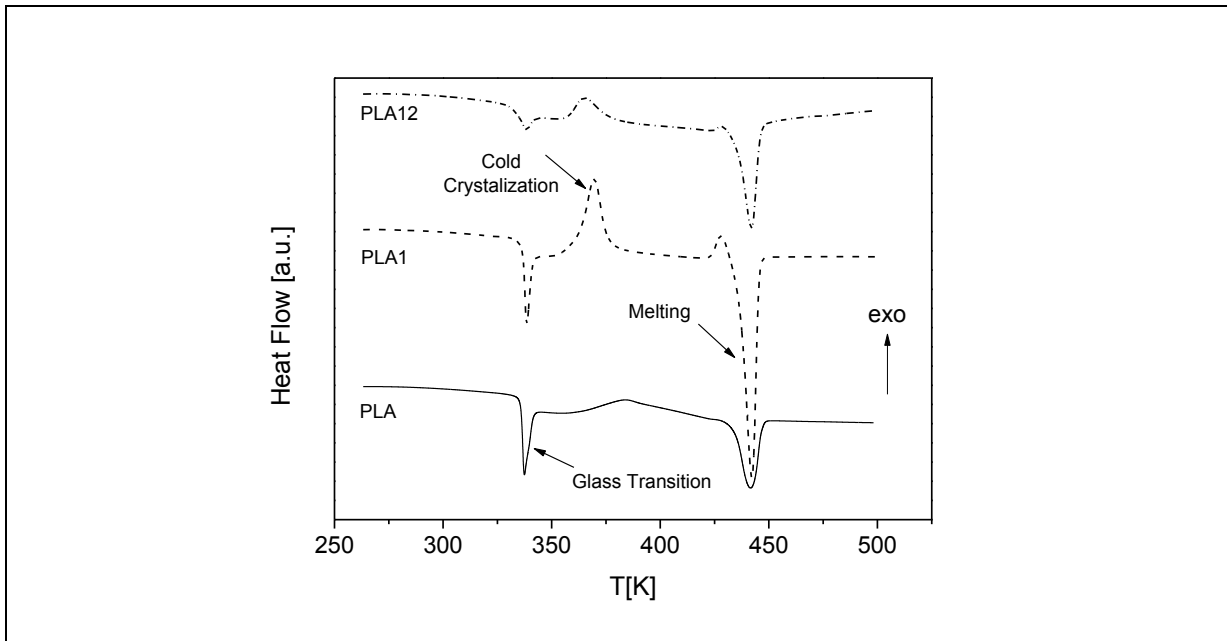
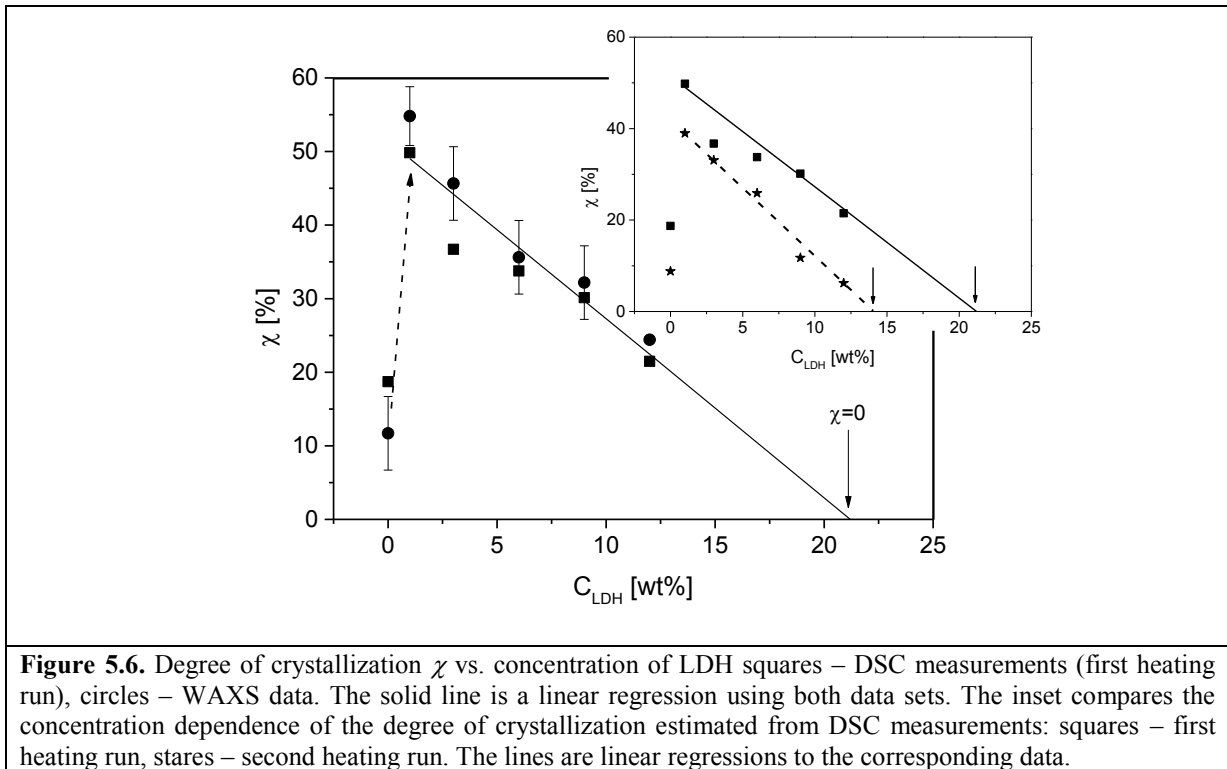


**Figure 5.5.** Comparison of DSC thermograms (*as prepared samples*, first heating, heating rate of 10 K/min) for pure PLA and selected nanocomposites: solid line - pure PLA, dashed line - MgAl-1 wt%, dashed dotted line - MgAl-12 wt%. The curves are shifted along the y-scale for sake of clearness.

Table 5.1 shows that for concentrations higher than 1 wt% the melting enthalpies (first heating) decrease with increasing concentration of LDH because the amount of polymer decreases with increasing content of LDH. From the melting enthalpy  $\Delta H_m$  the degree of crystallization can be calculated. In a first step, the enthalpy values have to be normalized to the amount of polymer. The degree of crystallization is given  $\chi = (1 - C_{LDH}) \Delta H_m / \Delta H_{m,100\%} * 100$  where  $\Delta H_{m,100\%}$  is the melting enthalpy of a complete crystalline PLA sample. The value of  $\Delta H_{m,100\%} = 93$  J/g is taken from references<sup>168, 165</sup>. In Figure 5.6,  $\chi$  increases for  $C_{LDH} = 1$  wt% compared to the bulk value. This means for a small amount of LDH the degree of crystallinity increases. This gives further evidence that the nanofiller acts as a nucleating agent and the crystallinity of the nanocomposites increases for low concentrations of LDH compared to the pure PLA. For higher values of  $C_{LDH}$  the degree of crystallization decreases approximately linearly with increasing concentration of LDH.

The extrapolation of  $\chi$  to zero value results in a critical concentration of LDH  $C_{Ci}$  of ca. 21 wt%. From the DSC measurements (first heating run) it is therefore concluded that for concentrations higher than this value, the cold crystallization of PLA is completely suppressed at 21 wt% LDH for the as prepared samples. This behavior is similar to that observed for nanocomposites based on olefins and LDH.

Absolute values of the crystallinity  $\chi$  can be also calculated with the wide angle X-ray scattering pattern (WAXS). For that analysis the  $q$  range from  $1.5 \text{ nm}^{-1}$  to  $40 \text{ nm}^{-1}$  is chosen and 60 counts were subtracted from the spectra as detector background. Moreover, the Kratky representation is used because  $q^2 I(q)$  is approximately proportional to the real number of scattered photons and more importantly to have equal condition in the whole  $q$  range. The integral  $A_{total} = \int_{1.5 \text{ nm}^{-1}}^{40 \text{ nm}^{-1}} q^2 I_{total}(q) dq$  is the total scattered intensity due to both the amorphous and crystalline regions. From the  $q^2 I_{total}(q)$  curves the amorphous contribution is subtracted by hand yielding to  $q^2 I_{crys}(q)$  due to the scattering of the crystalline regions including possible mesomorphic contributions<sup>166,167</sup>. The integral  $A_{crys} = \int_{1.5 \text{ nm}^{-1}}^{40 \text{ nm}^{-1}} q^2 I_{crys}(q) dq$  is the total scattered intensity due to the crystalline regions. The degree of crystallization is then given by  $\chi = A_{crys} / A_{total}$ . In Figure 5.6 the degree of crystallization estimated from the WAXS data are also included to compare with the DSC data. The dependence of  $\chi$  versus the concentration of LDH resembles estimated from the WAXS measurements is similar to the dependence extracted from the DSC (see Fig. 5.6) was also the absolute values agree in the frame of the experimental error. For pure PLA a crystallization degree about 10 % is obtained which is in agreement with literature data (see for instance [168]). Both data sets can be described by the same linear regression leading to a similar critical concentration of ca. 21 wt% LDH were the cold crystallization of PLA is completely suppressed. The agreement of the degree of crystallization estimated from the WAXS investigation and the DSC data for the first heating run is expected because in both cases the samples have the same thermal history (as prepared samples).



The inset of Figure 5.6 compares the degree of crystallization estimated from the first and the second heating run of the DSC measurements versus the concentration of LDH. For the second heating the degree of crystallization measured by DSC is essentially lower than the values obtained by the first heating run. Moreover, in the case of the second heating run the dependence of  $\chi$  on the concentration is stronger than for the first one which gives rise to a lower value for the critical concentration of ca. 14 wt% where  $\chi$  becomes zero (see inset Figure 5.6). This is different to the behavior found for polypropylene and polyethylene filled with LDH. Compared to polypropylene and polyethylene the crystallization rate of PLA is essentially lower. In the case of the first heating run, the samples were cooled down slowly in the press. For the second heating run, the samples were crystallized inside the DSC pan by cold crystallization at a heating rate of 10 K/min. Within the experimental error the different behavior observed for the different thermal histories can be understood by assuming that the main influence of the nanofiller on the cold crystallization behavior is a reduction of the crystallization rate. A detailed DSC study where the cooling rate is varied in a broad range is in progress to investigate this further.

## 5.4 The further analysis of the rigid amorphous phase of MgAl/LDH-PLA nanocomposites

For the following calculations it is important to note that all estimated thermodynamic quantities like crystallization and melting enthalpies as well as the specific heat capacities were normalized to the amount of polymer inside the sample. Under this assumption, the phase fractions of a nanocomposite based on a semicrystalline polymer are defined by<sup>169</sup>

$MAF + CF + RAF = 1$	(5.1)
----------------------	-------

where MAF is the mobile amorphous fraction, CF the crystalline fraction, and RAF the rigid amorphous fraction. CF+RAF can be also considered as the solid fraction SF. For a nanocomposite with a semicrystalline matrix the rigid amorphous fraction can be due to both the crystallites and the nanofiller. Therefore, it holds

$RAF_{all} = RAF_{crystal} + RAF_{filler}$	(5.2)
--	-------

$RAF_{crystal}$  and  $RAF_{filler}$  are the fractions of the rigid amorphous phase due to the crystallites and due to the filler, respectively. Classically, the crystalline fraction CF can be estimated by the melting enthalpy  $\Delta H$  via

$CF = \Delta H / \Delta H_0$	(5.3)
------------------------------	-------

$\Delta H_0$  is the melting enthalpy for a sample with 100% crystallinity which can be for instance taken from data given in the ATHAS database<sup>170</sup>. The mobile amorphous fraction is defined by the amount of segments which vitrify and devitrify during the glass transition and contributes to the heat capacity step at the glass transition temperature. Therefore, the mobile amorphous fraction MAF is estimated from the step height of  $\Delta c_{p,crystal}$  of a semicrystalline or  $\Delta c_{p,amorphous}$  for an amorphous nanocomposite by

$MAF = \Delta c_{p,i} / \Delta c_{p,amorphous \text{ pure polymer}}$	(5.4)
--	-------

where  $\Delta c_{p,amorphous \text{ pure polymer}}$  is the increment of the specific heat capacity at the glass transition of totally amorphous unfilled PLA ( $\Delta c_{p,i} = \Delta c_{p,crystal}$  – semicrystalline nanocomposite;  $\Delta c_{p,i} = \Delta c_{p,amorphous}$  – amorphous nanocomposite). Under the condition that crystallization can be completely avoided,  $\Delta c_{p,amorphous}$  can be estimated by StepScan calorimetry and  $RAF_{all}$  is only due to the nanoparticles ( $RAF_{crystal} = 0$  and  $MAF + RAF_{filler} = 1$ ). By measuring a semicrystalline and an amorphous nanocomposite all

phase fractions can be estimated without any further assumption and the restricted amorphous phase due to the crystals can be calculated by  $RAF_{crystal} = RAF_{all} - RAF_{filler}$  (see also Figure 4.2). The definition of MAF from Eq. 5.4 assumes that no devitrification of RAF takes place in the temperature range where  $\Delta c_p$  is estimated. Generally, whether the RAF can devitrify before melting is an open question even for semicrystalline polymers because it is expected that its devitrification and the overall melting take place in the same temperature range. There are some evidences for poly(ethylene terephthalate) by dielectric spectroscopy that with increasing temperature the amount of RAF decreases<sup>171</sup>. But according to Sargsyan<sup>12</sup> no devitrification is observed for  $RAF_{filler}$  between  $SiO_2$  and PMMA before the degradation of the polymer. It is supposed that there is also a strong interaction between LDH and PLA, and  $RAF_{filler}$  will be stable up to temperatures where cold crystallization sets in.

As discussed above compared to other semicrystalline polymers PLA has long crystallization half time<sup>41, 42</sup>. This means for a high enough cooling rate crystallization can be suppressed as discussed above. Figure 5.7 depicts DSC heating runs at a rate of 10 K/min after cooling with different rates for the sample MgAl-3 wt%. With increasing cooling rate the enthalpy due to cold crystallization increases which indicates that crystallization was partially suppressed during the cooling run and then takes place during the subsequent heating run by cold crystallization. In parallel, the step height at the glass transition increases which evidences that the amount of the amorphous material inside the sample increases and the crystalline fraction decreases.

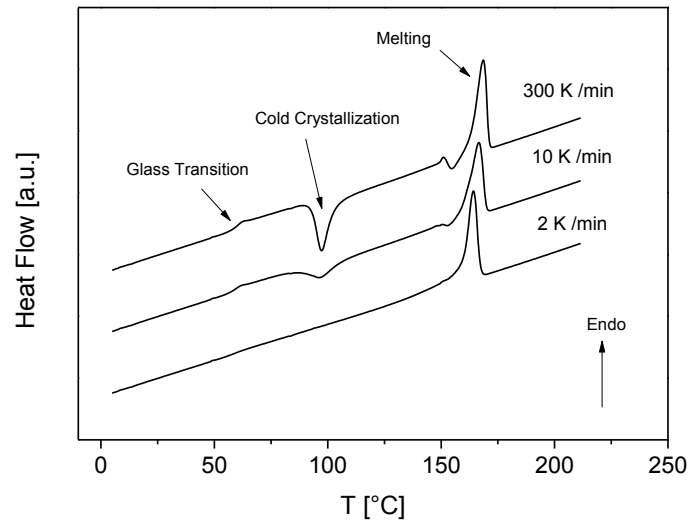


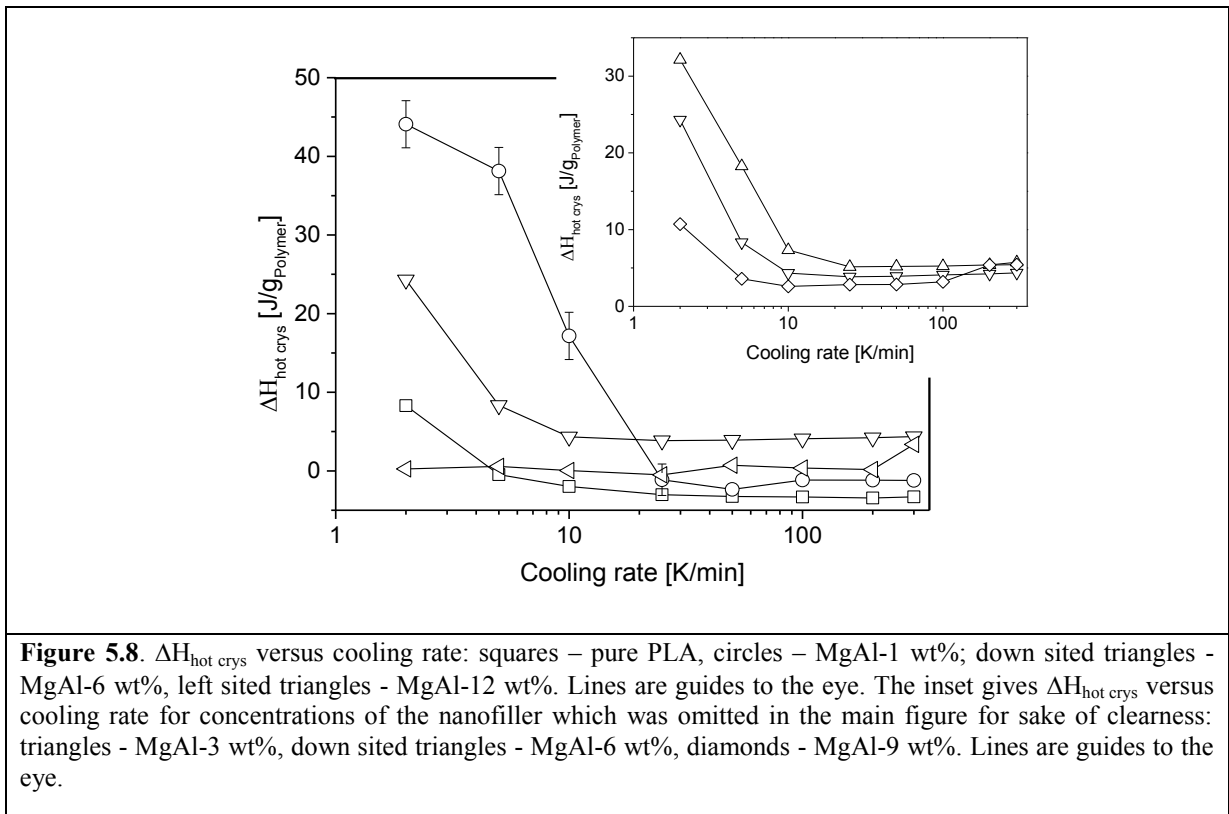
**Figure 5.7.** DSC heating curves at a heating rate of 10 K/min for the sample MgAl-3 wt% which was previously cooled down with the indicating rates. The curves were shifted along the y-scale for sake of clearness.

In the case that the enthalpy due to cold crystallization is equal to the enthalpy of melting this means the whole crystallization process takes place during cold crystallization and not during the cooling process. To characterize this quantitatively the parameter  $\Delta H_{hot\ crys}$  is calculated by

$$\Delta H_{hot\ crys} = \Delta H_{melting} + \Delta H_{cold\ crys}, \quad (5.5)$$

where  $\Delta H_{melting}$  and  $\Delta H_{cold\ crys}$  are the enthalpies of melting and cold crystallization. (Note that in used notation  $\Delta H_{cold\ crys}$  is negative.) In fact this quantity gives the value of the enthalpy due to the crystallization during cooling cycle. On the one hand, this parameter should be equal to the melting enthalpy if crystallization takes completely place during the cooling process and not during the cold crystallization ( $\Delta H_{cold\ crys}=0$ ). On the other hand,  $\Delta H_{hot\ crys}$  should be (ideally) zero if crystallization is completely suppressed during the cooling run ( $\Delta H_{melting} = -\Delta H_{cold\ crys}$ ). Both  $\Delta H_{melting}$  and  $\Delta H_{cold\ crys}$  were obtained by integrating the heat flows due to melting and cold crystallization employing a single peak baseline from above the melting peak down to above the glass transition<sup>172</sup>. Figure 5.8  $\Delta H_{hot\ crys}$  is plotted versus the cooling rate for selected concentrations of the nanofiller. (The inset of Figure 5.8 gives the data for the nanofiller concentrations which have been omitted in the main figure for the sake of clearness). For the pure PLA,  $\Delta H_{hot\ crys}$  decreases

with increasing cooling rate. For high cooling rates ( $\beta > 10 \text{ K/min}$ )  $\Delta H_{\text{hot crys}}$  becomes approximately zero which indicates that crystallization was completely suppressed during the cooling process. For the sample with 1 wt% of the nanofiller (MgAl-1 wt%) for a low cooling rate  $\Delta H_{\text{hot crys}}$  is much higher than for pure PLA. This result indicates a higher degree of crystallinity for MgAl-1 wt% than for pure PLA. This was already discussed in detail in Ref. [173], that for low concentrations of MgAl the nanofiller acts as nucleating agent. With increasing cooling rate  $\Delta H_{\text{hot crys}}$  decrease and becomes approximately zero for higher cooling rates like for pure PLA. For the samples MgAl-3 wt% to MgAl-9 wt% a similar dependence of  $\Delta H_{\text{hot crys}}$  on the cooling rate is observed where the absolute value of  $\Delta H_{\text{hot crys}}$  decreases with increasing concentration of the nanofiller (see Figure 5.8 and inset of Figure 5.8). The decrease of  $\Delta H_{\text{hot crys}}$  with increasing concentration of the nanofiller evidences that crystallization is more and more suppressed by the presence of the nanofiller (see also Ref. [168]). For the sample MgAl-12 wt%  $\Delta H_{\text{hot crys}}$  is approximately zero and independent on the cooling rate, indicating that crystallization during



cooling is completely suppressed for the selected conditions and this concentration of the nanofiller. It should be noted that for some samples  $\Delta H_{\text{hot crys}}$  is not ideal zero as expected.

This is due to uncertainties in the estimation of  $\Delta H_{\text{cold crys}}$  and  $\Delta H_{\text{melting}}$  which is in the range of ca.  $\pm 5$  J/g. Some typical error bars are also given in Figure 5.8.

For cooling rates higher than 25 K/min  $\Delta H_{\text{hot crys}}$  is zero for all concentrations of the nanofiller in the limit of the experimental uncertainties. This evidences that crystallization is suppressed for cooling rates higher than 25 K/min. Therefore, 100 K/min was selected as cooling rate to prepare completely amorphous nanocomposites for the following StepScan DSC investigations to estimate the different phase fractions in dependence on the concentration of the nanofiller (see Figure 4.2). It should be noted that recently a comparable approach to suppress the crystallization of a series of polypropylenes was developed by Schawe<sup>174</sup> employing Fast Scanning Calorimetry where a different method was used to estimate the critical cooling rate.

The crystalline fraction was estimated by conventional DSC (see Figure 4.2).

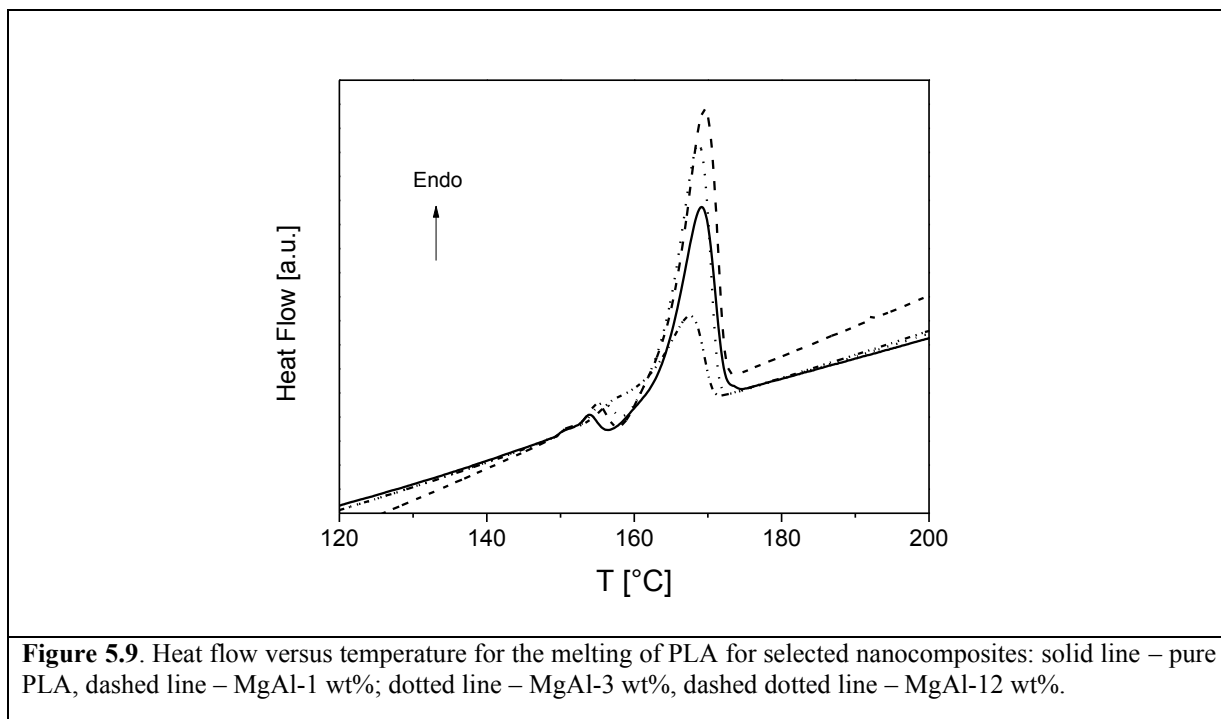
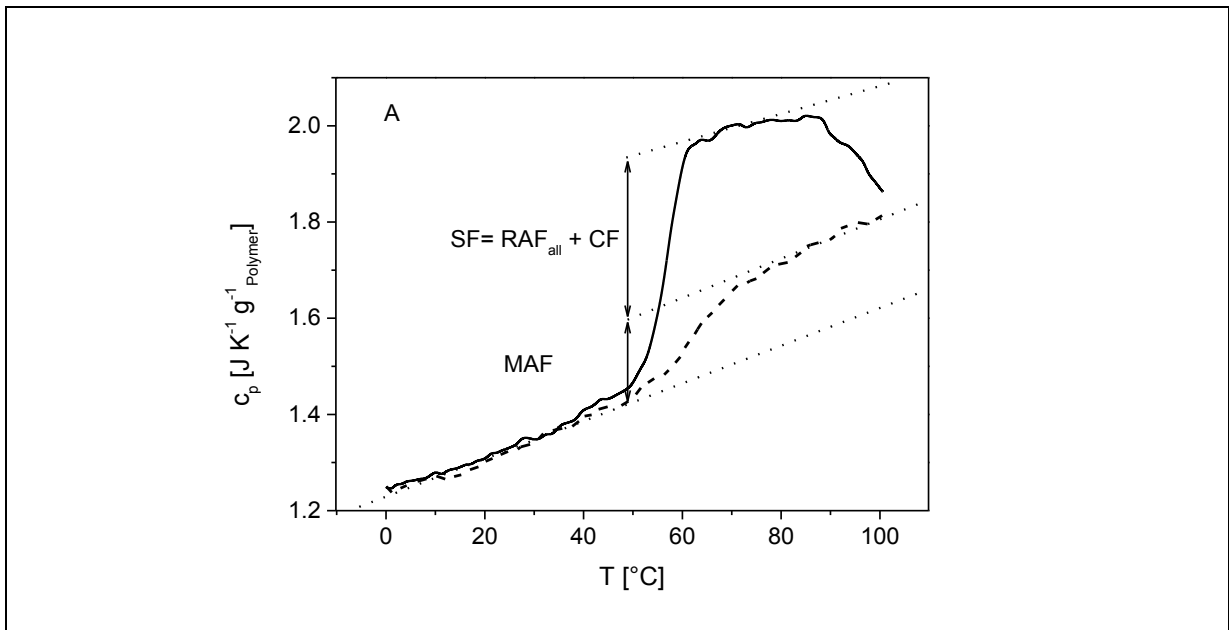
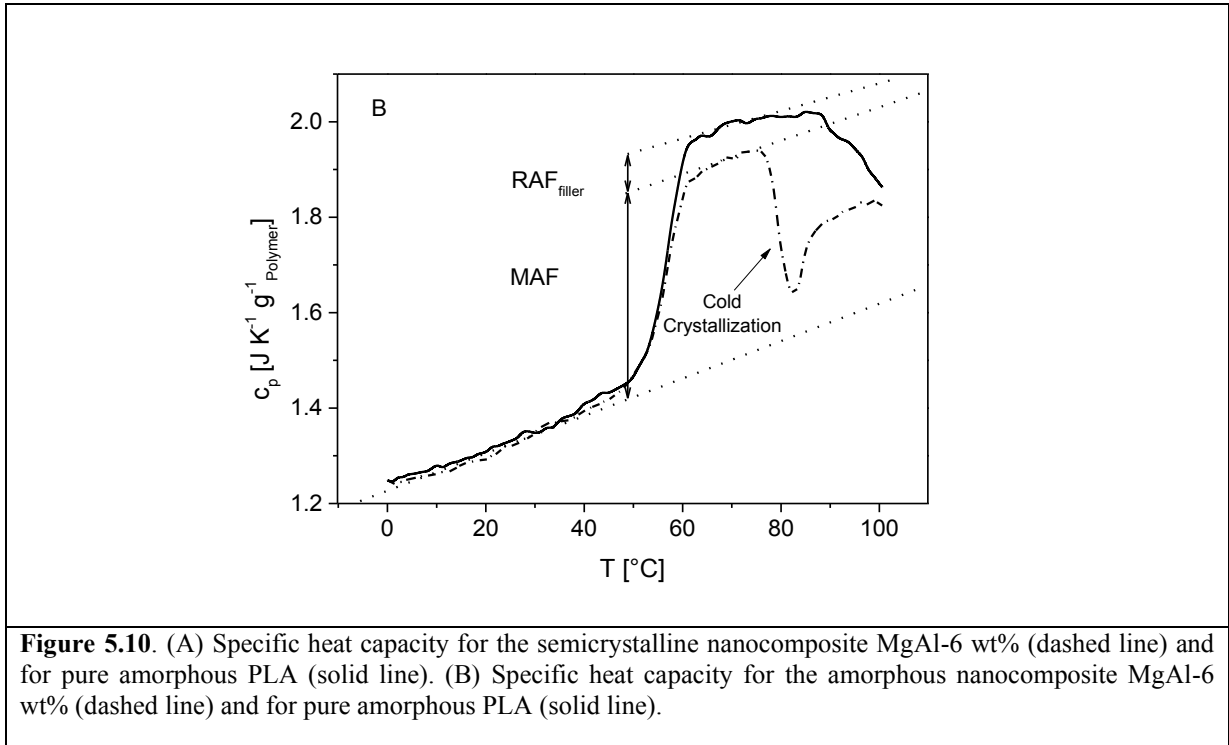


Figure 5.9 gives the heat flow in the temperature range of the melting of PLA for selected concentrations of the nanofiller. As discussed above, firstly the melting enthalpy increases for low concentrations of LDH compared to pure PLA as the nanofiller acts as nucleating agent. With increasing concentration of the nanofiller  $\Delta H$  decreases as crystallization is suppressed by the presence of the nanofiller (see Table 5.1). The reduced ability to crystallize might be related to a reduced mobility in the interface between nanoparticle and polymer matrix and therefore to the formation of  $\text{RAF}_{\text{filler}}$ . The melting enthalpy was

estimated by integrating the corresponding peak in the heat flow and the crystalline fraction CF was calculated according to Eq. 5.3 and given in Table 5.1. Here, for  $\Delta H_0$  a value of 93.7 J/g is used<sup>175, 176</sup>.

Figure 5.10a compares the temperature dependence of the specific heat capacity at thermal glass transition temperature for a crystallized nanocomposite with 6 wt% of MgAl-LDH with that of pure amorphous PLA as one example. Due to the CF and  $RAF_{all}$  the increment of the specific heat at the glass transition temperature is much smaller for the crystallized nanocomposites compared to the pure amorphous PLA. Because the CF is known, the mobile amorphous fraction can be estimated by Eq. 5.4 and  $RAF_{all}$  can be calculated using Eq. 5.1 for each concentration of the nanofiller. Further, Figure 5.10b depicts the specific heat capacity of the amorphous nanocomposite MgAl-6 wt% in comparison to pure amorphous PLA. In that case the missing part in the increment of  $\Delta c_p$  compared to  $\Delta c_{p,amorphous}$  is only due to  $RAF_{filler}$  which can be calculated as described. Because  $RAF_{all}$  is known  $RAF_{crystal}$  can be estimated by  $RAF_{crystal}=RAF_{all}-RAF_{filler}$ . A similar behavior is observed for all other concentrations of the filler and the different mass fractions are summarized in Table 5.1.



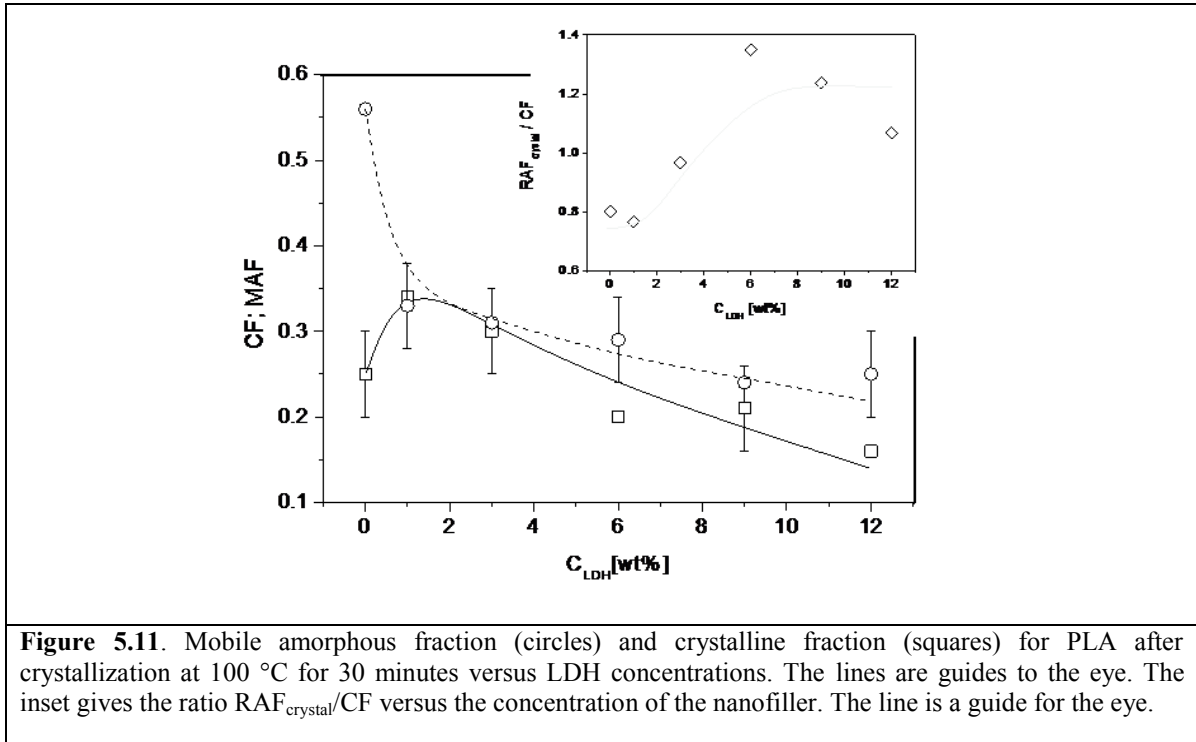


Although the MAF and CF are derived straightforward from the DSC measurement, there are some sources of errors. Besides the uncertainties which result from the integration of enthalpy peaks and the estimations of heat capacity increments there can be possible contributions of excess heat capacity<sup>177-180</sup> which can contribute to  $\Delta c_p$ . Furthermore latent heat contributions due to polymorphic phase transition<sup>181-182</sup> during crystallization and melting process could not be excluded completely. A detailed discussion of these effects is beyond the scope of this work.

**Table 5.1.** Sample codes, glass transition temperatures, thermodynamic quantities normalized to the weight of the polymer, and phase fractions calculated by Eqs 5.1-5.4.

	Pure PLA	MgAl-1 wt%	MgAl-3 wt%	MgAl-6 wt%	MgAl-9 wt%	MgAl-12 wt%
$T_g$ (°C)	57.3	61.5	60.4	61.7	59.9	59.7
$\Delta H_{melting}$ (J/g <sub>Polymer</sub> )	23.0	31.6	27.5	17.8	17.7	13.0
$\Delta c_p$ (J/g <sub>Polymer</sub> *K)	0.27	0.16	0.15	0.14	0.11	0.11
$\Delta c_{p,amorphousm}$ (J/g <sub>Polymer</sub> *K)	0.49	0.46	0.43	0.36	0.32	0.25
MAF	0.56	0.33	0.31	0.29	0.24	0.25
CF	0.25	0.34	0.30	0.20	0.21	0.16

RAF <sub>filler</sub>	0	0.07	0.10	0.23	0.30	0.42
RAF <sub>crystal</sub>	0.20	0.26	0.29	0.27	0.26	0.17



MAF and CF are plotted versus concentrations in Figure 5.11. As it is already clear from the raw data, CF increases for 1 wt% of LDH compared to pure PLA under the given crystallization conditions. With further increase of the concentration of LDH the crystalline fraction decreases. The MgAl LDH nanofiller inhibit the crystallization process of PLA. For pure PLLA 30 min at 100 °C exceeds the crystallization time necessary to obtain a full crystallized sample<sup>183</sup>. So the obtained CFs represent the maximal possible degree of crystallization of the PLA based nanocomposite for the given concentration of LDH.

For pure PLA the mobile amorphous fraction is maximal (see Figure 5.11). With increasing content of the LDH nanofiller the MAF decreases drastically for 1 wt% of LDH. This strong drop down of MAF is at the one hand side due to the formation the rigid amorphous phase from the filler particles. On the other hand for 1 wt% of LDH both the degree of crystallization and the RAF<sub>crystal</sub> related to this increased CF is also increased. With further increase of the concentration of the filler particles the MAF decreases further

but with a decreased rate. It is worth noting that the decrease of MAF with  $C_{LDH}$  is much weaker than that of CF ( $C_{LDH}$ ).

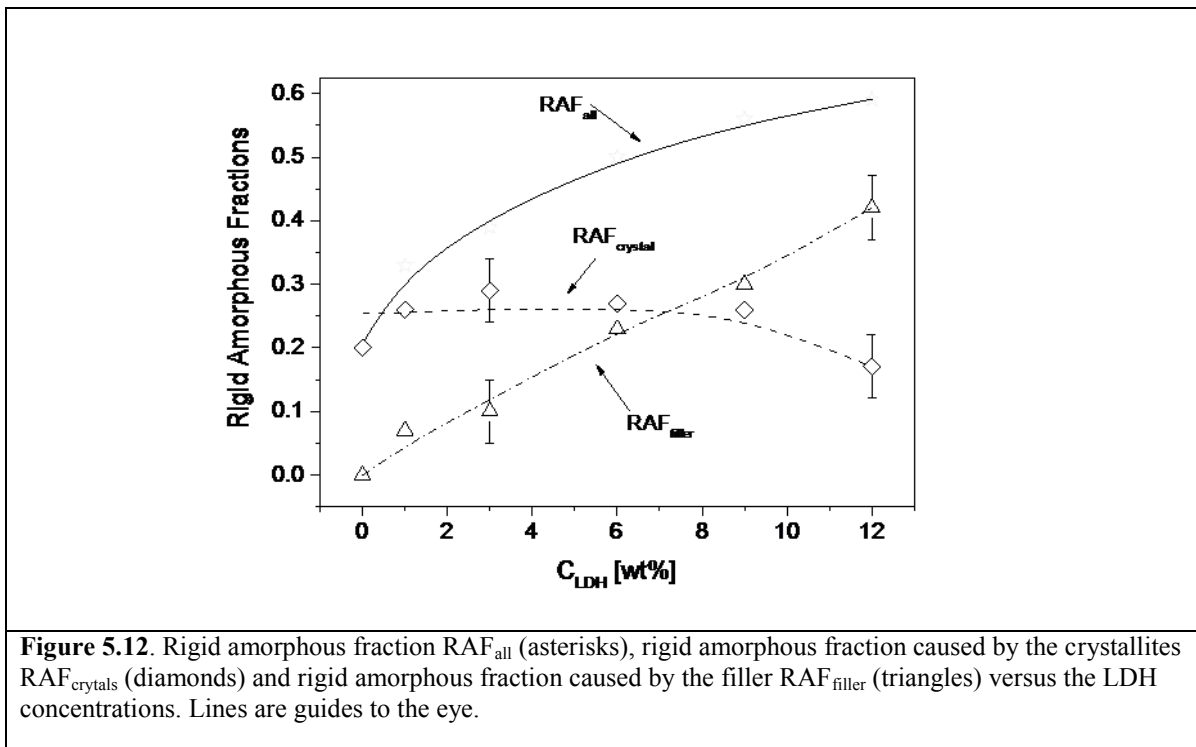
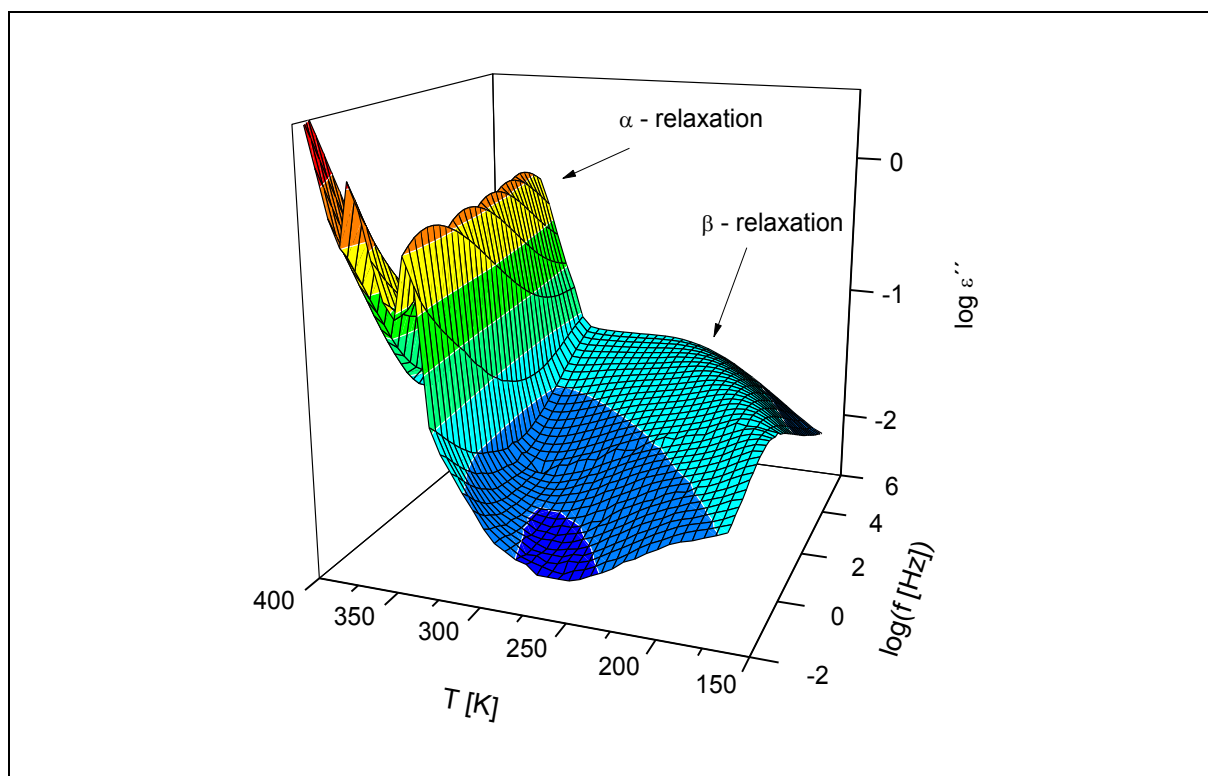


Figure 5.12 gives the estimated fractions of RAF versus the concentration of the filler particles.  $RAF_{filler}$  increases with increasing content of the LDH filler as expected. The increase of  $RAF_{all}$  with the concentration of LDH is thus due to an almost linear increase of  $RAF_{filler}$  with  $C_{LDH}$ . This means that in the considered concentration range each filler particle produces the same amount of RAF.

$RAF_{crystal}$  seems to be more or less constant and in the frame of the errors independent of the concentration of the nanoparticles. For the highest concentration of LDH there might be a small decrease of  $RAF_{crystal}$ . To estimate the relationship between the crystal fraction and  $RAF_{crystal}$  the ratio  $RAF_{crystal}/CF$  is calculated and plotted versus the concentration of the nanofiller in the inset of Figure 5.11. The ratio  $RAF_{crystal}/CF$  seems to increase with the concentration of the nanofiller and is not a constant as expected. For approximately 6 wt% of LDH a constant value of ca. 1.1 is reached. According to Righetti *et al.*<sup>17</sup>  $RAF_{crystal}$  depends on the chain mobility at the crystallization temperature. Here the samples are crystallized isothermally at 100 °C. Probably, the chain mobility and crystal growth are restricted by the nanofiller. This can lead to a higher amount of  $RAF_{crystal}$  for LDH-PLA nanocomposites with higher nanofiller concentrations compared to the pure PLA.

## 5.5 Dielectric spectroscopy analysis for the MgAl/LDH-PLA nanocomposites

The dielectric measurements were carried out for the as prepared samples. Figure 5.13 displays the dielectric loss  $\epsilon''$  of pure PLA versus frequency and temperature in a 3D representation. The dielectric response of a material is related to the fluctuation of dipole moments which is related to the molecular mobility of groups or segments<sup>87</sup>. As known in the literature bulk polylactide shows at least two relaxation processes indicated by peaks in the dielectric loss  $\epsilon''$  (see for instance [184, 185, 186]). The  $\beta$ -relaxation at low temperatures is assigned to localized fluctuations. At temperatures higher than the  $\beta$ -process,



**Figure 5.13.** Dielectric loss for pure PLA versus frequency and temperature and a 3D representation.

the  $\alpha$ -relaxation (dynamic glass transition, segmental dynamics) takes place.

To discuss the dielectric behavior in more detail the dielectric loss for pure PLA is plotted versus temperature at fixed frequency of  $10^3$  Hz (see Figure 5.14). The  $\alpha$ - and the  $\beta$ -relaxations are seen as prominent peak in the dielectric loss at high and low temperatures respectively. A closer inspection of the dielectric spectra reveals that there seems to be an additional process in between the  $\alpha$ - and the  $\beta$ -relaxation. The molecular origin of this relaxation process is not clear till now. Therefore a second heating run carried out. In the second heating cycle this intermediate process seems to disappear. But

also the  $\beta$ -relaxation shifts to higher temperatures and broadens (see Figure 5.14). In parallel the intensity of the  $\alpha$ -relaxation drops down and the peak shifts slightly to higher temperatures. This behavior points to an increased degree of crystallinity. To avoid such effects in the analysis of the nanocomposites here only the pure PLA samples are considered.

The model function introduced by Havriliak/Negami<sup>187</sup> (HN-function) is used to analyze the dielectric measurements quantitatively. The detail was already introduced by Equation 3.39 in Section 3.3.2.

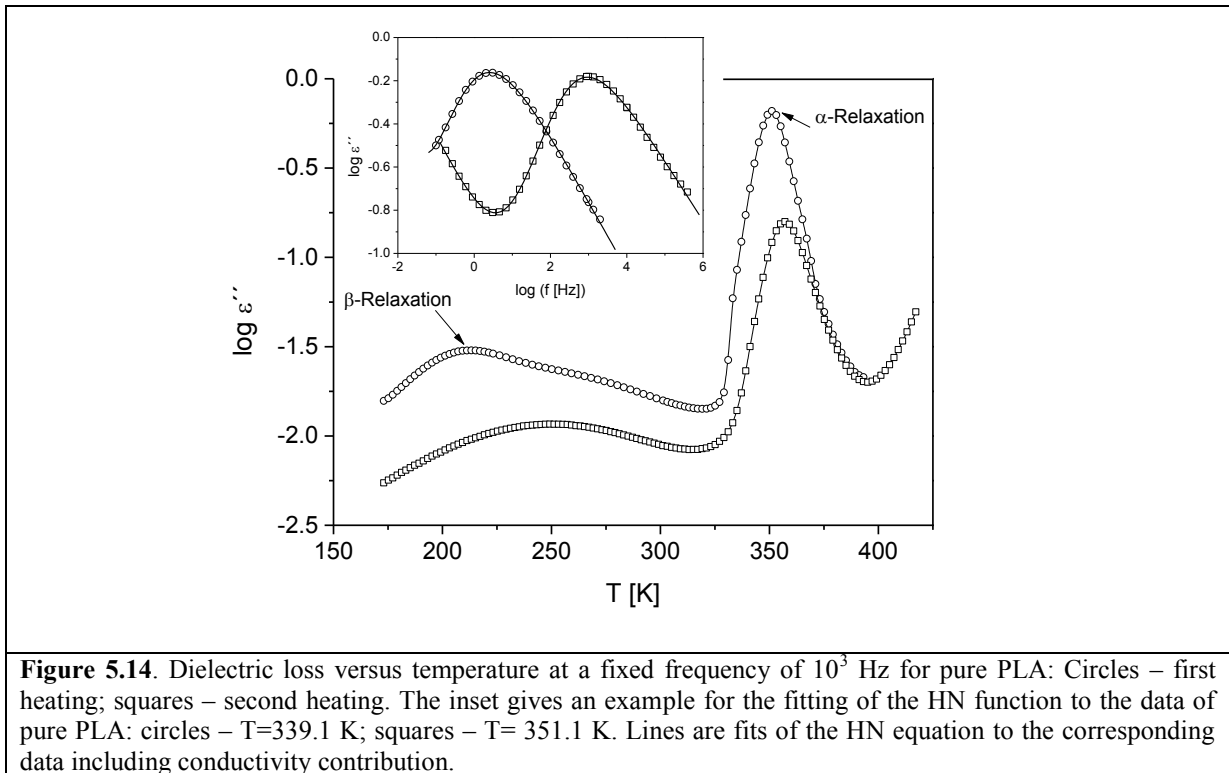


**Figure 5.14.** Dielectric loss versus temperature at a fixed frequency of  $10^3$  Hz for pure PLA: Circles – first heating; squares – second heating. The inset gives an example for the fitting of the HN function to the data of pure PLA: circles –  $T=339.1$  K; squares –  $T=351.1$  K. Lines are fits of the HN equation to the corresponding data including conductivity contribution.

Figure 5.15 depicts the temperature dependence of the relaxation rate of the  $\alpha$ -relaxation for pure PLA in the relaxation map. As expected for segmental (glassy) dynamics the temperature dependence of  $f_{p,\alpha}$  is curved when plotted versus  $1/T$  which can be described by the Vogel/Fulcher/Tammann (VFT-) equation<sup>188-190</sup>, the temperature dependence of the relaxation rate of the  $\beta$ -relaxation follows the Arrhenius equation (see inset of Figure 5.15). Both equations were already introduced as Equation 2.1 and 2.3 in Section 2.3.2, no need to give repeated descriptions here.

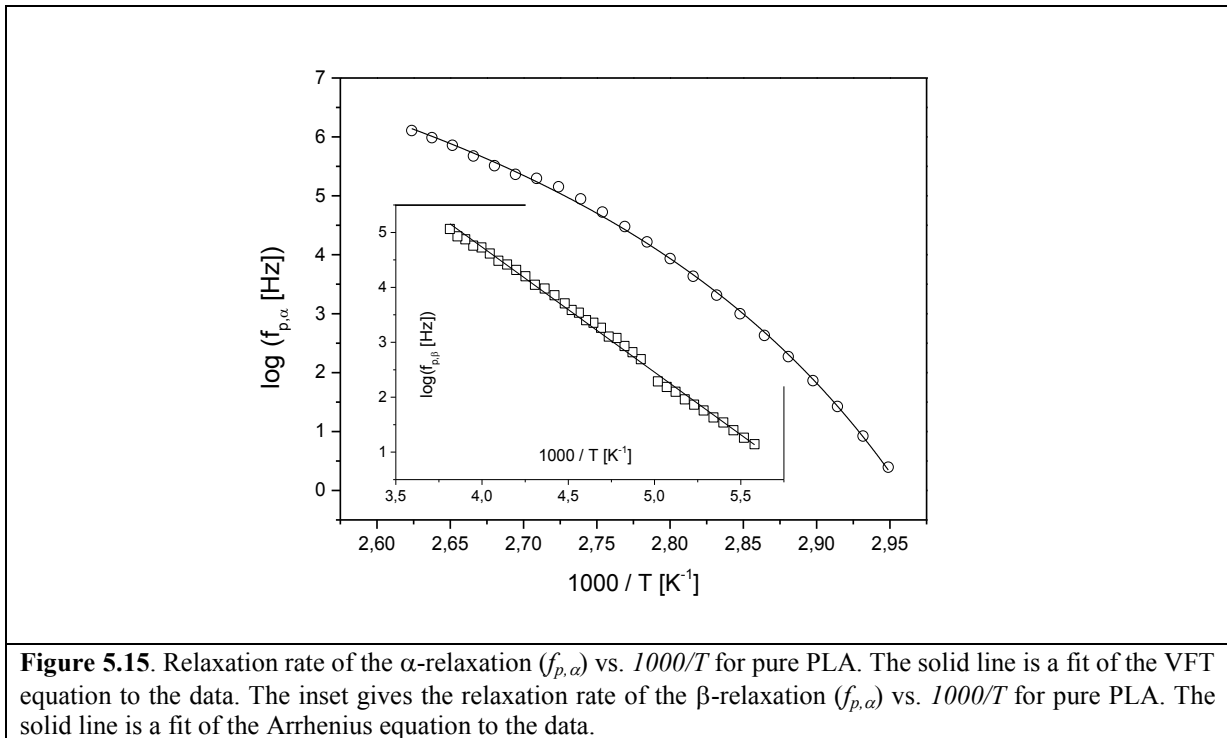


Figure 5.16 compares the dielectric loss in the temperature domain for pure PLA and different nanocomposites. Compared to pure PLA besides the  $\alpha$ - and the  $\beta$ -relaxation which were also observed for the nanocomposites three additional features are found: (1) In the temperature range around 260 K an additional peak is observed which increases in intensity with increasing concentration of LDH (relaxation region 1). (2) A further process is also observed in the temperature around 310 K (relaxation region 2). (3) At temperature above the  $\alpha$ -relaxation a third relaxation process appears which increases strongly in its intensity with increasing LDH concentration (relaxation region 3). These features will be discussed in detail in the following.

**Relaxation region 1:** Because of the fact that the intensity of this relaxation region increases with increasing concentration of LDH it is obvious that this process is related to the nanoparticles. The only polar component in the system which increases with the concentration of LDH is the bulky anion dodecyl benzene sulfonate (SDBS). Therefore it is concluded that relaxation region 1 is related in some manner to molecular fluctuations of SDBS. There are only few investigations which consider the dynamics of the alkyl chains inside the galleries of a pure layered material [191,192]. In the case of neat montmorillonite a disordered hydrocarbon trilayer formed by the surfactant molecules is evidenced by simulation [193]. For the nanocomposites the SAXS measurements show that they have a partly exfoliated morphology. In the presence of polymer segments the

alkyl tails of the surfactant (here SDBS) are desorbed further from the surface of the nanoparticles and form a phase mixed with the polymer segments. This means the polymer segments close to the layers will fluctuate together with the CH<sub>2</sub> groups of the alkyl chains of the surfactant. Relaxation region 1 is therefore assigned to common fluctuations of polymer segments and tail groups of the surfactant or in other words fluctuations of PLA segments promoted by the presence of SDBS and the nanofiller. Its analysis will provide information about the dynamics close to the layers.

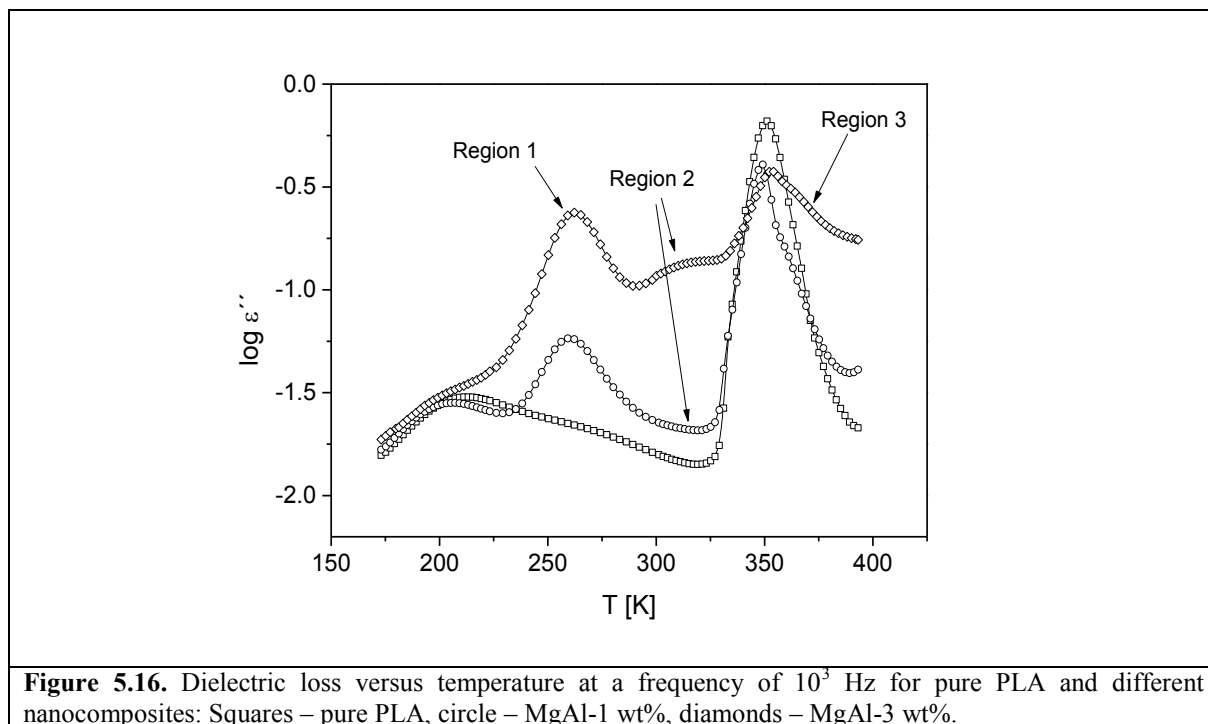


Figure 5.17 give the temperature dependence of the relaxation rate of the relaxation region 1 in the relaxation map. For all concentrations of the nanofiller the relaxation rates for relaxation region 1 collapse into one chart. Its temperature dependence is curved when plotted versus  $1/T$ . This result indicates that the underlying molecular fluctuations show a glassy dynamics. For all concentrations the temperature dependence of the relaxation rate can be described by a common fit of the VFT equation to the data.

The inset A of Figure 5.17 compares the temperature dependence of relaxation of relaxation region 1 for MgAl-6 wt% with the temperature dependence of a similar process found for a nanocomposite based on MgAl/LDH and polyethylene also for ca. 6 wt-% of the filler (PE6). The relaxation processes found for the two different systems show a close similarity. They are observed in the same temperature range and seem to have the same temperature dependence. To analyze the temperature dependence in more detail a

derivative technique is employed<sup>194</sup>. This method is sensitive to the functional form of  $f_p(T)$  irrespective of the prefactor. For a dependency according to the VFT-equation one gets

$\left[ \frac{d \log f_p}{dT} \right]^{-1/2} = T - T_0$	(5.9)
---	-------

In a plot of  $\left[ d \log f_p / dT \right]^{-1/2}$  versus  $T$  a VFT-behavior shows up as a straight line. This technique is applied to the data given in the inset A of Figure 5.17 and plotted in inset B of the same Figure. Firstly, both data sets follow a straight line confirming the VFT temperature dependence of the relaxation rates. Secondly, the data for ZnAl/LDH-PE-6 wt% and MgAl/LDH-PLA-6 wt% collapse into one chart. This result gives some evidence that the both processes for the different systems have a similar molecular origin. The common structural features present in both systems are the SDBS molecules. The similarities in the both processes are suggested that both relaxation modes are closely related to the fluctuations of the polar SDBS surfactant molecules modified by polymer segments. These, molecules are located close to the surface of the exfoliated layers or to the surface of the nano-stacks.

The VFT temperature dependence of the relaxation rate of relaxation region 1 indicated glassy dynamics in the interfacial region between the nanofiller and the PLA matrix. To have a signature as a glass transition the spatial extent of these regions should be in the order of 1 to 3 nm<sup>195-200</sup>.

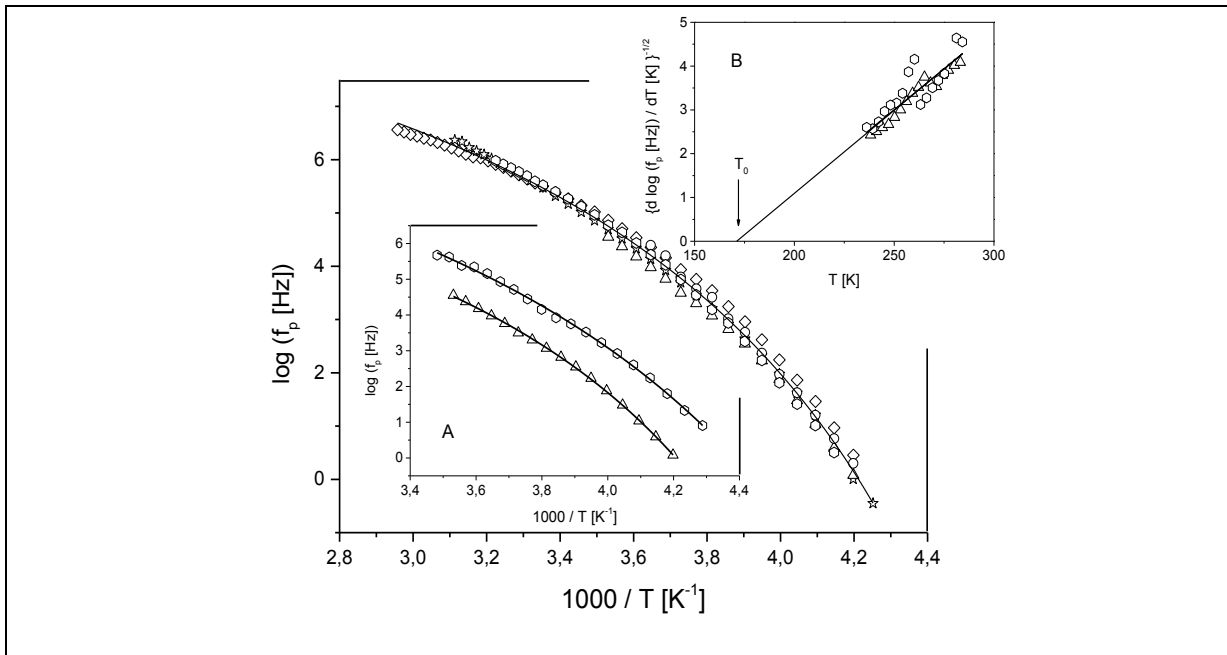


**Figure 5.17.** Relaxation rates of the relaxation region 1 versus  $1/T$  for different nanocomposites: circle – PLA 1 wt%, diamonds – PLA 3 wt%, triangles – PLA 6 wt%, hexagons – PLA 9 wt%, stars – PLA 12 wt%. The line is a fit common of the VFT equation to all data. Inset A gives the relaxation rate for PLA 6 wt% (triangles) and PE-6 wt% (hexagons) versus  $1/T$ . The lines are fits of the VFT equation to the corresponding data. Inset B gives  $[d \log f_p / dT]^{-1/2}$  versus  $T$  for PLA-6 wt% (triangles) and PE-6 wt% (hexagons). The line is a linear regression using both data sets.

**Relaxation region 2:** The relaxation region 3 can be observed for all concentrations of LDH. But  $C_{LHD}=1$  wt% is quite weak (see Figure 5.16) and for LDH concentrations higher than 3 wt% it is strongly overlaid by relaxation region 3 and conductivity effects. Therefore it can be analyzed unambiguously only for MgAl-3 wt%. Figure 5.18 gives the dielectric loss for the nanocomposite MgAl-3 wt% versus frequency and temperature in a 3D representation. The different relaxation region are evidenced by peaks in the dielectric loss and indicated by arrows. The relaxation region 2 is located between relaxation region 1 and the  $\alpha$ -relaxation. The temperature dependence of the relaxation rate of relaxation region 2 seems to be quite

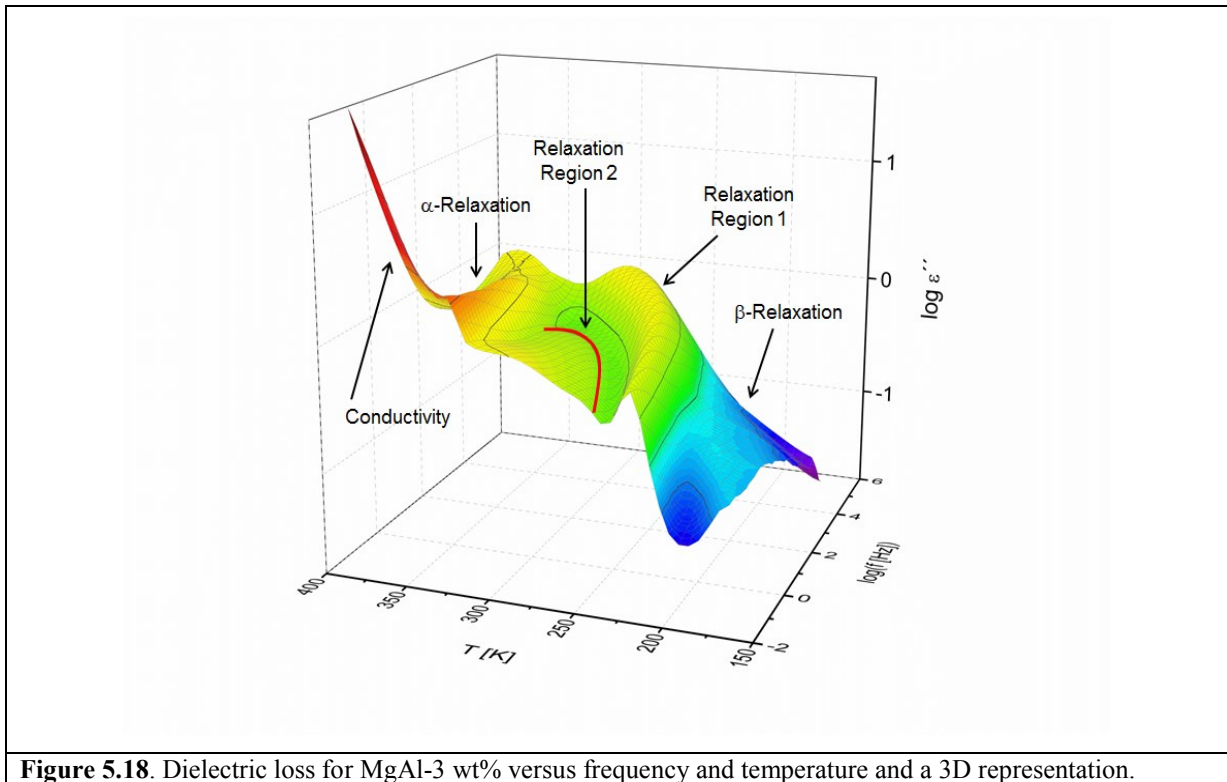
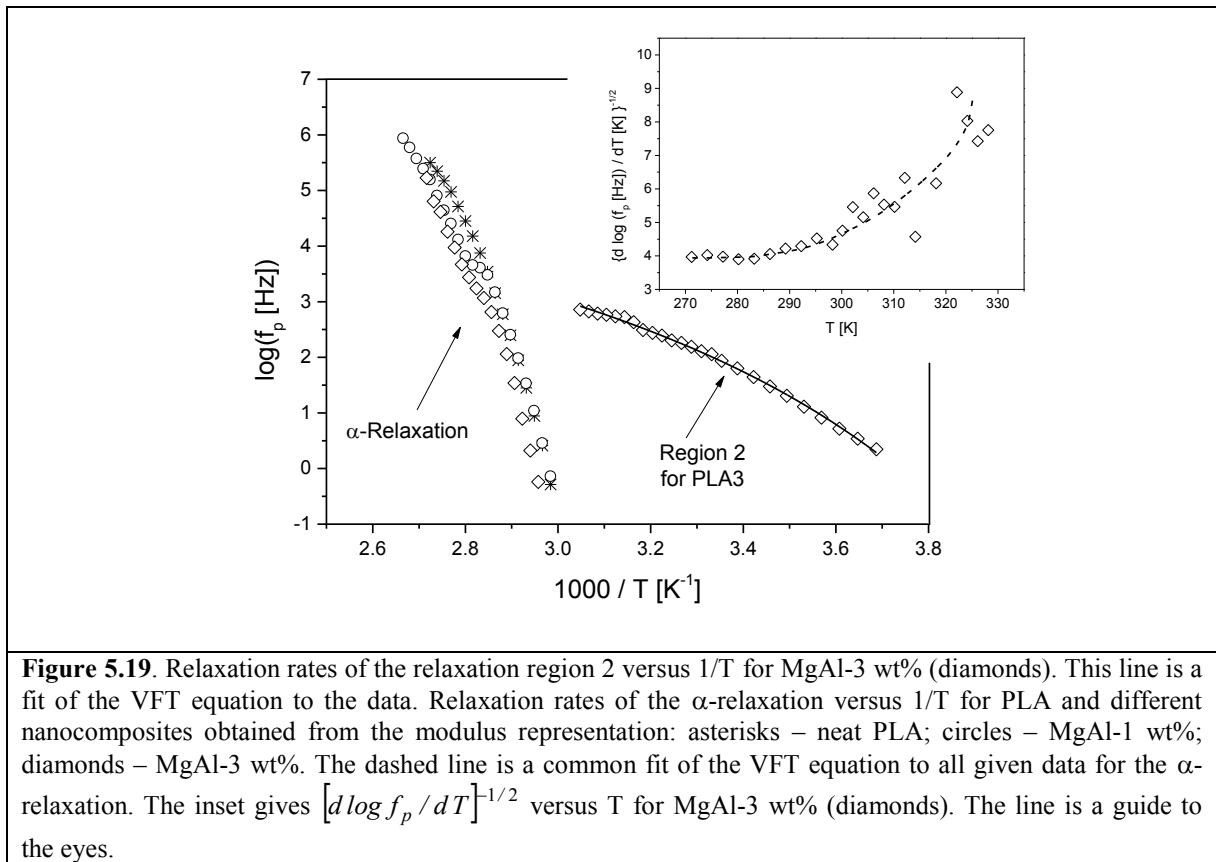


**Figure 5.18.** Dielectric loss for MgAl-3 wt% versus frequency and temperature and a 3D representation.

unusual. The temperature dependence of this relaxation process seems to have a saddle-like shape. At low temperatures the relaxation rates increases with increasing temperatures as expected. Then the relaxation rates have maximum before they seems to decrease again. A similar behavior was observed for nanocomposite systems bases on a maleic anhydride grafted polypropylene and organophilic modified montmorillonite clay.

To analyze this behavior in more detail Figure 5.19 depicts the temperature dependence of the relaxation rate of the relaxation region 2 for MgAl-3 wt% that is curved when plotted versus  $1/T$ . At the first glance the data seems to follow a VFT temperature dependence. But however a fit of the VFT equation to the data results in a prefactor  $\log(f_{\infty} [\text{Hz}]) \approx 6$  that is much too small for a true relaxation process. The inset of Figure 5.19 gives  $[d \log f_p / dT]^{-1/2}$  versus  $T$  for this process. The data can be described neither by an Arrhenius law nor by the VFT equation. This gives evidence that the temperature dependence of relaxation region 2 have a saddle-like temperature dependence. Such a saddle-like behavior is found besides the nanocomposite system discussed above also for pure LDH materials<sup>201</sup>. This saddle-like pattern of the relaxation rate seems to be characteristic for systems which contains some amount of water in the presence of a nanoporous structure<sup>202, 203</sup>. In a model of Rybaov et al. it is assumes that the saddle-like

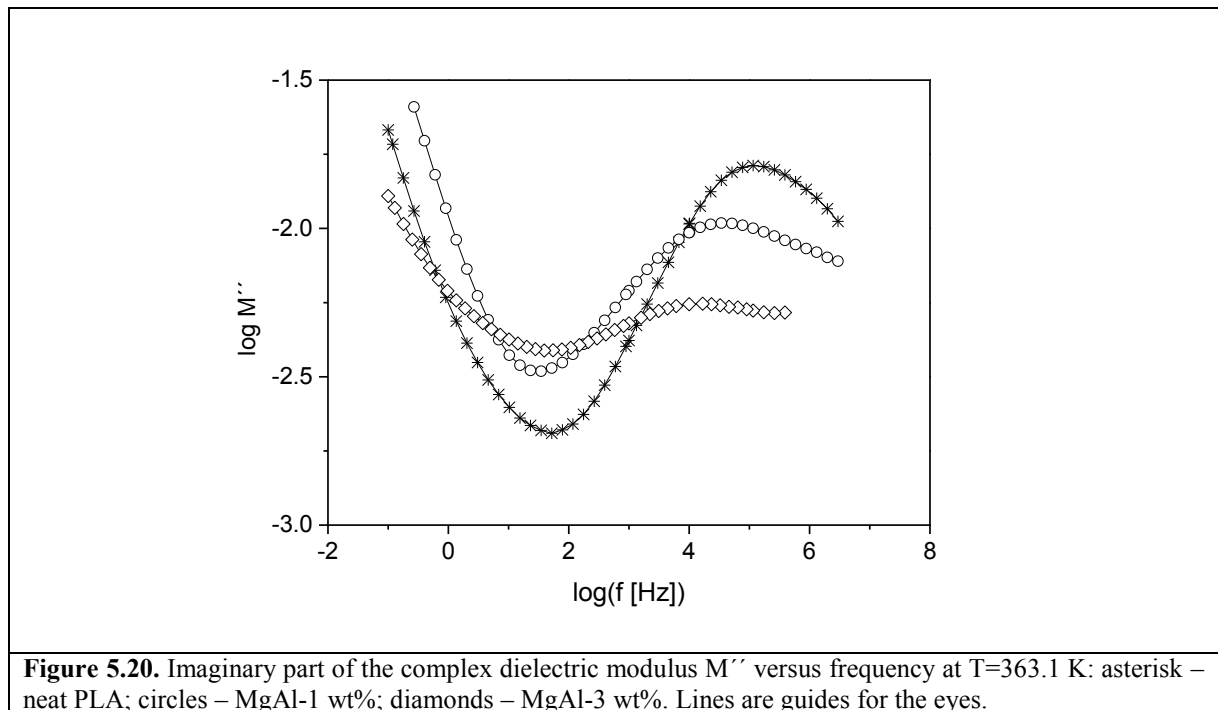
temperature dependence of the relaxation rate must be due to the counterbalance of two competing processes<sup>204</sup>. Firstly, the rotational fluctuation should have an activated temperature according to the Arrhenius equation. Secondly, the nanoporous structure will give rise to some free volume defects which will have a different temperature dependence. The combination of both effects will lead to a saddle-like temperature dependence. In the systems considered here some water is present in the intergalleries of the LDH although the filler is carefully dried in vacuum. Moreover the layered structure gives rise to given porosity. Therefore, it is concluded that relaxation region 2 is related to rotational fluctuations of water molecules in the presence of defects.



**$\alpha$ -Relaxation:** For the analysis of the  $\alpha$ -relaxation the modulus representation is used where the complex electrical modulus  $M^*$  is related to complex dielectric function by  $M^*(\omega)\epsilon^*(\omega)=1$ <sup>205</sup>. Figure 5.20 gives the modulus data for neat PLA and two nanocomposites with the lowest concentration of LDH for  $T=363.1$  K. Like for the complex dielectric function the  $\alpha$ -relaxation is characterized by a peak also in the modulus representation. Also the HN-function can be used to analyze the data. Besides the data for relaxation region 2, Figure 5.19 gives also the relaxation rates for the  $\alpha$ -relaxation. For all

given concentrations the relaxation rates collapse nearly into one chart together with data for neat PLA. This indicates that this process is due to the  $\alpha$ -relaxation of the polymeric matrix which is not influenced by the nanofiller. This is in agreement with the results obtained by DSC that  $T_g$  does not depend on the filler concentrations (see Figure 5.5). It is also in agreement with literature studies for other polymer based nanocomposites (see for instance [206,207] but also for other nanostructured systems like ultrathin films (see for instance [208-212]). A closer inspection of the temperature dependence shows that the data for the nanocomposite seems to have some kink-like change towards higher temperatures at ca. 375 K (see also Figure 5.20). Probably this effect is due to the onset of the cold crystallization which is shifted to lower temperatures by the presence of the nanoparticles (see Figure 5.5) the lower heating rate in the dielectric compared to the DSC experiments.

The only influence of the nanoparticles to the  $\alpha$ -relaxation is an almost symmetrical broadening of the relaxation peak with increases with increasing concentration of LDH (see Figure 5.20). For higher concentrations of LDH the  $\alpha$ -relaxation is strongly overlaid



by process 3 and conductivity phenomena and cannot be analyzed quantitatively.

**Relaxation region 3:** Figure 5.21 gives the imaginary part of the complex electrical modulus for the nanocomposites MgAl-6 wt% and MgAl-9 wt%. The spectra show two pronounced peaks. At the first glance the peak at higher frequencies might be assigned to

the  $\alpha$ -relaxation in these composites because of some similarities in the frequency position. But a more careful consideration reveals that the intensity of these peaks is much too high for the  $\alpha$ -relaxation (compare Figure 5.21 and 5.20). Also the extracted temperature dependence of the relaxation rate of that peak is completely different from that of the  $\alpha$ -relaxation. In parallel to the peaks observed in the imaginary part of the modulus  $M''$  a giant increase of the real part of the complex function  $\epsilon'$  with decreasing is observed (see inset of Figure 5.21). Such a strong increase of  $\epsilon'$  with decreasing frequency cannot be explained by a molecular dipole moment present in the system and is considered to be typical for interfacial polarization effects. Generally such an interfacial polarization process is caused by (partial) blocking of charge carriers at internal surfaces or interfaces of different phases having different values of the dielectric permittivity and/or conductivity at a mesoscopic length scale or at electrodes.

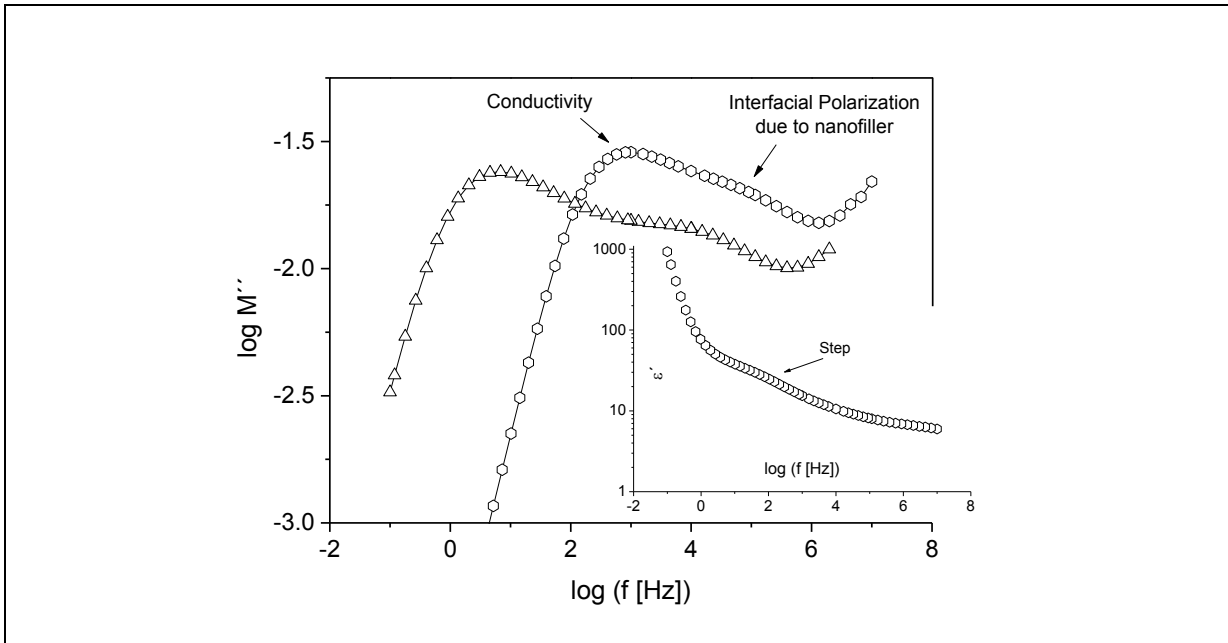


**Figure 5.21.** Imaginary part of the complex dielectric modulus  $M''$  versus frequency at  $T=363.1$  K: triangles – MgAl-6 wt%; hexagons – MgAl-9 wt%. Lines are guides for the eyes. The inset gives the real part of the complex dielectric function for MgAl-9 wt% at  $T=361.1$  K.

In the considered system the Maxwell / Wager / Sillars polarization effects can have two different origins: The blocking of the charge carriers at the crystallites and/or the blocking of the charge carriers at the LDH nanofiller (LDH nanostacks and exfoliated layers). Because of the facts that the dielectric data of neat PLA does not show interfacial polarization effects and that the strongest Maxwell/Wagner/Sillars signal were observed

for the highest concentration of the nanofiller the high frequency peak in the modulus spectrum is assigned to interfacial polarization effects caused by the nanofiller.

In the modulus representation a conductivity contribution is transformed into a peak. Therefore the peak observed at lower frequency in the modulus representation is assigned to the conductivity (see Figure 5.21). From the maximum position of that peak a rate for the conductivity  $f_{\text{Cond}}$  can be extracted.

Again the sum of two HN-functions can be employed to analyze the data. Figure 5.22 gives the temperature dependence of the rate of the conductivity for two concentrations of LDH. Generally for both concentrations of LDH is quite complex and cannot be described neither by an Arrhenius nor by the VFT equation. The reason for that is unclear up to now and further investigations are needed. A possible explanation is the cold crystallization process above the glass transition temperature.

Compared to MgAl-6 wt% the rate for the conductivity is much shorter for MgAl-12 wt% (see Figure 5.22). Because of the fact that  $f_{\text{Cond}}$  is proportional to the DC conductivity that means that for MgAl-12 wt% the conductivity is more than one order of magnitude higher than for MgAl-6 wt%. With increasing LDH also the concentration of SDBS is increased. Compared to apolar polyolefines for the more polar PLA the SDBS molecules may desorb from the LDH into the polymeric matrix and cat a ionic charge carriers which enhance conductivity.

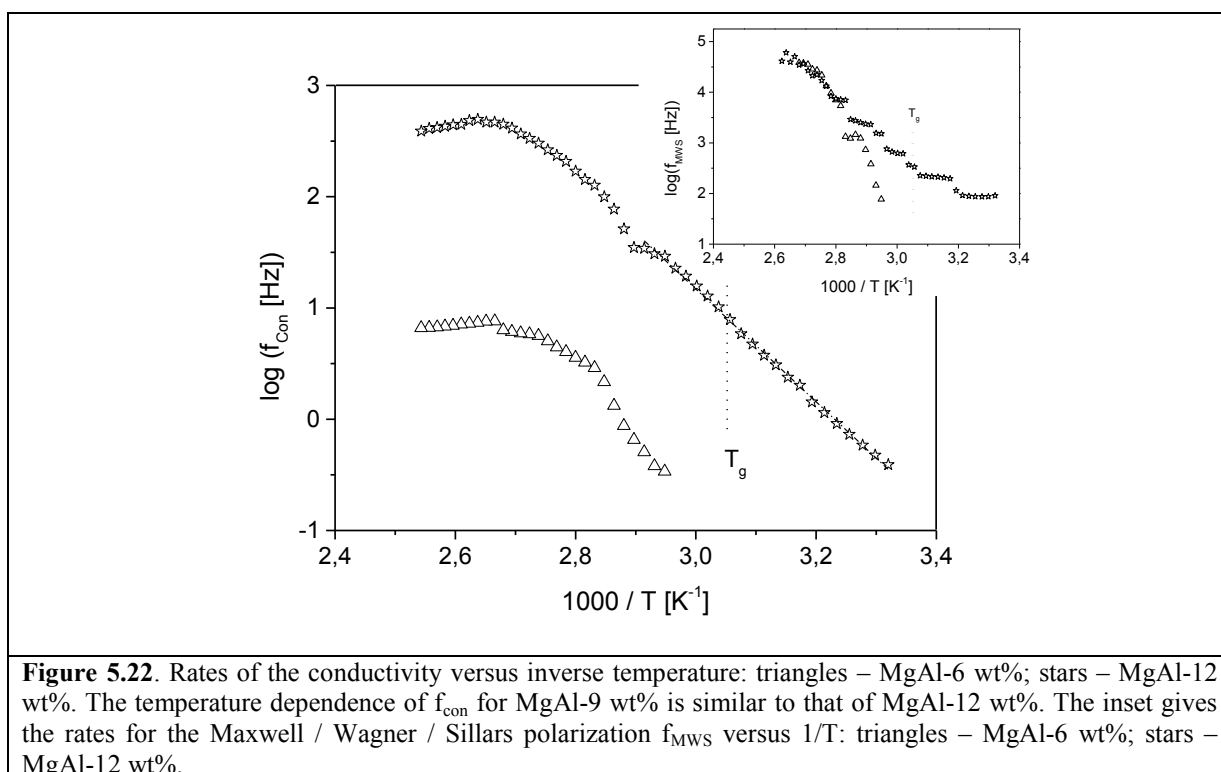


**Figure 5.22.** Rates of the conductivity versus inverse temperature: triangles – MgAl-6 wt%; stars – MgAl-12 wt%. The temperature dependence of  $f_{\text{con}}$  for MgAl-9 wt% is similar to that of MgAl-12 wt%. The inset gives the rates for the Maxwell / Wagner / Sillars polarization  $f_{\text{MWS}}$  versus  $1/T$ : triangles – MgAl-6 wt%; stars – MgAl-12 wt%.

This is interesting to note that for MgAl-12 wt% a considerable conductivity is observed even below the thermal glass transition. As discussed above the interfacial regions between the polymeric matrix and the nanofiller have a high molecular mobility (see discussion relaxation region 1). For high concentrations of LDH the amount of this interfacial area is high which can lead to a percolating network of high mobility regions. Charge transport can take place within this percolating network even at temperature below  $T_g$ .

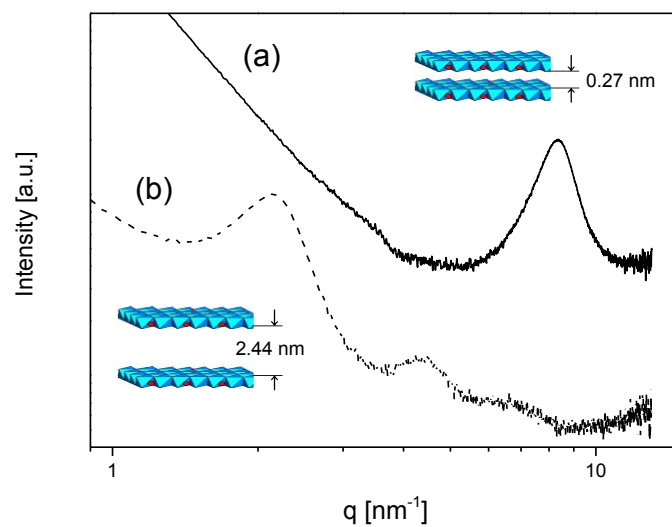
To be complete in the inset of Figure 5.22 the temperature dependence of the rate for the Maxwell/Wagner/Sillars polarization  $f_{MWS}$  is given for the same two concentrations of LDH. Due to the overlapping of the both processes the data have a considerable scatter. Also these temperature dependencies are complex and resemble similarities to that of the conductivity.



## Chapter 6 Investigation of PLA nanocomposites based on NiAl-LDH and a comparison with its MgAl-LDH counterpart

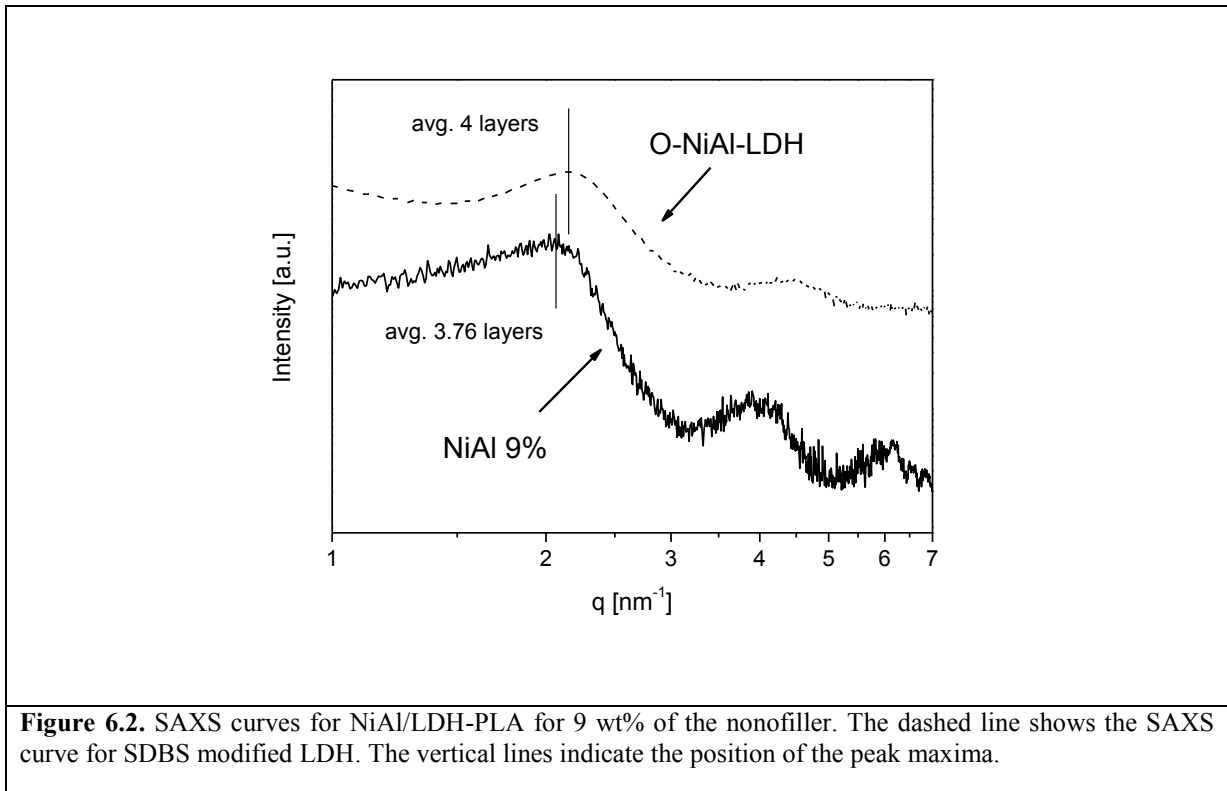
### 6.1 Characterization of modified LDH and the PLA nanocomposites by SAXS

Figure 6.1 depicts the SAXS patterns for O-NiAl/LDH and U-NiAl/LDH. For unmodified LDH SAXS data shows a reflection at  $8.3 \text{ nm}^{-1}$ . This is a characteristic for a layered compound corresponding to a lamellar repeat distance ( $d = 2\pi/q_{peak}$ ) of  $d = 0.76 \text{ nm}$ . An effective interlayer distance of  $0.27 \text{ nm}$  was obtained by subtracting the thickness of the hydroxide brucite-like LDH of ca.  $0.49 \text{ nm}$ . By fitting Gaussians to the data, the peak width is determined as  $w = 1.54 \text{ nm}^{-1}$ . From the width, a mean correlation length perpendicular to the lamella normal can be calculated to be  $l_c = 2\pi/w = 4 \text{ nm}$ . Assuming that lattice distortions can be neglected in a first approximation the crystallite thickness in the direction normal to the (001) plane can be estimated. This calculation gives that the average number of layers in a stack of the unmodified LDH is approximately 5.6. For the modified LDH, the lamellar reflections shift to lower  $q$ -values. Three equidistant reflections are visible. No reflection at  $q=8.3 \text{ nm}^{-1}$  characteristic for of O-LDH is observed that proves the absence of significant amounts of U-NiAl/LDH. A similar analysis as discussed above can also be carried out for O-NiAl/LDH. After the subtraction of the thickness of the brucite sheet, the layer distance is estimated to be  $2.44 \text{ nm}$  which is slightly smaller than observed for MgAl/LDH-PLA. The introduction of SDBS leads to an essential widening of the distance between the layers as expected. The width of the peak for the O-NiAl/LDH is estimated to be  $0.68 \text{ nm}^{-1}$ . If this value is compared with the data of U-NiAl/LDH, the number of layers in a stack of the modified LDH is calculated to be ca. 4 that is smaller than the value obtained for U-NiAl/LDH. The estimated values for NiAl/LDH are also a bit smaller than the values obtained for MgAl/LDH (layer distance  $2.54 \text{ nm}$ ; number of layers in the stack 6; see reference [5]).



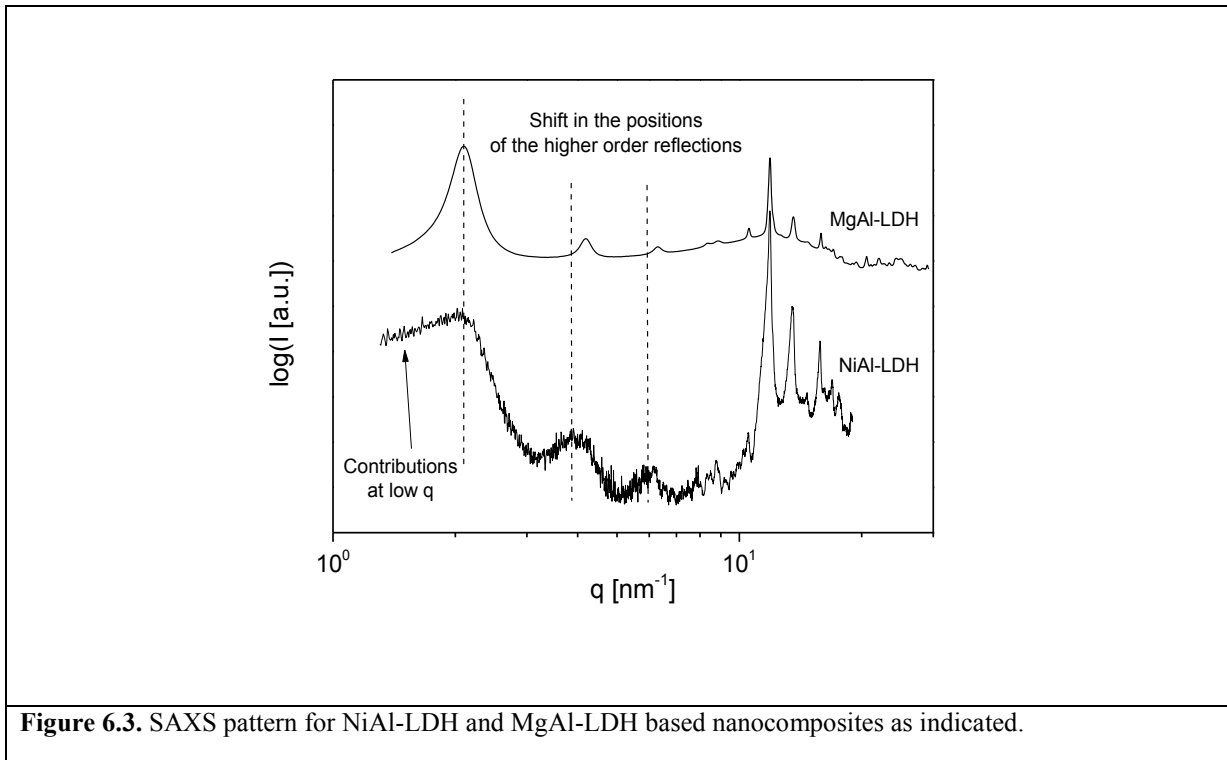
**Figure 6.1.** SAXS pattern of (a) unmodified and (b) organically modified NiAl/LDH.

Figure 6.2 depicts the SAXS pattern for NiAl 9 wt% as one example. For the nanocomposite the main peak shifts slightly to lower  $q$ -values ( $q_{\text{max}}=2.05 \text{ nm}^{-1}$ ) indicating a widening of the layer distance to 2.57 nm compared to O-NiAl/LDH. This is a first hint for an intercalated structure of the NiAl/LDH-PLA nanocomposite. The stack size was determined to be 8.9 nm, which is equivalent to ca. 3.76 layers. The  $l_c$  value for the nanocomposites is slightly smaller than the value of O-NiAl/LDH.



**Figure 6.2.** SAXS curves for NiAl/LDH-PLA for 9 wt% of the nonfiller. The dashed line shows the SAXS curve for SDBS modified LDH. The vertical lines indicate the position of the peak maxima.

Figure 6.3 compares the SAXS pattern for NiAl/LDH-PLA with that for MgAl/LDH-PLA for a concentration of 9 wt%. For the nanocomposite with the NiAl/LDH nanofiller, the peak at ca.  $2 \text{ nm}^{-1}$  has a pronounced broadening for lower  $q$ -values. This behavior indicates that the NiAl/LDH based nanocomposites have a broader distribution of interlayer distances, which is shifted to larger values of the interlayer distances. These results further points to a more intercalated structure of the NiAl/LDH-PLA nanocomposites in comparison to material based on MgAl/LDH, which is partly exfoliated as discussed in reference [5]. This interpretation is further supported by the observation that also the higher order reflection of the stack-like structures are shifted to lower  $q$ -values for NiAl/LDH-PLA. Similar results were found for the other concentrations of LDH, too. Therefore, it is concluded that the structure of the NiAl/LDH based nanocomposites is predominantly intercalated.



**Figure 6.3.** SAXS pattern for NiAl-LDH and MgAl-LDH based nanocomposites as indicated.

## 6.2 Characterization of Degradation stability of the nanocomposites by SEC

The metal ions consist in the LDH materials may cause a catalytic degradation effect for the PLA matrix. One reference<sup>213</sup> already reported a lower thermal stability of a similar PLA/LDH nanocomposites system. Therefore, Size Exclusion Chromatography was employed to investigate the degradation under ambient conditions at room temperature after 3 years. As discussed in reference [5] the elugrams show two signals. The main one at shorter elution times (higher molecular weights) corresponds to macromolecules of the matrix where the (lower molecular weights) is due to degradation products. The inset of Figure 6.4 gives the molecular weight distribution for the high molecular weight elution peak for the different NiAl/LDH concentrations. With increasing concentration of LDH, the peak maximum shifts slightly to lower molecular weight. This means with increasing concentration of LDH the molecular weight of the matrix decreases due to catalytic degradation.

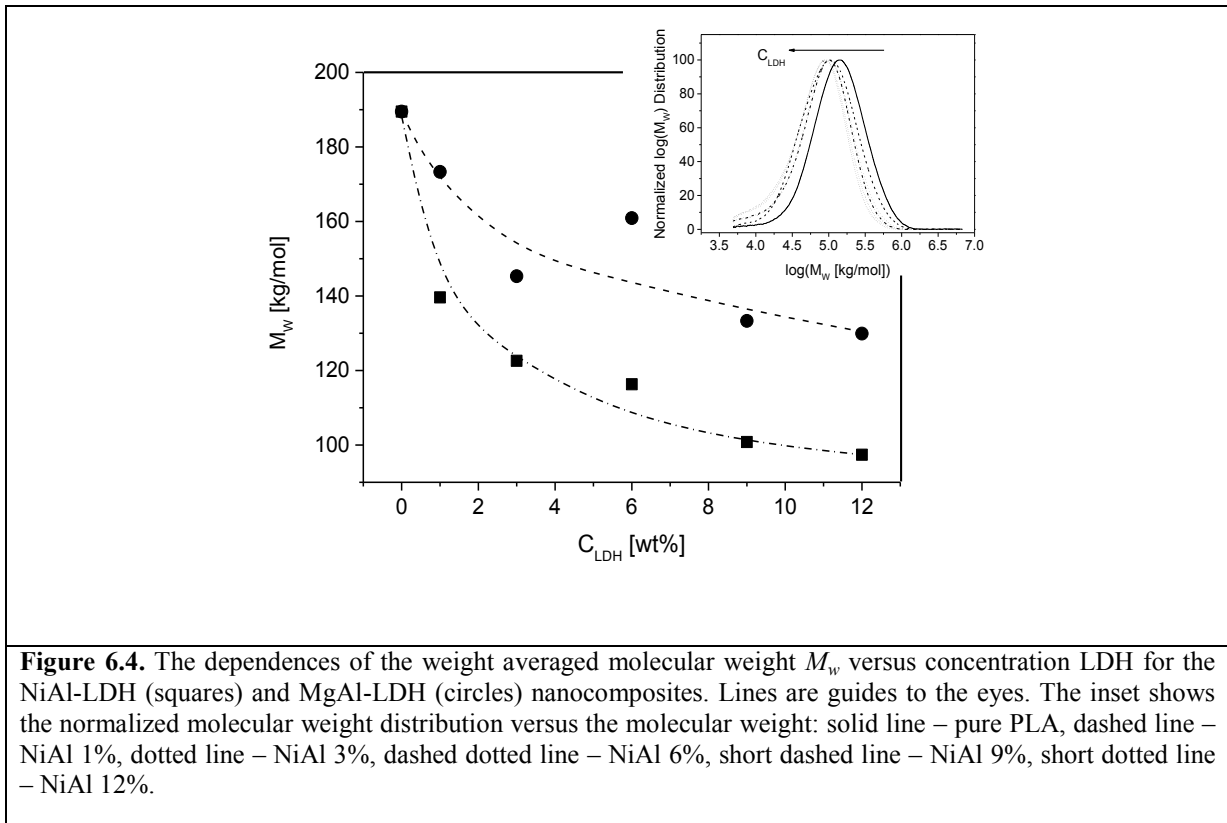


Figure 6.4 compares the weight averaged molecular weight  $M_w$  versus the concentration of LDH for MgAl and NiAl/LDH-PLA nanocomposites. For MgAl/LDH-PLA nanocomposites, the  $M_w$  decreases from 190 kg/mol of neat PLA to about 130 kg/mol for 12 wt% of the nanofiller, while the  $M_w$  of NiAl/LDH-PLA nanocomposites decreases to about 97 kg/mol. This means the NiAl/LDH filler causes a somewhat stronger degradation than MgAl/LDH. This behavior might be attributed to the different properties of the Ni and Mg ions. Reference [59] shows that the thermal degradation of a different LDH/PLA nanocomposite system is controlled by the unzipping depolymerization catalyzed by metal components in LDH. It might be that combination of Ni and Al is more effective for the degradation reaction than the combination of Mg and Al. Moreover, except the catalysis of metal ions, the residual water molecule between the interlayers of LDH may also contribute to the degradation process<sup>214</sup>. Nevertheless, the change of the polymer molecular weight is not strong enough to significantly influence the properties investigated here.

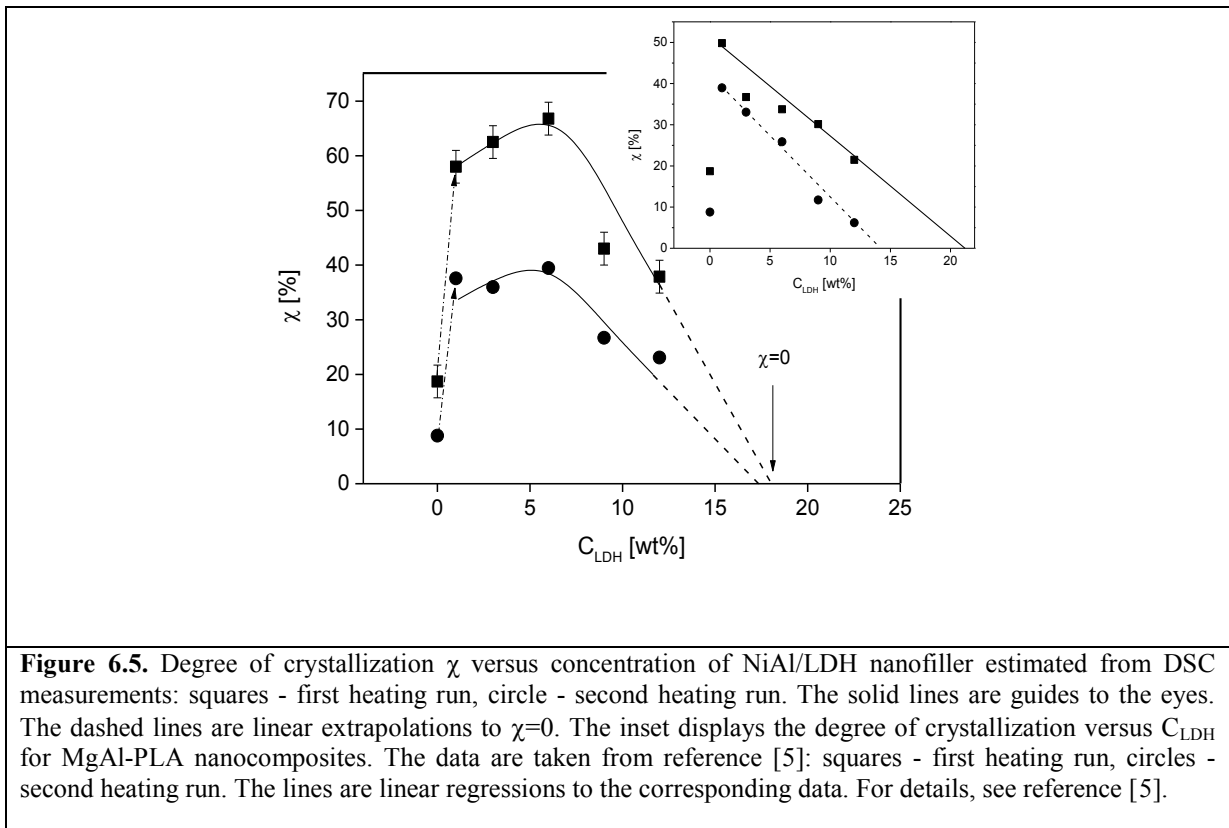
### 6.3 Crystallization analysis of the nanocomposites investigated by DSC and WAXS

**Table 6.1.** Crystallization Temperature ( $T_c$ ), Melting Temperature ( $T_m$ ), normalized crystallization enthalpy ( $\Delta H_{c,nor}$ ) and normalized melting enthalpy ( $\Delta H_{m,nor}$ ) obtained from the first heating, the first cooling and the second heating processes in the DSC measurement.

	First Heating					Cooling	
	$T_c$ [K]	$\Delta H_{c,nor}$ [J/g]	$T_m$ [K]	$\Delta H_{m,nor}$ [J/g]	$\chi$ [%]	$T_c$ [K]	$\Delta H_{c,nor}$ [J/g]
Pure	383.8	-15.8	441.7	18.4	18.7	–	–
1%	–	–	448.9	53.9	58	373.8	-9.8
3%	–	–	446.5	58.1	62.5	378.9	-12.4
6%	–	–	447.7	62.1	66.8	375.2	-21.3
9%	–	–	441.5	40	43	–	–
12%	354.8	-17.2	439.8	35.2	37.9	–	–
	Second Heating						
	$T_c$ [K]	$\Delta H_{c,nor}$ [J/g]	$T_m$ [K]	$\Delta H_{m,nor}$ [J/g]	$\chi$ [%]		
Pure	404.2	-6.76	434.2	8.2	8.8		
1%	376.9	-22.4	442.5	35.7	37.6		
3%	377.1	-19.3	440.2	35.6	36.0		
6%	374.8	-13.1	439.7	36.7	39.5		
9%	389.1	-27.4	434.6	30.0	36.7		
12%	392.1	-25.2	433.2	27.7	23.0		

The thermal properties of NiAl/LDH-PLA nanocomposites were investigated by DSC measurements. The results are given in Table 6.1. The obtained enthalpy values are normalized by the content of the polymer. Considering the preparation procedure of NiAl/LDH-PLA nanocomposites, the as prepared samples were slowly cooled down from melted state. From the melting enthalpies the degree of crystallization can be calculated according to  $\chi = (1 - C_{LDH})\Delta H_m / \Delta H_{m,100\%} * 100$ , where  $\Delta H_{m,100\%}$  is the melting enthalpy of a

complete crystalline unfilled PLA sample. A value of  $\Delta H_{m,100\%} = 93 \text{ J/g}$  is taken from reference [215]. The degree of crystallization is plotted versus the concentration of LDH in Figure 6.5. First, the as prepared samples (first heating run) are discussed.  $\chi$  increases for  $C_{LDH}=1 \text{ wt\%}$  compared to the bulk value. This means for a small amount of the nanofiller the LDH acts as the nucleating agent. A similar behavior is also observed for other PLA composite systems like completely exfoliated PLA/MMT nanocomposites<sup>216</sup>, PLA/MWNT composites<sup>217</sup>, PLLA/PDLA stereocomplexes<sup>218</sup> and PLA/PEG complexes<sup>219</sup>. With increasing concentration of LDH the degree of crystallinity increases further up to a LDH concentration of 6 wt% (see Figure 6.5.). For concentrations higher than  $C_{LDH}=6 \text{ wt\%}$ ,  $\chi$  decreases sharply.



In the simplest case this dependence can be linearly extrapolated to  $\chi=0$  resulting in a limiting concentration of ca. 18 wt% where the crystallization behavior of the polymer matrix is completely suppressed by the nanofiller.

Prior to the second heating run, the samples were cooled after the first heating cycle within the DSC (from the melted to the glassy state at a cooling rate of 10 K/min). In principle, the dependence of the degree of crystallization estimated from the second

heating shows a similar dependence on the concentration of LDH to that of the first heating cycle (see Figure 6.5.). However, the absolute values of  $\chi$  taken from the second heating are lower than the data estimated from the first heating cycles. This is different for polyolefins filled with LDH<sup>225,226</sup>, where no difference between the first and second heating was observed. For PLA the crystallization rate is substantially lower than polyethylene or polypropylene. In the case of the as prepared samples (first heating run), the samples were slowly cooled down in the press. For the second heating run, the samples were crystallized inside the DSC pan by cold crystallization at a heating rate of 10 K/min. One approach to understand the different behavior observed for the different thermal histories is to assume that the main influence of the nanofiller on the cold crystallization behavior is a reduction of the crystallization rate. To verify this assumption a detailed DSC study is in preparation where the cooling rate is varied in a broad range.

The inset of Figure 6.5 depicts the degree of crystallization versus the concentration of LDH for MgAl-PLA nanocomposites. In general, a related behavior as observed for the NiAl/LDH-PLA system is found. The observed difference is due to the fact that for NiAl/LDH-PLA,  $\chi$  increases further with  $C_{LDH}$  up to 6 wt% while for the MgAl-PLA nanocomposites  $\chi$  starts to decrease for LDH concentrations higher than 1 wt%. This effect is likely related to a different crystallization kinetics for the both systems caused by different sample morphologies. Moreover, it is also discussed in the literature that the amount of dispersion influences the crystallization kinetics in different PLA nanocomposite systems (see references [62-65]).

Figure 6.6 gives the X-ray pattern in the  $q$  value range of the crystalline reflections of PLA. The increase of the crystallinity up to a LDH concentration of 6 wt% can be also deduced from the X-ray measurements. Up to  $C_{LDH}=6$  wt%, the intensity of the main reflection at ca.  $q \approx 12 \text{ nm}^{-1}$  increases with increasing concentration of LDH followed by a decrease for higher values of  $C_{LDH}$ . The reflections are also the sharpest for  $C_{LDH}=6$  wt%.

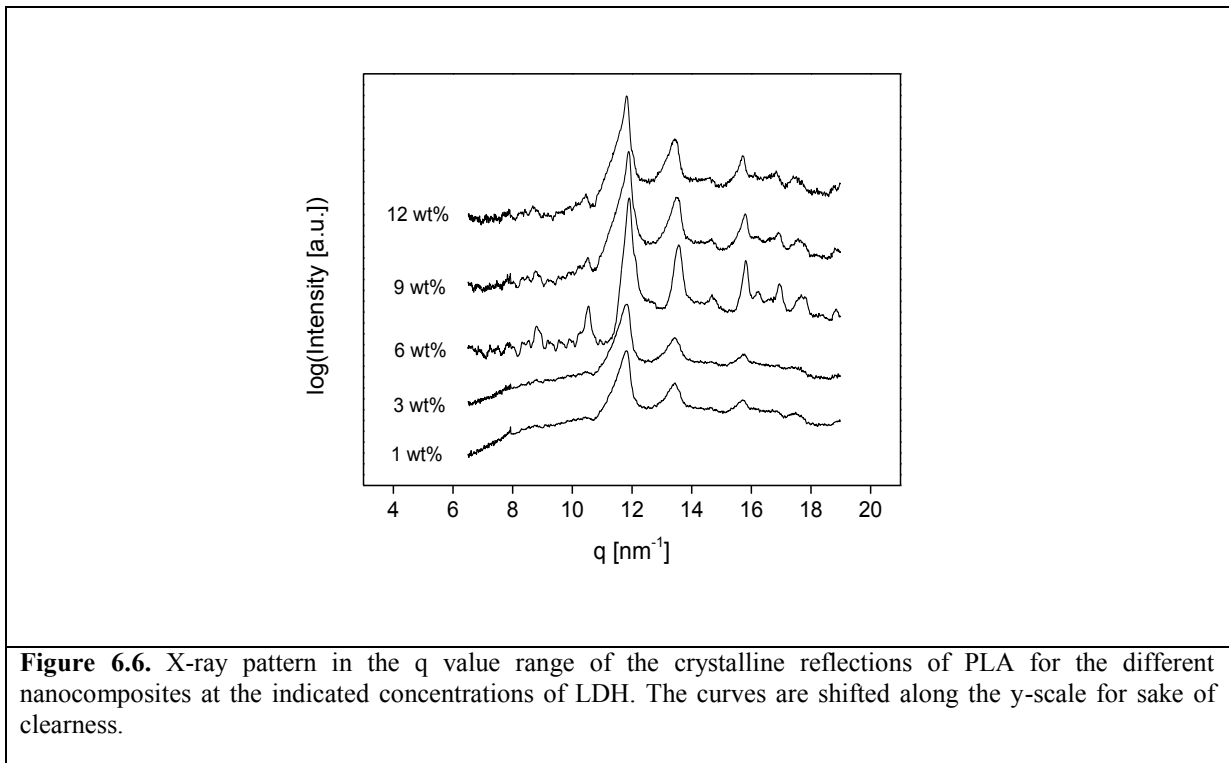
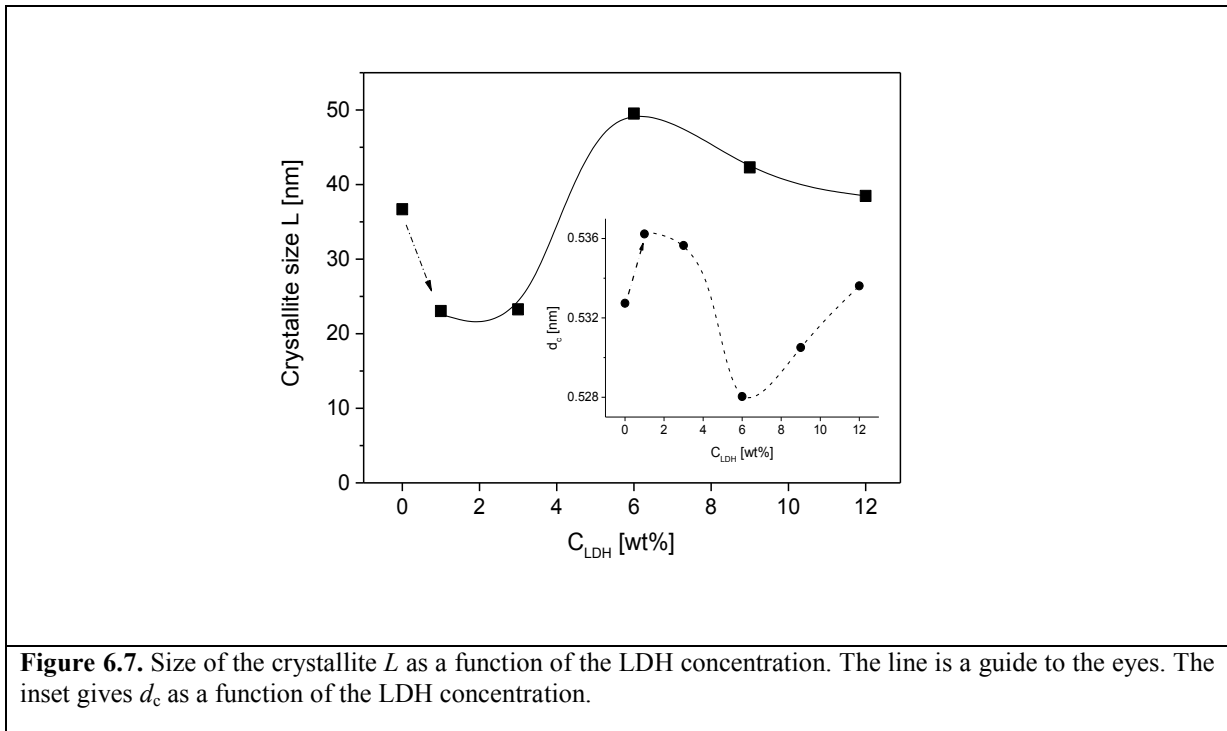


**Figure 6.6.** X-ray pattern in the  $q$  value range of the crystalline reflections of PLA for the different nanocomposites at the indicated concentrations of LDH. The curves are shifted along the y-scale for sake of clearness.

Unfortunately, absolute values of the degree of crystallinity cannot be estimated from the X-ray data because of the fact that the separation of the scattering contributions from crystalline and amorphous regions of the materials is ambiguous. The reason for this effect is not clear and needs further investigations.

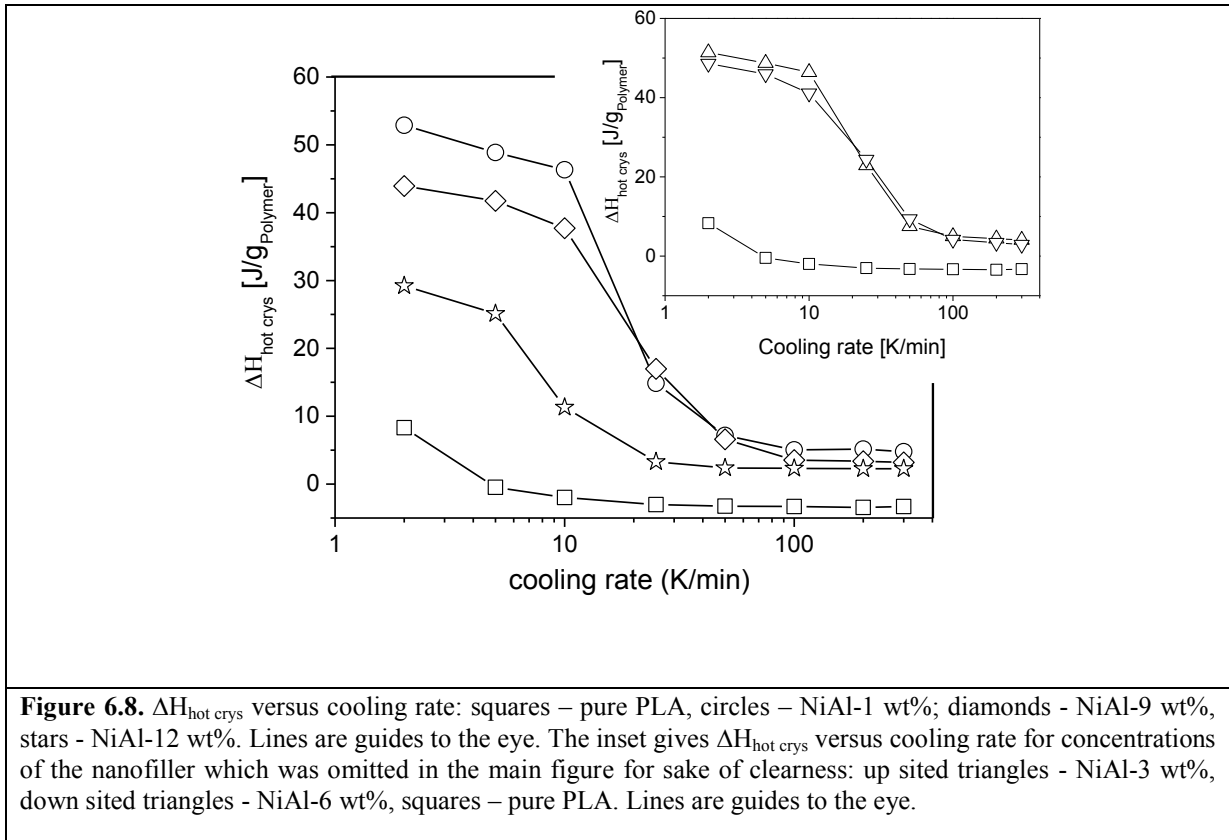
By the analysis of the width of the reflections, the crystal size  $L$  and the  $d_c$  spacing within a crystal can be estimated. The crystal size is plotted as a function of the concentration of LDH in Figure 6.7. Compared to pure PLA the crystal size decreases for  $C_{\text{LDH}}=1 \text{ wt}\%$ . Parallel, the  $d_c$  spacing increases (see inset of Figure 6.7). This results points to a less ordered structure of the crystals for low concentrations of the nanofiller. Because of the fact that the overall degree of crystallinity strongly increases, this means that for  $C_{\text{LDH}}=1 \text{ wt}\%$ , many imperfect crystals are formed compared to pure PLA. With increasing concentration of LDH, the crystal size increases and  $d_c$  decreases for concentrations of up to  $C_{\text{LDH}}=6 \text{ wt}\%$ . The high value of the degree of crystallinity observed for a concentration of 6 wt% of LDH is due to larger crystals with a higher order than in pure PLA. With a further increase of the LDH concentration, the crystal size decreases and the  $d_c$  increase indicates a loss of order.



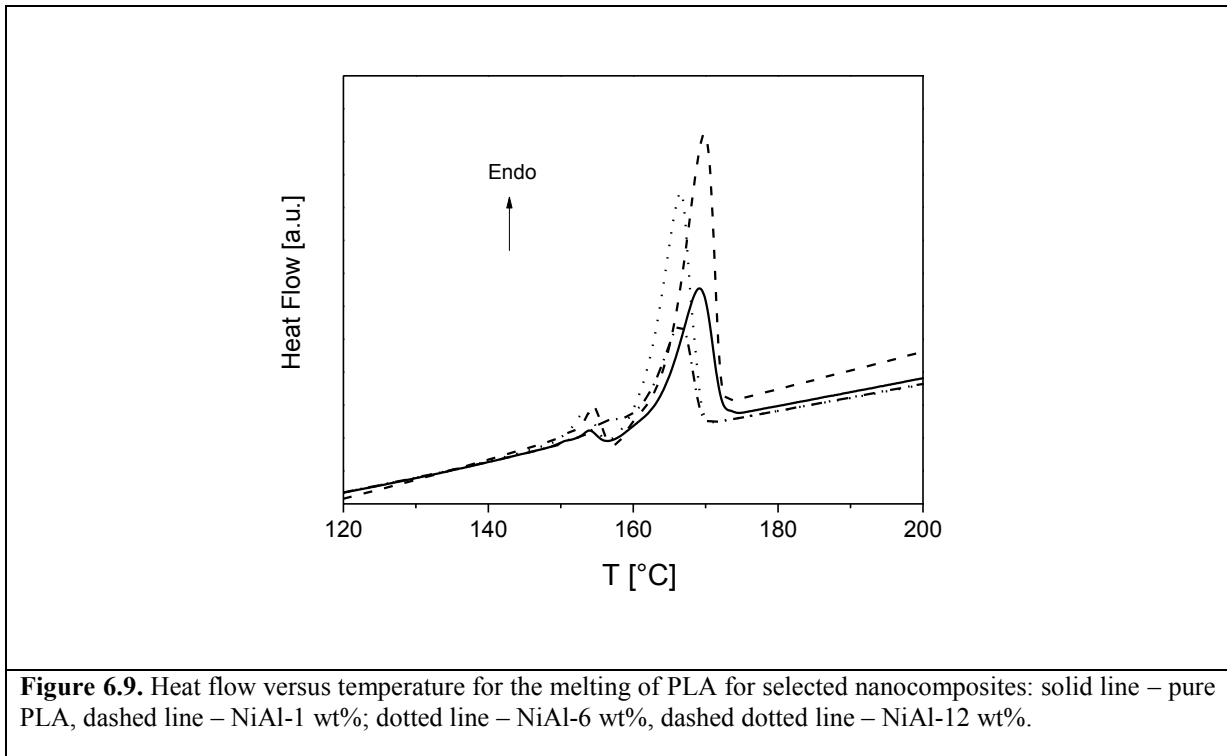
#### 6.4 The phase fraction analysis between NiAl/LDH-PLA and MgAl/LDH-PLA nanocomposites

The determination of the critical cooling rate follows the same procedure we applied on the investigation of MgAl/LDH-PLA nanocomposites (see Chapter 5). Therefore, here we do not give the detailed explanations again. Figure 6.8 shows the  $\Delta H_{hot\ crys}$  versus cooling rate for the selected concentrations of LDH nanofillers. (The inset of Figure 6.8 gives the data for the nanofiller concentrations which is omitted in the main figure for the sake of clearness). For pure PLA the  $\Delta H_{hot\ crys}$  data keeps accordance with the MgAl/LDH-PLA case. Compare to the similar plot from MgAl/LDH-PLA nanocomposites (see Figure 5.8), with the same concentrations, the value of  $\Delta H_{hot\ crys}$  of NiAl/LDH-PLA at higher cooling rates are apparently larger than that of the corresponding samples with MgAl/LDH. This indicates a higher degree of crystallization, in other words, the NiAl/LDH nanofiller has a stronger nucleating ability than the MgAl/LDH nanofiller. Through comparing the absolute value of  $\Delta H_{hot\ crys}$  with different NiAl/LDH concentrations at lower cooling rates (see Figure 6.8 and inset of Figure 6.8). The NiAl-1 wt% has the highest value of  $\Delta H_{hot\ crys}$ , and with the rise of NiAl/LDH concentration the  $\Delta H_{hot\ crys}$  decreases. This evidences the accumulation of content of NiAl/LDH nanofiller gives rise to a suppression effect to the degree of crystallization. Up to the cooling rate of 100 K/min, all  $\Delta H_{hot\ crys}$  of different concentrations approximates zero, indicating that crystallization during cooling is

suppressed completely. It should be noted that for some samples  $\Delta H_{\text{hot crys}}$  is not ideal zero as expected. This is due to uncertainties in the estimation of  $\Delta H_{\text{cold crys}}$  and  $\Delta H_{\text{melting}}$  which is in the range of ca.  $\pm 5$  J/g.



The 100 K/min was selected as the cooling rate to produce totally amorphous nanocomposite for the determination of  $RAF_{\text{filler}}$  via StepScan DSC techniques.



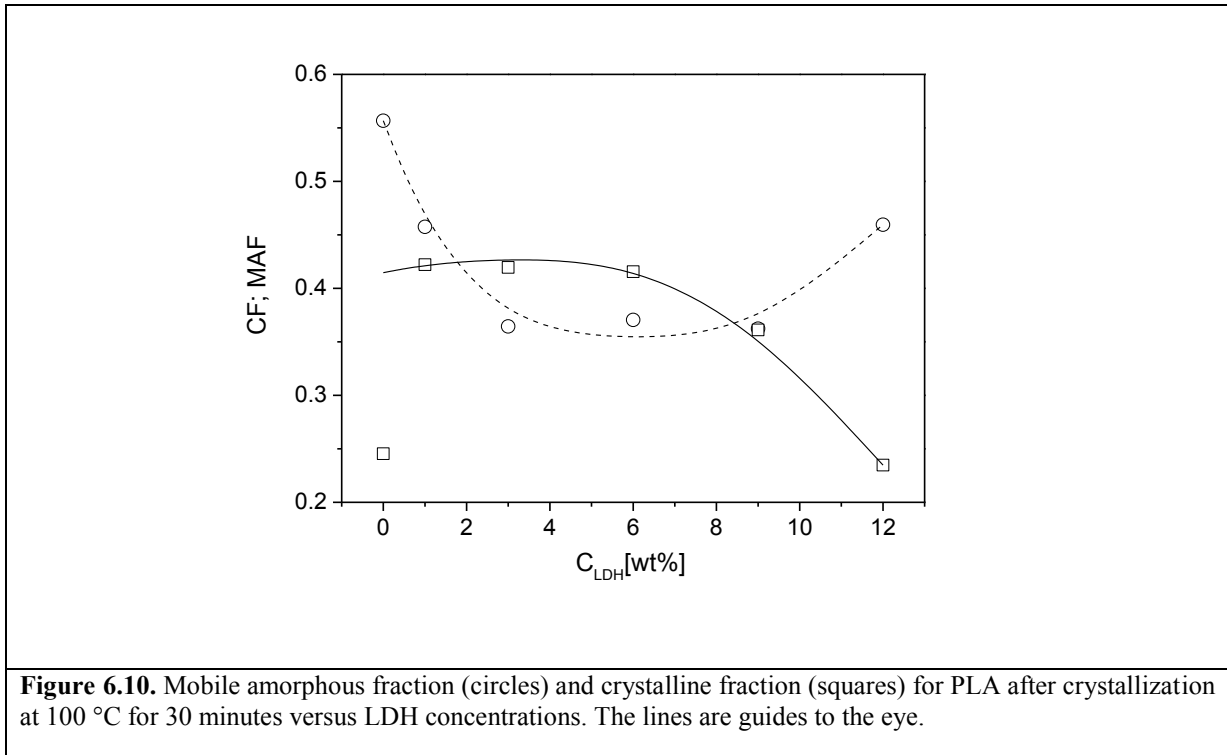
The crystalline fraction of NiAl/LDH-PLA nanocomposites was estimated by conventional DSC. The heat flow data during the melting of PLA for selected concentrations of NiAl/LDH nanofiller is given in Figure 6.9. The melting enthalpy increases more largely for lower concentrations of LDH compares to the pure PLA. As discussed above, the NiAl/LDH nanofiller act as a nucleating agent at low concentrations of LDH, with increasing content the degree of crystallization is suppressed (see Table 6.2). The melting enthalpy was estimated by integrating the corresponding peak in the heat flow and the crystalline fraction CF was obtained. For the measurement of MAF,  $RAF_{filler}$  and  $RAF_{crystal}$  the calculation procedure is as presented in Chapter 5. Here, Table 6.2 gives the resultant data directly, for the  $\Delta H_0$  a value of 93.7 J/g is taken<sup>220, 221</sup>.

Table 6.2. Sample codes, glass transition temperatures, thermodynamic quantities normalized to the weight of the polymer, and phase fractions calculated by Eqs 5.1-5.4

	Pure PLA	NiAl-1 wt%	NiAl-3 wt%	NiAl-6 wt%	NiAl-9 wt%	NiAl-12 wt%
$T_g$ (°C)	57.3	59.4	58.5	57.7	58.2	57.5
$\Delta H_{melting}$ (J/g <sub>Polymer</sub> )	23.0	39.5	39.3	38.9	33.8	22.0
$\Delta c_p$ (J/g <sub>Polymer</sub> *K)	0.27	0.23	0.18	0.18	0.18	0.23

$\Delta c_{p, \text{amorphousm}}$ (J/gPolymer*K)	0.49	0.49	0.47	0.47	0.46	0.41
MAF	0.56	0.46	0.36	0.37	0.36	0.46
CF	0.25	0.43	0.43	0.42	0.37	0.26
RAF <sub>filler</sub>	0	-0.014	0.032	0.037	0.066	0.17
RAF <sub>crystal</sub>	0.20	0.12	0.17	0.18	0.20	0.11

MAF and CF are plotted versus concentrations of NiAl/LDH in Figure 6.10. As mentioned in Chapter 5, for the pure PLLA the 30 min for crystallization at 100 °C exceeds the necessary crystallization time to obtain a full crystallized sample. Considering the accelerating crystallization rate of NiAl/LDH-PLA nanocomposites compared to pure PLLA, the resultant CFs can represent the maximal degree of crystallization in as prepared nanocomposites.



The dependence of CFs with increasing concentrations has the maximal value at the concentration of 6 wt%, this is in accordance with the trends of crystallinity measured in the second heating run. At higher concentrations the degree of crystallization is retarded by the increase of NiAl/LDH content furtherly. In parallel, MAF drops sharply on one hand due to the formation of rigid amorphous phase from nanofiller. On the other hand due to the increase of degree of crystallization and the emergence of corresponding

RAF<sub>crystal</sub>. Beyond the inflection concentration of 6 wt%, MAF increases again with the C<sub>LDH</sub> for the fall of CF partly.

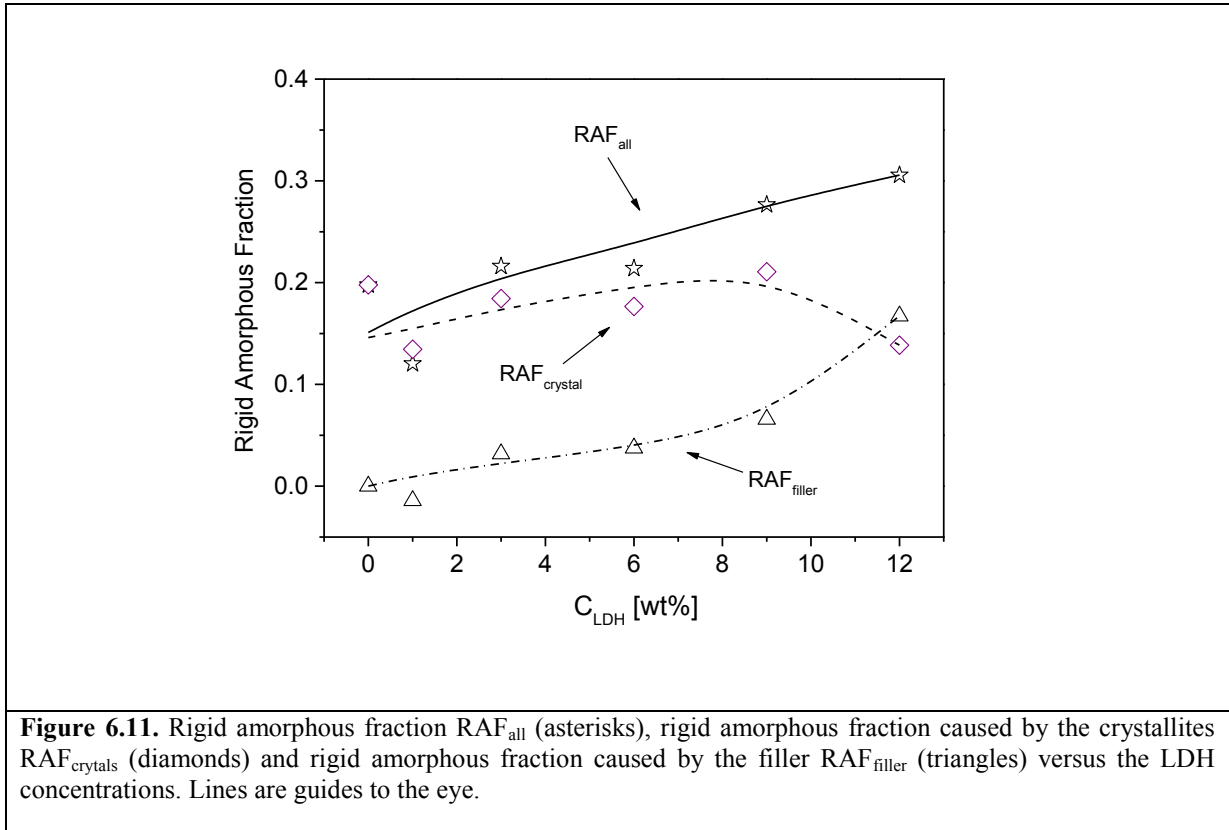
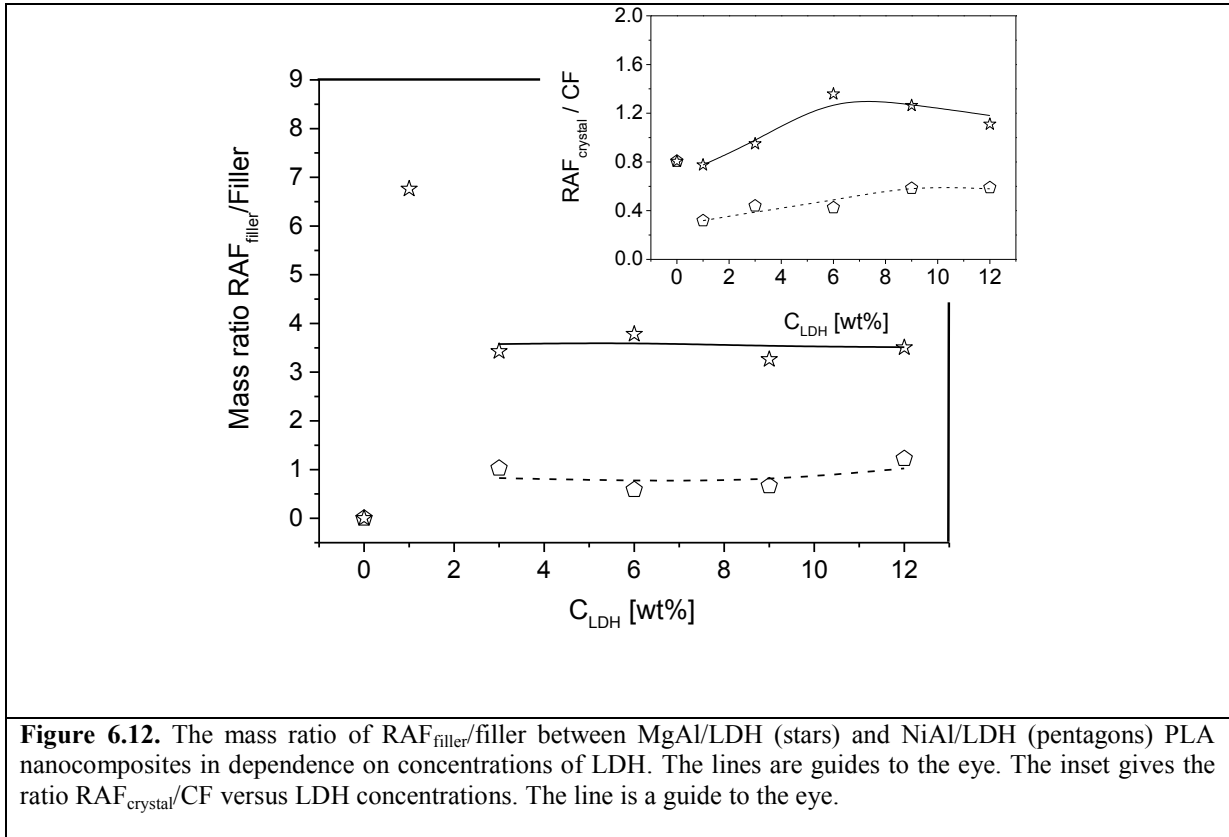


Figure 6.11 gives the trend of RAF versus the concentration of NiAl/LDH particles. Combining the RAF due to the nanofiller and the RAF resulted from the crystallization, the RAF<sub>all</sub> increases constantly with C<sub>LDH</sub>. The value of RAF<sub>filler</sub> due to NiAl/LDH is not comparable with the one of MgAl/LDH, for a more precise comparison, a dependence of ratio between the calculated mass of RAF and nanofiller with C<sub>LDH</sub> is made in Figure 6.12. Besides the intolerant error at the concentration of 1 wt%, the ratio from MgAl/LDH is around 3.5, and the ratio from NiAl/LDH indicates 0.8 approximately. This can be interpreted as the more contacting areas between polymer chains and nanofiller platelets for MgAl/LDH than NiAl/LDH. Relating the SAXS patterns and conductivity data to the different RAF<sub>filler</sub>/Filler ratios, it seems an another evidence for confirming the partly-exfoliated structure for MgAl/LDH-PLA nanocomposites, whereas the intercalated structure for NiAl/LDH-PLA nanocomposites. Another ratio related to RAF, the RAF<sub>crystal</sub>/CF is made in dependence on the increasing LDH content. A higher value of the ratio of MgAl/LDH-PLA is observed it is assumed for the more interference to

crystallization process because of the more fragments within nanocomposites due to the partly-exfoliated structure of MgAl/LDH-PLA.



**Figure 6.12.** The mass ratio of RAF<sub>filler</sub>/filler between MgAl/LDH (stars) and NiAl/LDH (pentagons) PLA nanocomposites in dependence on concentrations of LDH. The lines are guides to the eye. The inset gives the ratio RAF<sub>crystal</sub>/CF versus LDH concentrations. The line is a guide to the eye.

## 6.5 Dielectric Spectroscopy analysis for the NiAl/LDH-PLA nanocomposites

Besides literature studies (see for instance references [222-224]) the dielectric response of pure PLA is discussed in reference [5]. The dielectric response of polymer materials is related to the fluctuations of dipole moments that correspond to the functional groups and chain segments.<sup>87</sup> According to the literature, for bulk polylactide at least two main relaxation processes are observed as peaks of dielectric loss  $\epsilon''$  (see inset Figure 6.13). The  $\alpha$ -relaxation at temperatures above the thermal glass transition temperature  $T_g$  is attributed to the dynamic glass transition resulting from segmental fluctuations. The  $\beta$ -relaxation at lower temperature and higher frequency than the  $\alpha$ -relaxation is related to localized fluctuation.<sup>5</sup>

Figure 6.13 compares the dielectric loss in the temperature domain at a fixed frequency for pure PLA and different nanocomposites. Besides the  $\alpha$ - and the  $\beta$ -relaxation characteristic for bulk PLA three additional processes are observed for the

nanocomposites: (1) In the temperature range around 237 K an additional peak is observed (relaxation region 1). (2) A further process is also observed in the temperature around 310 K (relaxation region 2). (3) The  $\alpha$ -relaxation seems to broaden into a new peak (relaxation region 3). These features will be discussed below in the following sections.

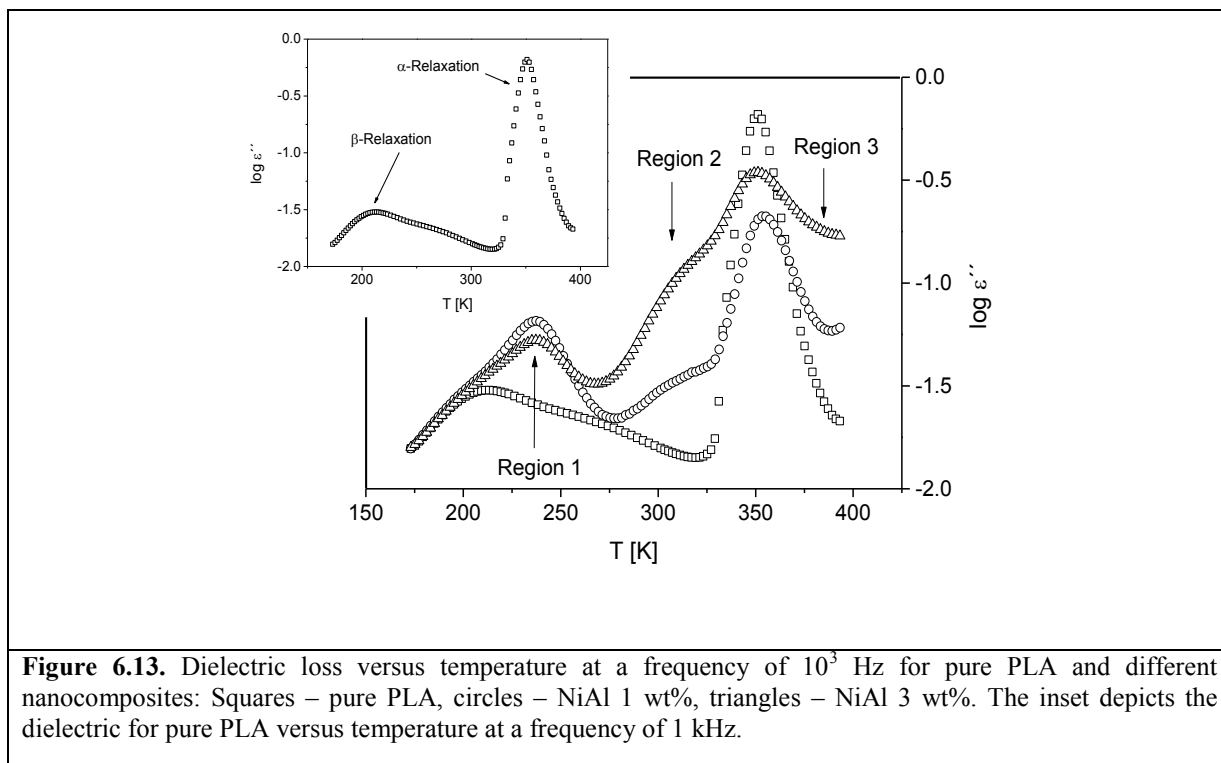
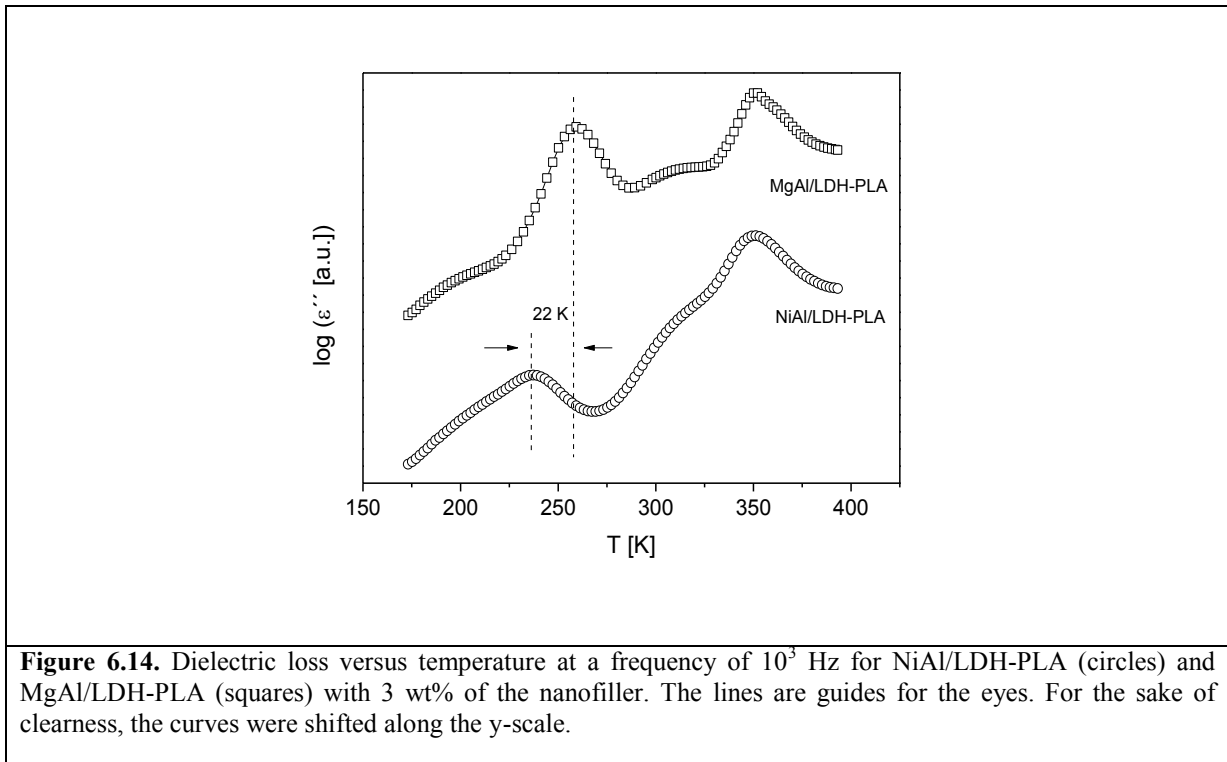


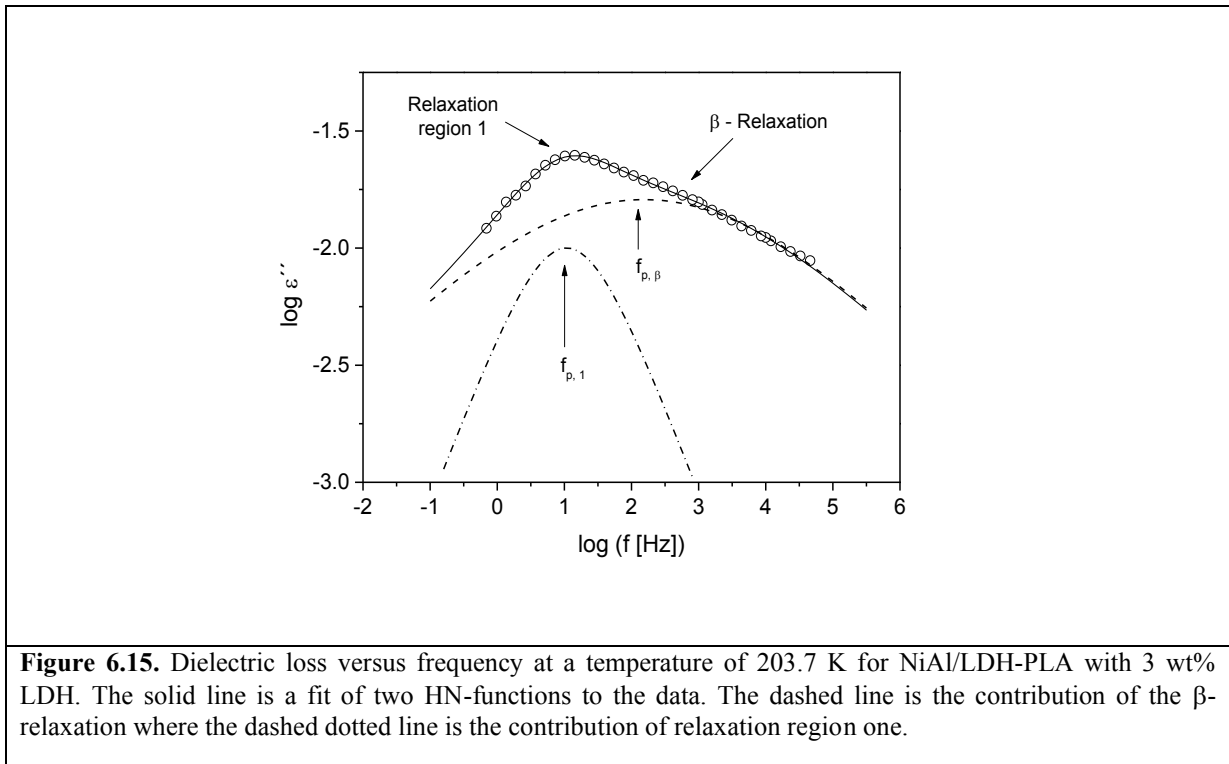
**Figure 6.13.** Dielectric loss versus temperature at a frequency of  $10^3$  Hz for pure PLA and different nanocomposites: Squares – pure PLA, circles – NiAl 1 wt%, triangles – NiAl 3 wt%. The inset depicts the dielectric for pure PLA versus temperature at a frequency of 1 kHz.

**Relaxation region 1:** For the MgAl/LDH-PLA nanocomposite system in the same temperature range also a relaxation process is observed, which increases in its intensity with increasing concentration of LDH.<sup>5</sup> Therefore, for this system, relaxation region 1 is assigned to SDBS molecules that form a mixed phase with the polymer segments in the interfacial region between the LDH layers and the polymeric matrix. This was also found for other nanocomposites based on different LDH fillers.<sup>45, 225, 226</sup> Figure 6.14 compares the dielectric loss for a MgAl and a NiAl/LDH-PLA nanocomposite with a concentration of 3 wt% of LDH. At the first glance, the observed behavior for the NiAl/LDH-PLA nanocomposites seems to be similar to that of the MgAl case.



Because of the fact that relaxation region 1 for the NiAl/LDH based nanocomposites is observed in a comparable temperature range as for the MgAl/LDH based materials, it is concluded that relaxation region 1 is also related to the fluctuations of the tails the SDBS together with PLA segments close to the filler for the NiAl/LDH based nanocomposites. However, a closer inspection of Figure 6.14 reveals pronounced differences with regard to the relaxation region 1 for both nanocomposite systems. For the NiAl/LDH based nanocomposite relaxation processes is shifted by more than 20 K to lower temperatures compared to the MgAl/LDH based nanocomposite and overlaps partly with the  $\beta$ -relaxation.

Before a detailed discussion, the data have to be analyzed in a quantitative manner. Hence, the model function of Havriliak/Negami (HN-function) is fitted to the data<sup>227</sup>, which was already depicted by Equation 3.39 in Section 3.3.2. From the fit of the HN-function to the data the relaxation rate  $f_p$  and the dielectric strength are determined and further discussed. If more as one relaxation process is observed in the covered frequency window a sum of HN-functions is fitted to the data. The method is described in detail in references [228,229]. An example for the fitting process is depicted in Figure 6.15.



In the inset of Figure 6.16, the relaxation rates for the  $\beta$ -relaxation and relaxation region 1 are plotted versus inverse temperature for NiAl/LDH-PLA nanocomposite with 3 wt% LDH. Obviously, both data sets can be described by the Arrhenius equation which was given for Equation 2.3 in Section 2.3.2. For the  $\beta$ -relaxation a value of 38 kJ/mol is obtained for the activation energy of the  $\beta$ -process. For the relaxation region 1 a significantly higher value of 53 kJ/mol is found. This proves that both processes are independent from each other.

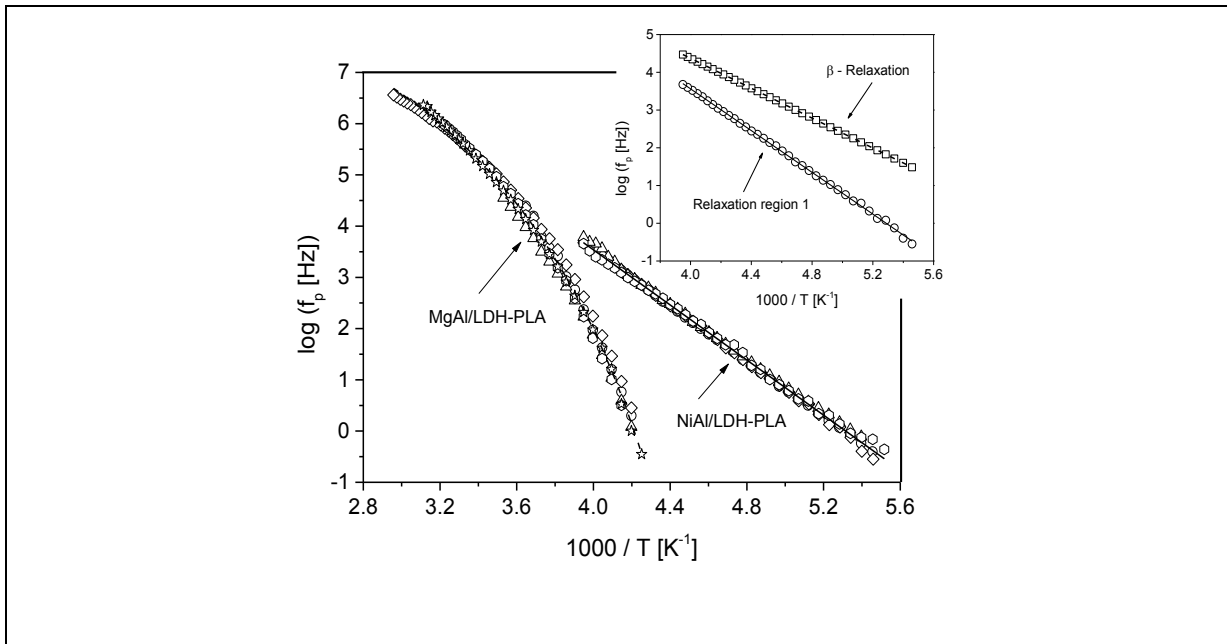
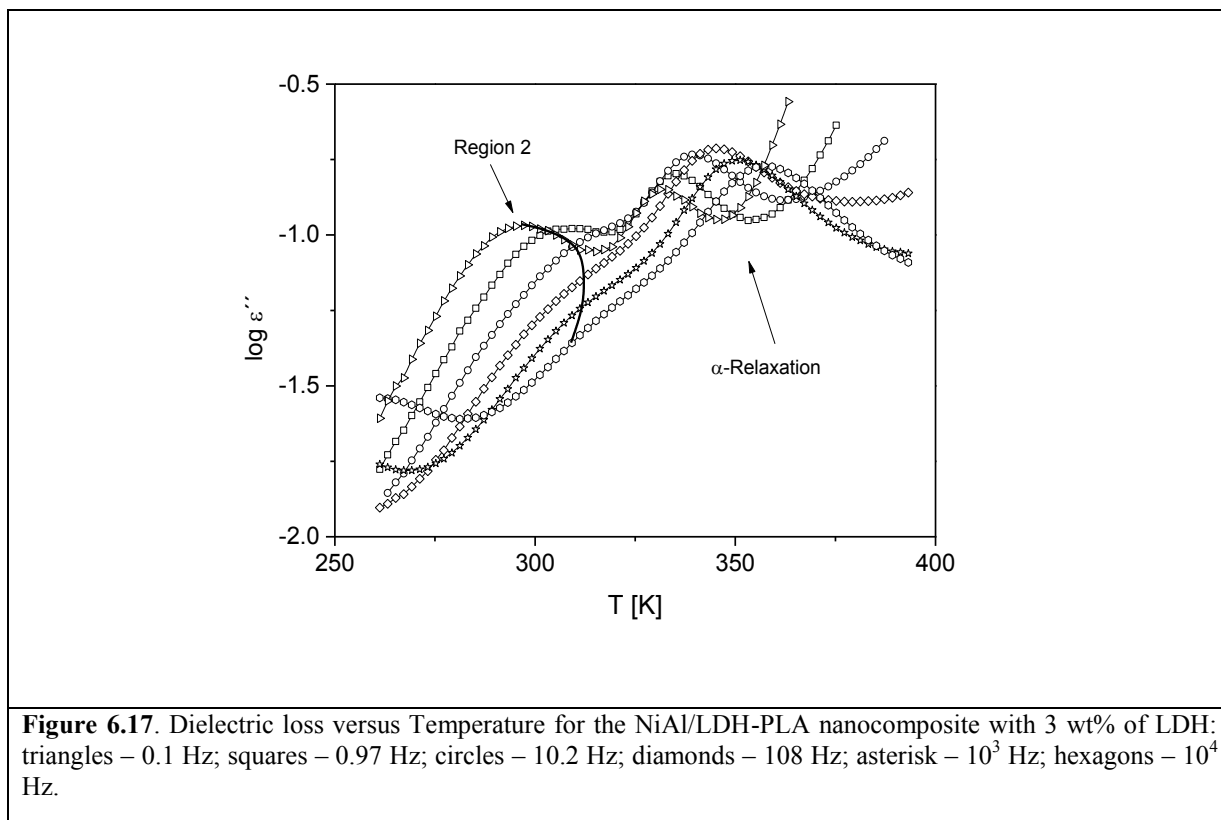


**Figure 6.16.** Relaxation rates of relaxation region 1 versus  $1000/T$  for NiAl/LDH and MgAl/LDH PLA nanocomposites as indicated: circle – 1 wt%, diamonds – 3 wt%, triangles – 6 wt%, hexagons – 9 wt%, stars – 12 wt%. The solid line is a common fit of the Arrhenius equation to all data sets of NiAl/LDH nanocomposites. The dashed line is a common fit of the VFT formula to all data of MgAl/LDH nanocomposites. The inset gives relaxation rates versus  $1000/T$  of relaxation region 1 and the  $\beta$ -relaxation for the NiAl/LDH based nanocomposite with 3 wt% LDH. Lines are fits of the Arrhenius equation to the corresponding data sets.

Figure 6.16 compares the temperature dependence of the relaxation rate of region one for NiAl/LDH and the MgAl/LDH-PLA based nanocomposites. For the NiAl based nanocomposites the data follows an Arrhenius behavior indicating a localized relaxation process, while for the MgAl-LDH/PLA the temperature dependences of the relaxation rate of region 1 has to be described by the Vogel/Fulcher/Tammann (VFT-) equation<sup>230, 231, 187</sup> (see Section 2.3.2), which is considered to be characteristic for a glassy behavior. The essential differences in the temperature dependence of the relaxation rate of process 1, found for both kinds of nanocomposites, indicate that the molecular motions due to the fluctuations of the SDBS tails together with the PLA segments are different: more localized fluctuations for the NiAl/LDH-PLA nanocomposites but cooperative, glassy-like dynamics for the material based on MgAl/LDH. Keeping in mind that the structure of the NiAl/LDH nanocomposite is more intercalated, one might conclude that relaxation region 1 is due to fluctuations of SDBS and PLA segments within the galleries of the layered LDH structure.

**Relaxation region 2:** The relaxation region 2 is observed for all concentrations of LDH and its intensity increases for higher concentrations of LDH (see Figure 6.13). For LDH concentrations higher than 6 wt%, this peak is strongly overlaid by the  $\alpha$ -relaxation and

conductivity effects. Figure 6.17 depicts the dielectric loss versus temperature for the NiAl/LDH-PLA nanocomposite with 3 wt% of LDH for different frequencies in the temperature range of relaxation region 2. As for the corresponding MgAl/LDH-PLA nanocomposite,<sup>5</sup> the temperature dependence of the peak position of relaxation region 2 is quite unusual. First, the peak shifts to higher temperatures with increasing frequency as expected. After passing a maximum temperature, the peak shifts back to lower temperatures



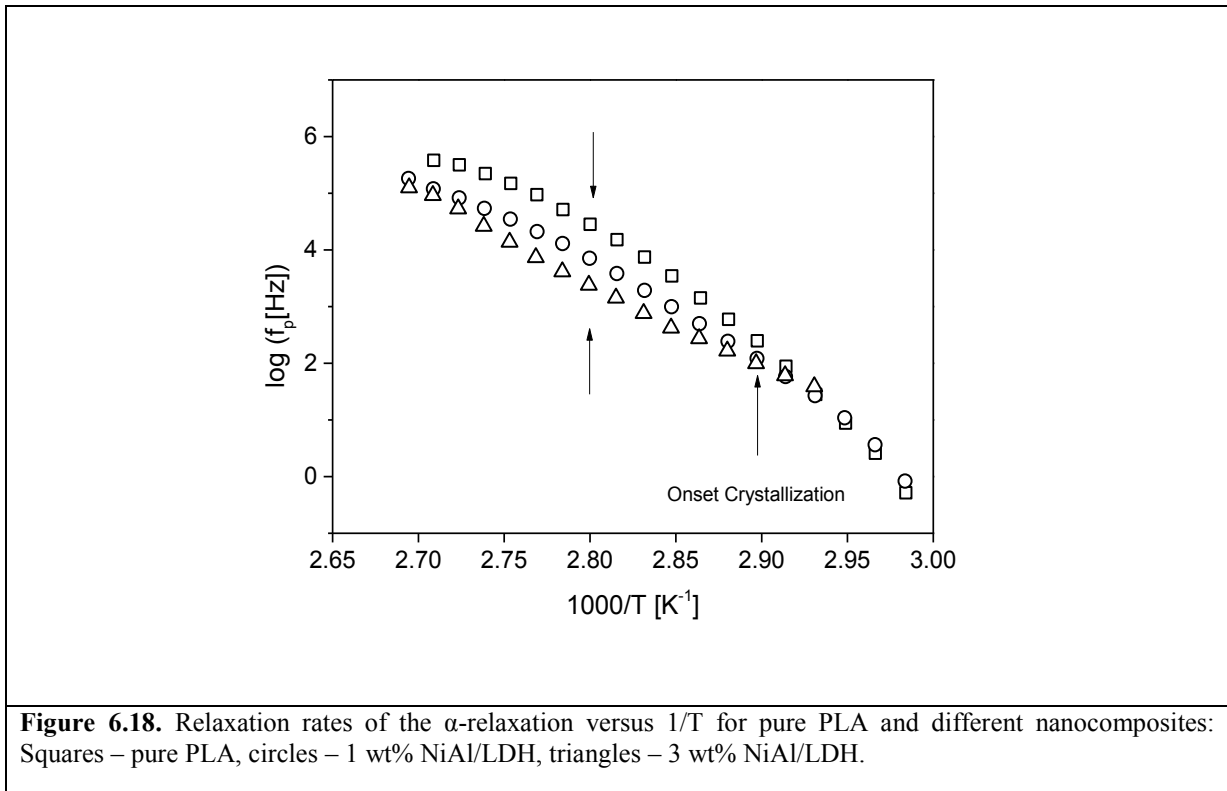
with further increase of the temperature. A similar saddle-like behavior was observed for nanocomposite systems based on a maleic anhydride grafted polypropylene and organophilic modified montmorillonite clay [40].

An analogous saddle-like behavior was also found for pure LDH materials, which was assigned in that case to the fluctuation of water molecules in a nanoporous environment [50]. Although the LDH materials are carefully dried before the preparation of the nanocomposites, water molecules might still be strongly adsorbed to the oxide surface. Therefore, relaxation region 2 is assigned to water present in the inter-galleries of the LDH. Such a saddle-like temperature dependence behavior can be described by the model of Ryabov et al.<sup>201</sup> This model assumes two competing effects. (1) The rotational fluctuation of water molecules should have an activated behavior described by the

Arrhenius equation. (2) The nanoporous structure due to the layers will provide some free volume defects that have a different temperature dependence. The combination of both effects will lead to a saddle-like temperature dependence which was observed for several nanoporous systems<sup>40, 50, 74, 78, 232</sup>. It seems to be therefore the fundamental behavior for water in nanoporous confining systems.

***$\alpha$ -Relaxation:*** Figure 6.18 depicts the relaxation rates for the  $\alpha$ -Relaxation. At low temperatures for all given concentrations the relaxation rates collapse into one chart together with data for neat PLA. This result indicates that this process due to the  $\alpha$ -Relaxation of polymeric matrix is not much influenced by the nanofiller. This is in agreement with the literature studies for other polymer based nanocomposites (see for instance [41-43, 206, 210] but also for other nanostructured systems like ultrathin films (see for instance [208-212])). With increasing temperature, the data deviate from the bulk behavior where the deviation is stronger for higher concentrations of the nanofiller. These deviations are due to the onset of crystallization with increasing temperature which is dependent on the concentration of the nanofiller. This behavior is similar to that of MgAl/LDH-PLA. For higher concentrations of LDH, the  $\alpha$ -relaxation is strongly overlaid by process 3 and conductivity phenomena and cannot be analyzed quantitatively.

***Relaxation region 3:*** For the analysis of the relaxation region 3 the modulus representation is used where the complex modulus  $M^*$  is related to the complex dielectric function by  $M^*(\omega)\varepsilon^*(\omega)=1$ <sup>80</sup>. The inset of Figure 6.19 compares the imaginary part of the complex electrical modulus  $M''$  for the nanocomposites MgAl/LDH and NiAl/LDH PLA for 9 wt% of the nanofiller at a temperature of 362.1 K. As discussed in Ref. 5, for MgAl/LDH-PLA the spectra show two peaks. The peak at lower frequencies is related to conductivity whereas the



peak at higher frequencies is related to interfacial polarization effects. These interfacial polarization effects are caused by mobile charge blocked at internal interphases having different values of the permittivity and/or conductivity (Maxwell/Wager/Sillars polarization). This interpretation is further supported by the strong increase of the real part of the dielectric function  $\epsilon'$  with decreasing frequency (see Figure 6.19). Such a strong increase of the  $\epsilon'$  is found to be typical for interfacial polarization and cannot be explained by a relaxation of a molecular dipole.

In the considered nanocomposite system with a semicrystalline polymer as a matrix, the MWS polarization can have two different origins: The blocking of charge carriers at the structures due to the nanofiller (exfoliated layers and intercalated nanostacks) and at the crystals. For pure PLA, the effects due to MWS polarization are insignificant in comparison to the nanocomposite. Therefore, it is concluded that the peak, which is located at higher frequencies of the loss part of the modulus is related to interfacial polarization effects due to the nanofiller.

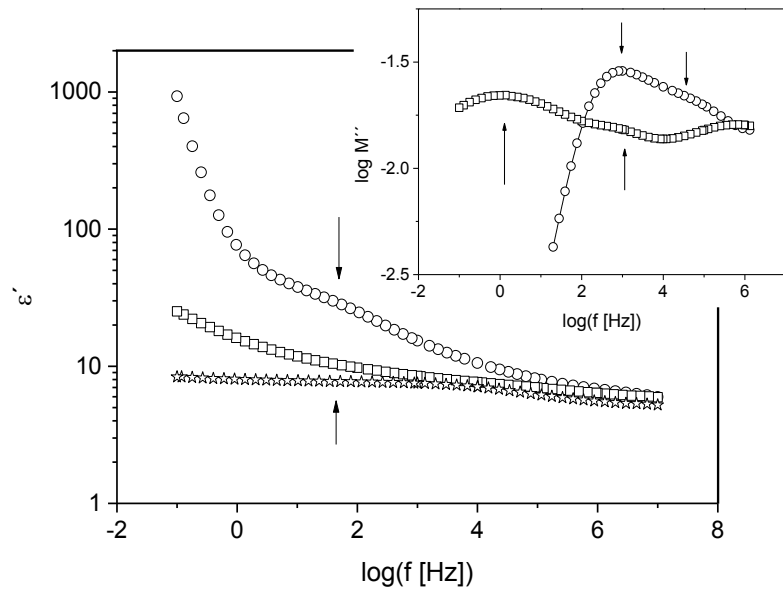


**Figure 6.19.** Real part of the complex dielectric function versus frequency for T=362.1 K: asterisks – pure PLA, squares – NiAl/LDH-PLA; circles – MgAl/LDH-PLA. The inset depicts the loss part  $M''$  versus frequency for T=362.1 K: squares – NiAl/LDH-PLA; circles – MgAl/LDH-PLA.

In the modulus representation, a conductivity contribution to dielectric loss is transformed in a peak. The peak at lower frequencies is therefore assigned to conductivity. This is further confirmed by a direct consideration of the conductivity, which is defined as  $\sigma^*(f) = 2\pi\epsilon_0 f \epsilon''(f)$  (see Figure 6.20).

For MgAl/LDH-PLA the real part of the complex conductivity  $\sigma'$  shows the typical frequency dependence expected for polymer systems. With decreasing frequency,  $\sigma'$  decreases with a power law. At a critical frequency  $f_c$ , this dependence turns into plateau which is the DC conductivity  $\sigma_{DC}$ . For MgAl/LDH-PLA, the DC conductivity  $\sigma_{DC}$  is at least

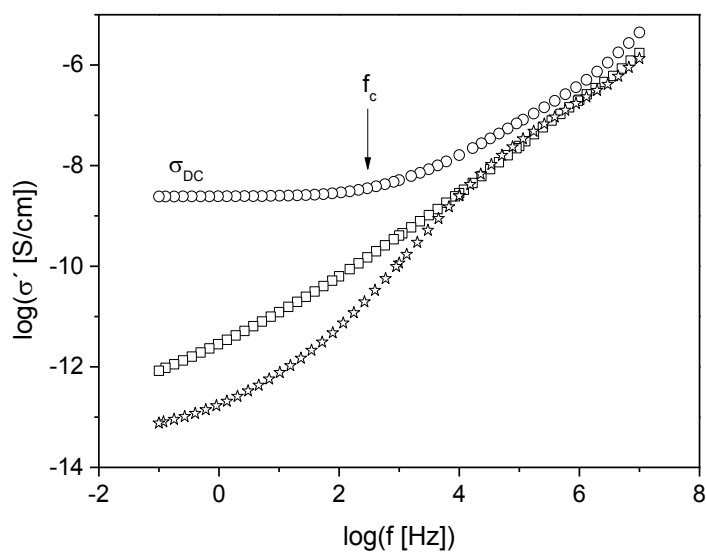


**Figure 6.20.** Real part of the complex conductivity versus frequency for  $T=362.1$  K: asterisks – pure PLA, squares – NiAl/LDH-PLA; circles – MgAl/LDH-PLA.

three orders of magnitude higher than for the NiAl/LDH based nanocomposite. This is also reflected on the modulus representation. The peak due to conductivity is shifted to lower frequencies. In addition, the peak related to interfacial polarization is observed at lower frequencies compared to MgAl/LDH-PLA (see inset Figure 6.19). Moreover, the contribution of the MWS polarization to the real part of complex dielectric function is much weaker than that of for MgAl/LDH-PLA. This different behavior must be due to differences in the structure of the both nanocomposites. As discussed above, the SAXS measurements reveal that the structure of the NiAl/LDH-PLA nanocomposite has a more intercalated structure than the MgAl/LDH based material which is more exfoliated. This leads to two consequences. Firstly, due to the presence of more exfoliated layers a larger amount of interfaces exist in the material at which charge carriers can be blocked. This larger amount of interfaces causes a larger Maxwell/Wagner/Sillars polarization compared to a corresponding intercalated system as observed. Secondly, due to the exfoliation process, ions, which are located in the interlayer galleries, can be released in to the matrix polymer. These additional charge carriers will increase the conductivity in comparison to a material were the nanofiller is not exfoliated. Also this effect is observed experimentally.

## Chapter 7 Conclusions and outlook

Poly(L-lactide) (PLA) nanocomposites based on organically modified MgAl layered double hydroxides (MgAl-LDH) and NiAl layered double hydroxides (NiAl-LDH) were both prepared by melt blending. The investigation of two kinds of PLA nanocomposites were applied by complementary measurements such as size exclusion chromatography (SEC), differential scanning calorimetry (DSC), small- and wide-angle X-ray scattering (SAXS and WAXS) and dielectric relaxation spectroscopy (BDS).

For the SEC measurements, both nanocomposites showed a small enhancement of the degradation of PLA due to the LDH nanoparticles. The NiAl/LDH-PLA nanocomposite was found a slightly stronger degradation than the MgAl/LDH-PLA nanocomposite. This behavior might be attributed to the different properties of the Ni and Mg ions.

The SAXS measurement also demonstrated the difference of properties between Mg and Ni ions. The gallery distance of original MgAl/LDH is 0.39 nm, whereas gallery distance of original NiAl/LDH is 0.27 nm. Both LDHs were observed to be modified successfully by SDBS. But the gallery distance of MgAl/LDH was increased to 2.53 nm, whereas for NiAl/LDH which was increased to 2.44 nm. Based on the determination of stack size, the average layer number for modified MgAl/LDH was calculated to be ca. 6, the NiAl/LDH was observed averagely had 3.76 layers. These results indicated that the NiAl/LDH-PLA nanocomposites had a more intercalated structure in comparison to the MgAl/LDH-PLA nanocomposites. Meanwhile, the MgAl/LDH-PLA nanocomposites had a partly exfoliated morphology with mixed nanostacks.

The thermal properties of the nanocomposites were investigated by conventional DSC. The degree of crystallization of the MgAl/LDH-PLA nanocomposites was found reduced with increasing LDH concentration for the concentration greater than 1 wt%. While in the NiAl/LDH system, the crystallinity increased until the LDH content of 6 wt% where a decreasing trend started with increasing LDH concentration. For both nanocomposites the crystallization degree trend observed from WAXS measurements was similar to the DSC result.

The phase fractions are characterized by a deliberately designed calorimetric program for both nanocomposites. The CFs value of MgAl/LDH-PLA nanocomposites keeps decreasing for the LDH content exceeding 1 wt%. Whereas for NiAl/LDH-PLA system, the CFs value reaches maxima at the concentration of 6 wt%, at higher concentration the CF decreases because of the confinement resulting from the LDH. For the MAFs value,

MgAl/LDH-PLA nanocomposite displays a decreasing trend. In contrast, the MAFs of NiAl/LDH-PLA system achieves minima at the same concentration of 6 wt% with its CFs. The behavior of MAFs should be attributed to the interaction of both the CFs and RAFs. The RAF is divided into  $RAF_{\text{filler}}$  and  $RAF_{\text{crystal}}$  for both nanocomposites systems. To offer a more clarified comprehension, the mass ratios of  $RAF_{\text{filler}}/\text{Filler}$  and  $RAF_{\text{crystal}}/\text{CF}$  are plotted respectively versus the LDH concentration. Both types of  $RAF_{\text{filler}}/\text{Filler}$  ratios show a constant value, for MgAl/LDH is 3.5 and the value of NiAl/LDH equals 0.8. A larger contacting area between polymer chains and nanofiller platelets for MgAl/LDH than NiAl/LDH can be concluded. Meanwhile, the data from SAXS patterns and conductivity both point to a more exfoliated structure for MgAl/LDH-PLA nanocomposites, these results link together to prove a partly-exfoliated structure for MgAl/LDH-PLA and a intercalated structure for NiAl/LDH-PLA. On the basis of analysis of the  $RAF_{\text{crystal}}/\text{CF}$  ratio, a higher value for MgAl/LDH-PLA is observed, it is deduced the partly-exfoliated structure of MgAl/LDH-PLA produces more nanofiller fragments within nanocomposites to interfere the crystallization process of PLA.

The dielectric relaxation behavior of neat PLA show a  $\beta$ -relaxation due to localized fluctuations below the thermal glass transition temperature  $T_g$  and an  $\alpha$ -relaxation due to segmental dynamics (dynamic glass transition) for temperatures higher than  $T_g$ . Besides these relaxation processes the relaxation behavior of the MgAl/LDH-PLA nanocomposites is more complex and at least three additional dielectric relaxation regions are observed. The relaxation region 1 is related to the interfacial area between the nanofiller and the PLA matrix. It is mainly due to the the fluctuations of the alkyl tails of the SDBS molecules together with PLA segments. The temperature dependence of the relaxation rate of relaxation region 2 seems to have an unusual saddle-like temperature dependence. It is related to the fluctuations of remaining water molecules in the nonporous structure of the LDH nanofillers. Relaxation region 3 is observed at temperatures higher than characteristic for the dynamic glass transition. It is assigned to interfacial polarizations effects due to the blocking of charge carriers at the nanofiller.

The relaxation behavior of the NiAl/LDH-PLA nanocomposite is analogous to the MgAl/LDH-PLA case, also three additional dielectric relaxation regions are observed. Relaxation region 1 is mainly related to the fluctuations of SDBS surfactants intercalating between the layers of NiAl/LDH. The temperature dependence of the corresponding relaxation rates obeys an Arrhenius law which is in difference to the MgAl/LDH case.

This indicates different surfactant molecular presence situations in the two systems. The temperature dependence of the relaxation rate of relaxation region 2 also has an unusual saddle-like temperature dependence which is related to the relaxation of water molecules in nanoporous environment. Relaxation region 3 is assigned to the interfacial polarizations effects due to the blocking of charge carriers at the nanofiller, which is a Maxwell/Wagner/Sillars polarization effect. This effect on the MgAl/LDH-PLA nanocomposite is stronger than on the NiAl/LDH-PLA nanocomposite. Furthermore, the conductivity value is found lower for the NiAl/LDH-PLA nanocomposite than the MgAl/LDH-PLA nanocomposite. These can be interpreted by more charge carriers of LDH platelets in MgAl/LDH-PLA system, and it is due to the more exfoliated structure of MgAl/LDH-PLA nanocomposite and more intercalated structure of NiAl/LDH-PLA nanocomposite.

The LDH nanofiller based PLA nanocomposites is only one case for the clay based polymer nanocomposites. Even at a low loading, these nanocomposites exhibits remarkably better mechanical, thermal, dynamic mechanical, adhesion and barrier properties, flame retardancy, etc. in comparison to the corresponding neat polymer material. However, the selection of the combination of polymer and clays is essentially at random, rather than by a scientific principle (at least no such process was reported).<sup>233</sup> The in-depth understanding of the structure-property relationship of high performance polymer nanocomposites is in need with eagerness. And the clays chosen are usually limited in the smectite group because of their well exfoliation property. Therefore, expanding boundary of the feasible clays might present new promising functional nanocomposites. The development of innovative polymer nanocomposites is possible to involve either novel combination of nanofiller and polymer matrix, or any breakthroughs in strategy of the synthetic process. The recent report<sup>234</sup> on synthetic nacre by an artificial approach is no doubt a great inspiration for the fabrication of biomimetic polymer nanocomposites.



## Reference

---

- 1 Peeterbroeck, S.; Alexandre, M.; Dubois, P. *Processing of Polymer Nanocomposites: New Developments and Challenges* In: *Recent Advances in Polymer Nanocomposites: Synthesis and Characterisation* Taylor & Francis Group, **2010**, p. 19.
- 2 Zhang, Z.; Friedrich, K. *Compos. Sci. Technol.*, **2003**, *63*, 2029-2044.
- 3 Paul, D. R.; Robeson, L. M. *Polymer* **2008**, *49*, 3187.
- 4 Vaia, R. A.; Giannelis, E. P. *MRS Bull.* **2001**, *26*, 394.
- 5 Leng, J.; Purohit, P. J.; Kang, N.-J.; Wang, D.-Y.; Falkenhagen, J.; Emmerling, F.; Thünemann, A. F.; Schönhals, A. *Eur. Polym. J.* **2015**, *68*, 338-354.
- 6 Balazs, A. C.; Emrick, T.; Russell, T. P. *Science* **2006**, *314*(5802), 1107-1110
- 7 Kotal, M.; Bhowmick, A. K. *Progr Polym Sci* **2015**, *51*, 127-187.
- 8 Hsueh, H. B.; Chen, C. Y. *Polymer* **2003**, *44*, 1151-1161.
- 9 Costa, F. R.; Satapathy, B. K.; Wagenknecht, U.; Weidisch, R.; Heinrich, G. *Eur. Polym. J.* **2006**, *42*, 2140-2152.
- 10 Chen, W.; Qu, B. *Chem. Mater.* **2003**, *15*, 3208-3213.
- 11 Qiu, L.; Chen, W.; Qu, B. *Polymer* **2006**, *47*, 922-930.
- 12 Wang, Q.; O'Hare, D. *Chem. Rev.* **2012**, *112*, 4124.
- 13 Costa, F. R.; Saphiannikova, M.; Wagenknecht, U.; Heinrich, G. *Adv. Polym. Sci.* **2008**, *210*, 101.
- 14 Catti, M.; Ferraris, G.; Hull, S.; Pavese, A. *Phys. Chem. Miner.* **1995**, *22*, 200.
- 15 Williams, G. R.; Dunbar, T. G.; Beer, A. J.; Fogg, A. M.; O'Hare, D. *J. Mater. Chem.* **2006**, *16*, 1222.
- 16 Williams, G. R.; O'Hare, D. *J. Mater. Chem.* **2006**, *16*, 3065.
- 17 Selvam, T.; Inayat, A.; Schwieger, W. *Dalton Trans.* **2014**, *43*, 10365.
- 18 Corma, A. *Chemical Reviews* **1997**, *97*, 6.
- 19 Abello, S.; Medina, F.; Tichit, D.; Pe' rez-Rami' rez, J.; Cesteros, Y.; Salagre, P.; Sueiras, J. E. *Chem. Commun.* **2005**, 1453-1455.
- 20 Velasco, J. I.; Ardanuy, M.; Antunes, M. *Layered double hydroxides (LDHs) as functional fillers in polymer nanocomposites* In: *Advances in polymer nanocomposites: types and applications*; Gao, F.-G., Eds.; Woodhead Publishing Limited, **2012**; p 91.
- 21 Pinnavaia, T. J.; Beall, G. W. *Polymer-clay nanocomposites*, England, John Wiley & Sons.

- 
- 22 Sorrentino, A.; Gorasi, G.; Tortora, M.; Vittoria, V.; Constantino, U. *et al. Polymer* **2005**, *46*, 1601–1608.
- 23 Kotal, M.; Kuila, T.; Srivastava, S. K.; Bhowmick, A. K.; *J. Appl. Polym. Sci.* **2009**, *114*, 2691–2699.
- 24 Pavlidoua, S.; Papaspyrides, C. D. *Progr. Polym. Sci.* **2008**, *33*, 1119 – 1198 .
- 25 Du, L.; Qu, B. *Polym. Compos.* **2007**, 131–138 .
- 26 Herrero, M.; Benito, P.; Labajos, F. M.; Rives, V.; Zhu, Y. D. *et al. J. Solid State Chem.* **2010**, *183*, 1645–1651 .
- 27 Lu, P.; Liang, S.; Liu, L.; Gao, Y.S.; Wang, Q. *J. Membrane Sci.* **2016**, *504*, 196-205.
- 28 Kapusetti, G.; Misra, N.; Singh, V. *et al. J. Biomed. Mater. Res. Part A* **2012**, *100A*, 3363-3373.
- 29 Mahkam, M.; Davatgar, M.; Rezvani, Z.; Nejati, K. *International J. Polymeric Materials* **2011**, *62*, 57-60.
- 30 Sperling, L. H. *Introduction to physical polymer science*; John Wiley & Sons: New Jersey, **2005**.
- 31 Katz, D.; Zervi, I. G. *J. Polym. Sci.* **1974**, *46C*, 139.
- 32 Katz, D.; Salee, G. *J. Polym. Sci.* **1968**, *A-2 (6)*, 801.
- 33 Ueberreiter, K.; Kanig, G. *J. Chem. Phys.* **1950**, *18*, 399.
- 34 Martin, G. M.; Mandelkern, L. *J. Res. Natl. Bur. Stand.* **1959**, *62*, 141.
- 35 Schönhals, A.; Kremer, F. *Amorphous polymers* In: *Polymer Science: A comprehensive reference, Volume 1*, Matyjaszewski, K.; Möller, M. Eds., Elsevier Inc., **2013**, p. 201.
- 36 Ehrenfest, P. *Leiden Comm. Suppl.* **1933**, *75a*.
- 37 Prigogine, I.; Defay, R. *Chemical Thermodynamics*; Longmanns-Green: New York, **1954**.
- 38 Donth, E. *The Glass Transition: Relaxation Dynamics in Liquids and Disordered Materials*; Springer: Berlin, Germany, **2001**.
- 39 Moynihan, C. T. *Ann. N.Y. Acad. Sci.* **1981**, *371*, 151.
- 40 Gupta, P. K.; Moynihan, C. T. *J. Chem. Phys.* **1976**, *65*, 4136.
- 41 Struick, L. G. E. *Physical aging in amorphous polymers and other materials*; Elsevier Science Publisher Co.: Amsterdam, Oxford, New York, **1978**.
- 42 Kauzmann, W. *Chem. Rev.* **1948**, *43*, 219.
- 43 Adam, G.; Gibbs, J. H. *J. Chem. Phys.* **1965**, *43*, 139.

- 
- 44 Kirkpatrick, T. R.; Thirumalai, D.; Wolynes, P. G. *Phys. Rev. A* **1989**, *40*, 1045.
- 45 Bailey, R. T.; North, A. M.; Pethrick, R. A. *Molecular motion in high Polymers*; Oxford University Press: Oxford, New York, **1981**.
- 46 Alig, I.; Stieber, F.; Bakhramov, A.D. et al. *Polymer* **1989**, *30*, 842.
- 47 Berne, B.J.; Pecora, R. *Dynamic Light Scattering*; Wiley: New York, **1976**.
- 48 Fytas, G.; Ngai, K. L. *Macromolecules* **1988**, *21*, 804
- 49 Roe, R. J. *Methods of X-ray and Neutron Scattering in Polymer Science*; Oxford University Press: Oxford, New York, **2000**.
- 50 Schmidt-Rohr, K.; Spiess, H. W. *Multidimensional Solid-State NMR and Polymers*; Academic press: London, **1994**.
- 51 Spiess, H. W. *Macromolecules* **2010**, *43*, 5479.
- 52 Birge, N. O.; Nagel, S. R. *Phys. Rev. Lett.* **1985**, *54*, 2674.
- 53 Schick, C. *Temperature Modulated Differential Scanning Calorimetry – Basics and applications to Polymers* In: *Handbook of Thermal Analysis and calorimetry Vol. 3*; Cheng, S. Z. D., Eds.; Elsevier, Amsterdam, **2002**; p 713.
- 54 Huth, H.; Minakov, A.; Schick, C. *J. Polym. Sci. B Polym. Phys.* **2006**, *44*, 2996.
- 55 Kremer, F.; Schönhals, A., Eds. *Broadband Dielectric Spectroscopy*; Springer: Berlin, Germany, **2002**.
- 56 Vogel, H. *Physikalische Zeitschrift* **1921**, *22*, 645.
- 57 Fulcher, G. S. *J. Am. Ceram. Soc.* **1925**, *8*, 339.
- 58 Tammann, G.; Hesse, W. *Z. Anorg. Allg. Chem.* **1926**, *156*, 245.
- 59 Angell, C. A. *J. Non-Cryst. Solids* **1991**, *13*, 131.
- 60 Angell, C. A. *J. Res. Natl. Inst. Stand. Technol.* **1997**, *102*, 171.
- 61 Ferry, J. D. *Viscoelastic properties of polymers*, 3rd ed.; Wiley: New York, **1980**.
- 62 Arbe, A.; Richter, D.; Colmenero, J. et al. *Phys. Rev. E* **1996**, *54*, 3853
- 63 Hofmann, A.; Kremer, F.; Fischer, E. W.; Schönhals, A. *The scaling of the  $\alpha$ - and  $\beta$ -relaxation in low molecular weight and polymeric glass forming systems* In: *Disorder Effects on Relaxational Processes*; Richert, R. Blumen, A., Eds.; Springer Verlag: Berlin, Germany, **1994**; Chapter 10, p 309.
- 64 Schönhals, A. In: *Nonequilibrium Phenomena in Supercooled Fluids, Glasses and Amorphous Materials*; Giordano, M. Leporini, D. Tosi, M. P., Eds.; World Scientific Publishing Co.:Singapore, **1996**, ISBN 981-02-2795-7.

- 
- 65 Johari, G. P.; Goldstein, M. *J. Chem. Phys.* **1970**, *53*, 2372.
- 66 Johari, G. P. In: *The Glass Transition and the Nature of the Glassy state*; Goldstein, M. Simha, R. Eds.; *Ann. N. Y. Acad. Sci.* **1976**, *279*, 117.
- 67 Zallen, R. *The Physics of Amorphous Solids*; Wiley: New York, **1983**.
- 68 Fox, T. G.; Flory, P. J. *J. Appl. Phys.* **1950**, *21*, 581.
- 69 Doolittle, A. K. *J. Appl. Phys.* **1951**, *22*, 1471.
- 70 Cohen, M. H.; Turnbull, D. *J. Chem. Phys.* **1959**, *31*, 1164.
- 71 Cohen, M. H.; Grest, G. S. *Phys. Rev. B* **1979**, *20*, 1077.
- 72 Shrader, D. M.; Jean, Y. C. *Positron and Positronium Chemistry*; Elsevier: Amsterdam, The Netherlands, **1988**.
- 73 Dlubek, G.; Clarke, A. P.; Fretwell, H. M. et al. *Phys. Status Solid A* **1996**, *157*, 351.
- 74 Dlubek, G. In: *Encyclopedia of Polymer Science and Technology*; Seidel, A., Eds.; Wiley-Interscience: Hoboken, NJ, 2008; p 1-23.
- 75 Yampolskii, Y. P.; Kaliuzhnyi, N. E.; Durgaryan, S. G. *Macromolecules* **1986**, *19*, 846.
- 76 Donth, E. J. *J. Non-cryst. Solids* **1982**, *53*, 325.
- 77 Golemme, G.; Nagy, J. B.; Fonseca, J. B. A. et al. *Polymer* **2003**, *44*, 5039.
- 78 Adam, G.; Gibbs, J. H. *J. Chem. Phys.* **1965**, *43*, 139.
- 79 Schneider, K.; Schönhals, A.; Donth, E. J. *Acta Polymerica* **1981**, *32*, 471.
- 80 Hempel, E.; Hempel, G.; Hensel, A.; et al. *J. Phys. Chem. B* **2000**, *104*, 2460.
- 81 Beiner, M.; Kahle, S.; Hempel, E.; et al. *Macromolecules* **1998**, *31*, 2460.
- 82 Kahle, S.; Korus, J.; Hempel, E.; et al. *Macromolecules* **1997**, *30*, 7214.
- 83 Cheng, S. Z. D.; Jin, S. *Crystallization and melting of metastable crystalline polymers in Handbook of Thermal Analysis and calorimetry Vol. 3*; Cheng, S. Z. D., Eds.; Elsevier, Amsterdam, **2002**.
- 84 Cheng, S. Z. D.; Keller, A. *Annu. Rev. Mater. Sci.* **1998**, *28*, 533.
- 85 Cheng, S. Z. D.; Keller, A. *Polymer* **1998**, *39*, 4461.
- 86 Wunderlich, B. *Macromolecular Physics, Vol. III, Crystal Melting*, Academic Press, New York, **2001**.
- 87 Schönhals, A. *Molecular Dynamics in Polymer Model Systems* In: *Broadband Dielectric Spectroscopy*; Kremer, F.; Schönhals, A., Eds.; Springer: Berlin, **2002**; p 225.
- 88 Strobl, G. *The physics of polymers: concepts for understanding their structures and behavior*; Springer, Berlin, **1996**.

- 
- 89 Ishida, Y.; Yamafuji, K.; Ito, H.; Takayanagi, M. *Kolloid Z. Z. Polym.* **1962**, *184*, 97.
- 90 Huo, P.; Cebe, P. *Macromolecules* **1992**, *25*, 902.
- 91 Nogales, K.; Ezquerra, T. A.; et al. *Macromolecules* **1999**, *32*, 2301.
- 92 Schick, C.; Dobbertin, J.; et al. *J. Therm. Anal.* **1997**, *49*, 499.
- 93 Gabrielse, W.; Gaur, H. A.; et al. *Macromolecules* **1994**, *27*, 5811.
- 94 Wunderlich, B. *Prog. Polym. Sci.* **2003**, *28*, 383-450.
- 95 Menczel, J.; Wunderlich, B. *J. Polym. Sci. Polym. Lett. Ed.* **1981**, *19*, 261-264.
- 96 Suzuki, H.; Grebowicz, J.; Wunderlich, B. *Br. Polym. J.* **1985**, *17*, 1-3.
- 97 Schick, C.; Wurm, A.; Mohammed, A. *Thermochim. Acta* **2003**, *396*, 119.
- 98 Righetti, M. C.; Tombari, E. *Thermochim. Acta* **2010**, *522*, 118-127.
- 99 Righetti, M. C.; Laus, M.; Di Lorenzo, M. L. *European Polymer Journal* **2014**, *58*, 60-68.
- 100 Sargsyan, A.; Tonoyan, A.; et al. *European Polymer Journal* **2007**, *43*, 3113-3127.
- 101 Leng, J.; Kang, N. J.; Wang, D.-Y.; et al. *Polymer* **submitted**.
- 102 Wunderlich, B. *Thermal analysis*; Academic Press, New York, **1990**.
- 103 Hemminger, W.; Höhne, G. W. H. *Calorimetry – fundamentals and practice*. VCH, Weinheim, **1984**.
- 104 Wunderlich, B. *Thermal analysis* In: *Encyclopedia of materials science and engineering*; Bever, M. B., Eds.; Pergamon Press, Oxford. **1986**.
- 105 Richardson, M. *Thermal analysis* In: *Comprehensive polymer science, vol 1*; Allen, G. Eds.; Pergamon Press, Oxford. **1989**.
- 106 Höhne, G. W. H.; Hemminger, W.; Flammersheim, H.-J. *Differential Scanning Calorimetry*; Springer-Verlag Berlin Heidelberg. **2003**.
- 107 Schick, C. *Anal. Bioanal. Chem.* **2009**, *395*, 1589-1611.
- 108 LeParlouer, P.; Mathonat, C. (2005) Proceedings 33rd NATAS, Universal City, CA, USA.
- 109 Watson, E. S.; O'Neill, M. O.; Justin, J. Brenner, N. *Anal. Chem.* **1964**, *36*, 1233-1238.
- 110 O'Neill, M. J. *Anal. Chem.* **1964**, *36*, 1238-1245.
- 111 Reading, M.; Elliott, D.; Hill, V. *Proceedings of the 21st North American Thermal Analysis Society Conference* **1992**, 145-150.
- 112 Reading, M.; Elliott, D.; Hill, V. *J. Therm. Anal.* **1993**, *40*, 949.

- 
- 113 Sindee, L. S. *Thermochim. Acta* **2001**, 374, 55-71.
- 114 Reading, M.; Hourston, D. J. *Modulated-Temperature Differential Scanning Calorimetry — theoretical and practical applications in polymer characterisation*; Springer, **2006**.
- 115 Reading, M.; Luget, A.; Wilson, R. *Thermochim. Acta* **1994**, 238, 295.
- 116 Reading, M. J. *J. Therm. Anal. Calor.* **1997**, 54, 411.
- 117 Schawe, J. E. K. *Thermochim. Acta* **1995**, 260, 1.
- 118 Schick, C. *Temperature modulated differential scanning calorimetry (TMDSC)-basics and applications to polymers* In: *Handbook of Thermal Analysis and calorimetry Vol. 3*; Cheng, S. Z. D., Eds.; Elsevier, Amsterdam, **2002**.
- 119 Sichina, W. J. *Better characterization of thermosets using stepscan DSC*
- 120 Pielichowski, K.; Flejtuch, K.; Pielichowski, Jan. *Polymer* **2004**, 45, 1235-1242.
- 121 Sandor, M.; Bailey, N. A.; Mathiowitz, E. *Polymer* **2002**, 43, 279.
- 122 Höhne, G. W. H. ; Hemminger, W.; Flammersheim, H.-J. *Differential Scanning Calorimetry*, Springer-Verlag Berlin Heidelberg. **2003**.
- 123 Spilotros, A.; Svergun, D. I. *Advances in Small- and Wide-Angle X-ray Scattering SAXS and WAXS of Proteins* In: *Encyclopedia of analytical chemistry*; Meyers, R. A., Eds. John Wiley & Sons, Ltd. **2000**.
- 124 Chu, B.; Hsiao, B. S. *Chem. Rev.* **2001**, 101, 1727.
- 125 Sawyer, L. C.; Grubb, D. T.; Meyers, G. F. *Polymer Microscopy*. Springer **2007**.
- 126 Alexander, L. E. *X-ray Diffraction Methods in Polymer Science*, John Wiley & Sons, New York. **1969**.
- 127 Romhany, G.; Vigh, J.; Thomann, R.; Karger-Kocsis, J.; Sajo, I. E. *Macromol. Mater. Eng.* **2013**, 296, 544.
- 128 Ruland, W. *Colloid Polym. Sci.* **1977**, 255, 417.
- 129 Vonk, C. G.; Kortleve, G. *Colloid Polym. Sci* **1967**, 220, 19.
- 130 Strobl, G. R.; Schneider, M. J. *Polym. Sc. Polym. Phys. Ed.* **1980**, 18, 1343.
- 131 Causin, V.; Marega, C.; et al. *Polymer* **2005**, 46, 9533-9537.
- 132 Smilgies, D. M. *J. Appl. Cryst.* **2009**, 42, 1030.
- 133 Böttcher, C. J. F. *Theory of electric polarization, vol. I. Dielectrics in static fields*. Elsevier Amsterdam, Oxford, New York. **1973**.
- 134 Debye, P. *Polar molecules*. Chemical catalog, reprinted by Dover 1929

- 
- 135 Kirkwood, J. G. *J. Chem. Phys.* **1939**, 58, 911.
- 136 Kirkwood, J. G. *Ann. NY Acad. Sci.* **1940**, 40, 315.
- 137 Kirkwood, J. G. *Trans. Faraday* **1946**, 42A, 7.
- 138 Fröhlich, H. *Theory of dielectrics*. Oxford University Press, London. **1958**.
- 139 Böttcher, C. J. F.; Bordewijk, P. *Theory of electric polarization, vol. II. Dielectrics in time-dependent fields*. Elsevier Amsterdam, Oxford, New York. **1980**.
- 140 Landau, L. D. Lifschitz, E. M. *Textbook of theoretical physics, vol. V. Statistical physics*. Akademie-Verlag, Berlin. **1979**.
- 141 Cole, K. S.; Cole, R. H. *J. Chem. Phys.* **1941**, 9, 341.
- 142 Davidson, D. W.; Cole, R. H. *J. Chem. Phys.* **1950**, 18, 1417.
- 143 Davidson, D. W.; Cole, R. H. *J. Chem. Phys.* **1951**, 19, 1484.
- 144 Havriliak, S.; Negami, S. *J. Polym Sci. C.* **1966**, 16, 99.
- 145 Havriliak, S.; Negami, S. *Polymer* **1967**, 8, 161.
- 146 Wagner, R. W. *Arch. Elektrotech* **1914**, 2, 371.
- 147 Sillar, R. W. *J. Inst. Elect. Eng.* **1937**, 80, 378.
- 148 Richert, R. *Tutorial on "Broadband Dielectric Spectroscopy and its Application"* **2005**.
- 149 Sherman, P. *Emulsion science*. Academic Press, New York. **1968**.
- 150 Takashima, S. *Electrical properties of biopolymers and membranes*. Institute of Physics Publishing. **1989**.
- 151 Samet, M.; Serghei, A. et al. *J. Chem. Phys.* **2015**, 142, 194703.
- 152 Wang, D. Y.; Costa, F. R.; Vyalikh, A.; Leuteritz, A.; Scheler, U.; Jehnichen, D.; Wagenknecht, U.; Häussler, L.; Heinrich, G. *Chem. Mater.* **2009**, 21, 4490.
- 153 Purohit, P. J.; Huacuja-Sánchez, J. E.; Wang, D. Y.; Emmerling, F.; Thünemann, A.; Heinrich, G.; Schönhals, A. *Macromolecules* **2011**, 44, 4342.
- 154 Purohit, P. J.; Wang, D. Y.; Emmerling, F.; Thünemann, A. F.; Heinrich, G.; Schönhals, A. *Polymer* **2012**, 53, 2245.
- 155 Paris, O.; Li, C.; Siegel, S.; Weseloh, G.; Emmerling, F.; Riesemeier, H.; Erko, A.; Fratzl, P. *J. Appl. Crystallogr.* **2007**, 40, S466.
- 156 Hammersley, A. P.; Svensson, S. O.; Hanfland, M.; Fitch, A. N.; Hausermann, D. *High Pressure Res.* **1996**, 14, 235.

- 
- 157 Sarge, S. M.; Hemminger, W.; Gmelin, E.; Höhne, G. W. H.; Cammenga, H. K.; Eysel, W. *J. Therm. Anal.* **1997**, *49*, 1125–34.
- 158 Najafi, N.; Heuzey, M. C.; Carreau, P. J. *Polym. Eng. Sci.* **2013**, *53*, 1053-1064.
- 159 Wu, D.-F.; Wu, L.; Wu, L.-F.; Xu, B.; Zhang, Y.-S.; Zhang, M. *J. Polym. Sci. Pol. Phys.* **2007**, *45*, 1100-1113.
- 160 Toda, A.; Androsch, R.; Schick, C. *Polymer* **2016**, *91*, 239-263.
- 161 Kremer, F.; Schönhals, A. *Broadband Dielectric Measurement Techniques In: Broadband Dielectric Spectroscopy*; Kremer, F.; Schönhals, A., Eds.; Springer: Berlin, Germany, **2002**, p. 35.
- 162 Burum, D.P.; Rhim, W. K. *J. Chem. Phys.* **1979**, *71*, 944.
- 163 Chiang, M.-F.; Chu, M.-Z.; Wu, T.-M. *Polym. Degrad. Stab.* **2011**, *96*, 60-66.
- 164 Pilla, S.; Gong, S.; O'Neill, E.; Yang, L.; Rowell, R. M. *J. Appl. Polym. Sci.* **2009**, *111*, 37.
- 165 Fischer, E. W.; Sterzel, H. J.; Wegner, G. *Kolloid-Z. u. Z. Polymere* **1973**, *251*, 980-990.
- 166 Stoclet, G.; Seguela, R.; Lefèbvre, J. M.; Elkoun, S.; Vanmansart C. *Macromolecules* **2010**, *43*, 1488-1498.
- 167 Delpouve, N.; Delbreilh, L.; Stoclet, G.; Saiter, A.; Dargent, E. *Macromolecules* **2014**, *47*, 5186-5197.
- 168 Cao, X.; Mohamed, A.; Gordon, S. H.; Willett, J. L.; Sessa, D. *J. Thermochimica Acta* **2003**, *406*, 115–127.
- 169 Sargsyan, A.; Tonoyan, A.; Davtyan, S.; Schick, C. *Eur. Polym. J.* **2007**, *43*, 3113.
- 170 Wunderlich, B. *Pure. Appl. Chem.* **1995**, *67*, 1019.
- 171 Schlosser, E.; Schönhals, A. *Colloid Polym. Sci.* **1989**, *267*, 963.
- 172 Schick, C. *Anal. Bioanal. Chem.* **2009**, *395*, 1589-1611.
- 173 Wurm, A.; Ismail, M.; Kretzschmar, B.; Pospiech, D.; Schick, C. *Macromolecules* **2010**, *43*, 1480-1487.
- 174 Schawe, E. K. *J. Appl. Polym. Sci.* **2015**, *133*, 42977
- 175 Tsuji, H.; Ikada, Y. *Polymer* **1995**, *36*, 2709–2716.
- 176 Tsuji, H.; Ikada, Y. *Polymer* **1996**, *37*, 595–601.
- 177 Wurm, A.; Merzlyakov, M.; Schick, C. *J. Therm. Anal. Calorim.* **2000**, *60*, 807.
- 178 Schick, C.; Wurm, A.; Mohammed, A. *Thermochim Acta* **2002**, *392-393*, 303.

- 
- 179 Androsch, R.; Wunderlich, B.; Radusch, H. J. *J. Therm. Anal. Calorim.* **2005**, *79*, 615.
- 180 Androsch, R.; Wunderlich, B. *Macromolecules* **2001**, *34*, 5950.
- 181 Pan, P.; Inoue, Y. *Prog. Polym. Sci.* **2009**, *34*, 605-640.
- 182 Righetti, C. M.; Gazzano, M.; Lorenzo, D. L. M.; Androsch, R. *Eur. Polym. J.* **2015**, *70*, 215-220.
- 183 Xiao, H.-W.; Liu, F.; Jiang, T.; Yeh, J.-T. *J. Appl. Polym. Sci.* **2010**, *117*, 2980-2992.
- 184 Starkweather, Jr. H. W.; Avakian, P. *Macromolecules*, **1993**, *26*, 5084.
- 185 Mierzwa, M.; Floudas, G.; Dorgan, J.; Knauss, D.; Wegner, J. *J. Non-Cryst. Solids* **2002**, *307-310*, 296-303.
- 186 Bras, A. R.; Viciosa, M. T.; Wang, Y.-M.; Dionisio, M.; Mano, J. F. *Macromolecules* **2006**, *39*, 6513-6520.
- 187 Havriliak, S.; Negami, S. *J. Polym. Sci. Part C: Polym. Symposia* **1966**, *14*, 99-117.
- 188 Vogel, H. *Physikalische Zeitschrift* **1921**, *22*, 645.
- 189 Fulcher, G. S. *J. Am. Chem. Soc.* **1925**, *8*, 339-355.
- 190 Tammann, G.; Hesse, W. *Z. Anorg. Allg. Chem.* **1926**, *156*, 245.
- 191 Jacobs, J.D.; Koerner, H.; Heinz, H.; Farmer, B. L.; Mirau, P.; Garrett, P. H.; Vaia, R. A. *J. Phys. Chem. B* **2006**, *110*, 20143.
- 192 Kubies, D.; Jérôme, R.; Grandjean, J. *Langmuir* **2002**, *18*, 6159.
- 193 Heinz, H.; Suter, U. W. *J. Phys. Chem. B* **2004**, *108*, 18341-18352.
- 194 Kremer, F.; Schönhals, A. *The Scaling of the Dynamics of Glasses and Supercooled Liquids Spectra* In: *Broadband Dielectric Spectroscopy*, Kremer, F.; Schönhals, A. Eds.; Springer: Berlin, **2002**; p 99.
- 195 Donth, E. *J. Non-Cryst. Solids* **1982**, *53*, 325.
- 196 Hempel, E.; Hempel, G.; Hensel, A.; Schick, C.; Donth, E. *J. Phys. Chem. B* **2000**, *104*, 2460.
- 197 Sills, S.; Gray, T.; Overney, R.M., *J. Chem. Phys.* **2005**, *123*, 134902.
- 198 Berthier, L.; Biroli, G.; Bouchaud, J.P.; Cipelletti, L.; El Masri, D.; L'Hôte, D.; Ladieu, F.; Pierno, M. *Science* **2005**, *310*, 1797.
- 199 Cangialosi, D.; Alegria, A.; Colmenero, J. *Phys. Rev. E* **2007**, *76*, 011514.
- 200 Saiter, A.; Delbreilh, L.; Couderc, H.; Arabeche, K.; Schönhals, A.; Saiter, J.-M. *Phys. Rev. E* **2010**, *81*, 041805.

- 
- 201 Frunza, L.; Schönhals, A.; Frunza, S.; Parvulescu, V.I.; Cojocaru, B. Carriazo, D.; Martín, C.; Rives, V. *J. Phys. Chem. A* **2007**, *111*, 5166.
- 202 Ryabov, Y.E.; Puzenko, A.; Feldman, Yu. *Phys. Rev. B* **2004**, *69*, 014204.
- 203 Frunza, L.; Kosslick, H.; Frunza, S.; Schönhals, A. *J. Phys. Chem. B* **2002**, *106*, 9191.
- 204 Ryabov, Ya.; Gutina, A.; Arkhipov, V.; Feldman, Yu. *J. Phys. Chem. B* **2001**, *105*, 1845
- 205 Schönhals, A.; Kremer F. *Theory of Dielectric Relaxation In: Broadband Dielectric Spectroscopy*; Kremer, F.; Schönhals, A., Eds.; Springer: Berlin, **2002**; p 1.
- 206 Holt, A.; Griffin, P.; Bocharova, V.; Agapov, A.; Imel, A.; Dadmun, M.; Sangoro, J.; Sokolov, A. *Macromolecules* **2014**, *47*, 1837–1843.
- 207 Füllbrandt, M.; Purohit, P.; Schönhals, A. *Macromolecules* **2013**, *46*, 4626-4632.
- 208 Huth, H.; Minakov, A.; Schick, C. *J. Polym. Sci. B: Polym. Phys.* **2006**, *44*, 2996-3005.
- 209 Zhou, D.S.; Huth, H.; Gao, Y.; Xue, G.; Schick, C. *Macromolecules* **2008**, *41*, 7662-7666.
- 210 Tress, M.; Erber, M.; Mapesa, E. U.; Huth, H.; Müller, J.; Serghei, A.; Schick, C.; Eichhorn, K.-J.; Volt, B.; Kremer, F. *Macromolecules* **2010**, *43*, 9937–9944.
- 211 Yin, H.; Schönhals, A. *Soft Matter* **2012**, *8*, 9132-9139.
- 212 Yin, H.; Schönhals, A. *Polymer* **2013**, *54*, 2067-2070.
- 213 Chiang, M.-F.; Chu, M.-Z.; Wu, T.-M. *Polym. Degrad. Stab.* **2011**, *96*, 60-66.
- 214 Södergard, A.; Stolt, M. *Prog. Polym. Sci.* **2002**, *27*, 1123-1163.
- 215 Delpouve, N.; Delbreilh, L.; Stoclet, G.; Saiter, A.; Dargent, E. *Macromolecules* **2014**, *47*, 5186-5197.
- 216 Lee, J. H.; Jeong, Y. G. *Fiber Polym.* **2011**, *12*, 180-189.
- 217 Xu, H.-S.; Dai, X. J.; Lamb, P. R.; Li, Z.-M. *J. Polym. Sci. B Polym. Phys.* **2009**, *47* 2341-2352.
- 218 Tsuji, H.; Taki, H.; Saha, S. K. *Polymer* **2006**, *47*, 3826-3837.
- 219 Pluta, M. *Polymer* **2004**, *45*, 8239-8251.
- 220 Tsuji, H.; Ikada, Y. *Polymer* **1995**, *36*, 2709–2716.
- 221 Tsuji, H.; Ikada, Y. *Polymer* **1996**, *37*, 595–601.
- 222 Starkweather, Jr. H.W.; Avakian, P. *Macromolecules* **1993**, *26*, 5084.

- 
- 223 Mierzwa, M.; Floudas, G.; Dorgan, J.; Knauss, D.; Wegner, J. *J. Non-Cryst. Solids* **2002**, *307-310*, 296-303.
- 224 Bras, A. R.; Viciosa, M. T.; Wang, Y.-M.; Dionisio, M.; Mano, J. F. *Macromolecules* **2006**, *39*, 6513-6520.
- 225 Purohit, P. J.; Huacuja-Sanchez, J. E.; Wang, D.-Y.; Emmerling, F.; Thünemann, A.; Heinrich, G.; Schönhals, A. *Macromolecules* **2011**, *44*, 4342.
- 226 Purohit, P.J.; Wang, D.-Y.; Emmerling, F.; Thünemann, A.; Heinrich, G.; Schönhals, A. *Polymer* **2012**, *53*, 2245.
- 227 Havriliak, S. Negami, S. *J. Polym. Sci. Part C: Polym. Symposia* **1966**, *14*, 99-117.
- 228 Schönhals, A.; Kremer, F. *Analysis of Dielectric Spectra* In: *Broadband Dielectric Spectroscopy*, Kremer, F.; Schönhals, A. Eds., Springer, Berlin, **2002**, p. 59.
- 229 Schlosser, E.; Schönhals, A. *Colloid Polym. Sci.* **1989**, *267*, 963-969.
- 230 Vogel, H. *Physikalische Zeitschrift* **1921**, *22*, 645.
- 231 Fulcher, G. S. *J. Am. Chem. Soc.* **1925**, *8*, 339-355.
- 232 Frunza, L.; Kosslick, H.; Pitsch, I.; Frunza, S.; Schönhals, A. *J. Phys. Chem. B* **2005**, *109*, 9154-9159.
- 233 Kotal, M.; Bhowmick, K. *Prog. Polym. Sci.* **2015**, *51*, 127-187.
- 234 Mao, L.-B.; Yu, S.-H. et. al. *Science* **2016** Aug 18.

---

## List of Symbols

$A_T$	Amplitude of temperature perturbation
$A_a$	Area of the amorphous halo in a WAXS profile
$A_c$	Total area under Bragg peaks in a WAXS profile
$A_{HF}$	Amplitude of the heat flow modulation
$C$	Heat capacity
$C_p$	Heat capacity at constant pressure
$c_p$	Specific heat capacity
$C_{p \text{ non-reversing}}$	Non-reversing heat capacity
$C_{p \text{ reversing}}$	Reversing heat capacity
$C'_p$	Phase corrected reversing heat capacity
$C''_p$	Kinetic heat capacity
$C_1, C_2$	WLF parameters
$d$	Inter-planar spacing involved
$D$	Fragility parameter
$\mathbf{D}$	Dielectric displacement
$E_A$	Activation energy
$\Delta E$	Free energy barrier for a conformational change of a segment
$E$	Electric field
$E(t)$	Periodic electrical field
$E_{Loc}$	Local electrical field
$f$	Relaxation rate
$f_p$	Frequency of the maximal point
$f_\infty$	Prefactor of VFT equation
$g(r)$	Interface distribution function
$H$	Enthalpy
$\Delta H_c$	Crystallization enthalpy
$\Delta H_m$	melting enthalpy
$k_B$	Boltzmann constant
$\mathbf{k}$	Wavevector of a plane wave

---

$\mathbf{k}'$	Modulus of the scattering wavevector
$K$	Scherrer constant
$l_c$	Crystal thickness
$l_a$	Amorphous layer thickness
$m$	Sample mass
$M^*(\omega)$	Complex electric modulus
$M'(\omega)$	Real part of the complex electric modulus
$M''(\omega)$	Imaginary part of the complex electric modulus
$\mathbf{P}$	Polarization
$\mathbf{p}_i$	Microscopic dipole moments
$\mathbf{P}_\infty$	Induced polarizaitons
$\mathbf{P}_\infty$	Electronic and atomic polarization
$\mathbf{q}$	Scattering vector
$R$	Thermal resistance of thermoelectric disk
$t_p$	Modulation period
$T_0$	Initial temperature
$T_c$	Crystallization Temperature
$T_m$	Melting Temperature
$T_g$	Thermal glass transition
$T_K$	Kauzmann temperature
$T_0$	Vogel or ideal glass transition temperature
$T_{\text{Ref}}$	Reference temperature
$S$	Entropy
$S_c(T)$	Total configurational entropy
$V$	Volume
$V_c$	Critical volume
$V_f$	Free volume
$V_m$	Molecular volume
$V^*$	Critical value of volume
$W$	Interaction energy between a dipole and the electric field
$z(T)$	Average number of segments

---

$\alpha$	Polarizability
$\alpha_T$	Shift factor
$\beta$	Underlying heating or cooling rate
$\beta_{1/2}$	Full-width at half-maximum of the scattering peak
$\gamma(r)$	Correlation function
$\delta(t)$	Dirac function
$\varepsilon^*$	Complex dielectric function
$\varepsilon'(\omega)$	Real part of the complex dielectric function
$\varepsilon''(\omega)$	Imaginary part of the complex dielectric function
$\theta$	Angle between the incident ray and the scattering crystal planes
$\lambda$	Wavelength of the radiation
$\Lambda(a)$	Langevin function
$\langle \mu \rangle$	Mean dipole moment
$\mu$	Molecular permanent dipole moment
$\xi$	Radius of a CRR sphere cooperatively rearranging regions
$\rho$	Density of bulk material
$\tau_D$	Characteristic dielectric relaxation time
$\tau$	Mean size of the crystallite
$\varphi$	Phase lag between the modulation in the heat flow and the heating rate
$\Phi$	Heat flow rate
$\Phi(\tau)$	Correlation function
$x_c$	Degree of crystallinity
$\omega$	Angular frequency
$\omega A_T$	Amplitude of the modulation in the heating rate oscillation
$d\Omega$	Differential space angle

---

## List of Abbreviations

CFs	Crystallization Fractions
CNTs	Carbon Nanotubes
CRRs	Cooperatively Rearranging Regions
DSC	Differential Scanning Calorimetry
IGC	Inverse Gas Chromatography
LDH	Layered Double Hydroxides
MAFs	Mobile Amorphous Fractions
MAXS	Medium Angle X-ray Scattering
MMOs	Mixed Metal Oxides
MMT	Montmorillonite
NMR	Nuclear Magnetic Resonance Spectroscopy
PALS	Positron Annihilation Lifetime Spectroscopy
PLA	Poly (L-lactide)
PMMA	Poly(methyl methacrylate)
RAFs	Rigid Amorphous Fractions
RFOT	First Order Transition Theory
SAM	Self-Assembling Monolayers
SAXS	Small Angle X-ray Scattering
SDBS	Sodium dodecyl benzene sulfonate
SEC	Size Exclusion Chromatography
SHS	Specific Heat Spectroscopy
SSDSC	StepScan calorimetry
TEM	Transmission Electron Microscope
TMDSC	Temperature Modulated Differential Scanning Calorimetry
VDOS	Vibrational Density of States
VFT	Vogel-Fulcher-Tammann
WLF	Williams-Landel-Ferry
WAXS	Wide Angle X-ray Scattering
XRD	X-ray diffraction

---

## Publications from this work:

### *Peer-reviewed Journal articles*

1. J. Leng; P. J. Purohit; N.-J. Kang; D.-Y. Wang\*; J. Falkenhagen; F. Emmerling; A. F. Thünemann; A. Schönhals\*, *Structure-property relationships of nanocomposites based on polylactide and MgAl layered double hydroxides*. **Eur. Polym. J.** 2015, 68, pp. 338-354.

2. J. Leng; N.-J. Kang; D.-Y. Wang\*; A. Wurm; C. Schick; A. Schönhals\*, *Crystallization behavior of nanocomposites based on poly(L-lactide) and MgAl layered double hydroxides - Unbiased determination of the rigid amorphous phases due to the crystals and the nanofiller*. **Polymer**, 2017, 108, pp. 257-264.

3. J. Leng; N.-J. Kang; D.-Y. Wang\*; J. Falkenhagen; A. F. Thünemann; A. Schönhals\*, *Structure-property relationships of nanocomposites based on polylactide and layered double hydroxides – Comparison of MgAl and NiAl LDH*. **J. Polym. Sci. Part B**, **Submitted**.

### *Conference (Talks)*

1. J. Leng; D.-Y. Wang; A. Wurm; C. Schick; A. Schönhals, *Crystallization behavior of nanocomposites based on Polylactide – Rigid Amorphous Phase due to the nanofiller*. Spring Meeting, German Physics Society (DPG), Regensburg, Germany, March 2016.

### *Conference (Posters)*

1. J. Leng; P. J. Purohit; A. F. Thünemann; F. Emmerling; D.-Y. Wang; A. Schönhals, *Structure-property relationships of nanocomposites based on polylactide and layered double hydroxides*. Spring Meeting, German Physics Society (DPG), Regensburg, Germany, March 2013.

2. J. Leng; A. Schönhals; A. F. Thünemann; F. Emmerling; D.-Y. Wang, *Structure-property relationship of nanocomposites based on epoxy and layered double hydroxides*. Spring Meeting, German Physics Society (DPG), Dresden, Germany, March 2014.

---

3. J. Leng; P. J. Purohit; A. F. Thünemann; F. Emmerling; D.-Y. Wang; A. Schönhals, *Structure-property relationship of nanocomposites based on polylactide and layered double hydroxides*. 8th International Conference on Broadband Dielectric Spectroscopy and its Applications, Wisla, Poland, September 2014.

4. J. Leng; A. Schönhals; A. F. Thünemann; F. Emmerling; D.-Y. Wang, *Structure-property relationship of nanocomposites based on epoxy and layered double hydroxides*. 8th International Conference on Broadband Dielectric Spectroscopy and its Applications, Wisla, Poland, September 2014.

5. J. Leng; P. J. Purohit; A. F. Thünemann; F. Emmerling; D.-Y. Wang; A. Schönhals, *Structure-property relationships of nanocomposites based on polylactide and layered double hydroxides*. Spring Meeting, German Physics Society (DPG), Berlin, Germany, March 2015.

6. J. Leng; A. F. Thünemann; F. Emmerling; D.-Y. Wang; A. Schönhals, *Structure-property relationship of nanocomposites based on epoxy and layered double hydroxides*. Spring Meeting, German Physics Society (DPG), Berlin, Germany, March 2015.